
Radial electric field studies in the plasma edge of ASDEX Upgrade

Eleonora Viezzer

München 2012



Radial electric field studies in the plasma edge of ASDEX Upgrade

Dissertation zur Erlangung des akademischen Grades eines
Doktors der Naturwissenschaften (Dr. rer. nat.)
an der Fakultät für Physik der Ludwig-Maximilians-Universität München

durchgeführt am
Max-Planck-Institut für Plasmaphysik, Garching bei München

vorgelegt von
Eleonora Viezzer
geboren am 10.10.1986 in Wien

München, den 18.12.2012



Erstgutachter: Prof. Dr. Hartmut Zohm

Zweitgutachter: Prof. Dr. Harald Lesch

Tag der mündlichen Prüfung: 21.2.2013

Zusammenfassung

In magnetisch eingeschlossenen Fusionsplasmen werden Randtransportbarrieren während dem Übergang von einem turbulenten Plasmaregime mit niedrigem Energieeinschluss (L-mode) in ein Regime mit hohem Energieeinschluss (H-mode) aufgebaut. Die Einschlussgüte einer H-mode hängt von der Höhe der Transportbarriere ab. Diese erstreckt sich typischerweise nur über die äußersten 5 % des eingeschlossenen Plasmas. Es ist weitgehend akzeptiert, dass eine verscherte Plasmaströmung senkrecht zum Magnetfeld, hervorgerufen durch ein radiales elektrisches Feld E_r , eine wesentliche Rolle für die Turbulenzunterdrückung am Plasmarand spielt und damit für den Aufbau der Transportbarriere und den Übergang in die H-mode. Daher ist das Wechselspiel zwischen makroskopischen Strömungen und mikroturbulentem Transport ausschlaggebend um den Einschluss des Plasmas zu verstehen.

Der Gegenstand dieser Arbeit ist die Untersuchung und Charakterisierung des radialen elektrischen Felds am Plasmarand des Fusionsexperiments ASDEX Upgrade (AUG). Dazu wurden neue optische Diagnostiken, die auf Ladungsaustauschspektroskopie im sichtbaren Spektralbereich basieren, an der inneren und an der äußeren Mittelebene von AUG installiert. Diese neuen Diagnostiken ermöglichen die Messung zeitlich und räumlich hochaufgelöster Profile der Ionentemperatur, Verunreinigungsdichte und Rotationsgeschwindigkeit einer bestimmten Ionenspezies. Mithilfe der radialen Kraftbilanz kann das E_r Profil direkt aus den Messdaten bestimmt werden, sowohl an der äußeren Niederfeldseite und erstmals auch an der inneren Hochfeldseite. Die neuen Ladungsaustauschmessungen kombiniert mit den bereits existierenden hochauflösenden Randdiagnostiken an AUG ermöglichen eine hochpräzise Lokalisierung (2–3 mm) des E_r Profils.

Das radiale elektrische Feld wurde mittels Ladungsaustauschmessungen an He^{2+} , B^{5+} , C^{6+} und Ne^{10+} bestimmt. Das daraus resultierende E_r Profil ist innerhalb der experimentellen Messungenauigkeiten identisch. In der Randtransportbarriere der H-mode bildet sich ein negatives (nach innen gerichtetes) E_r mit steilen Gradienten aus. Das Minimum des E_r Profils befindet sich nahe der letzten geschlossenen magnetischen Fläche. Die maximale Verschierung von E_r und die steilsten Gradienten in den kinetischen Profilen der Ionen liegen innerhalb des E_r Minimums. Dieses Resultat deutet darauf hin, dass die Region mit negativer E_r Verschierung entscheidend ist für die Unterdrückung der Turbulenz.

Ein Vergleich des E_r Profils mit dem Druckgradiententerm der Hauptionen zeigt, dass dieser Term am Plasmarand in der radialen Kraftbilanz der Hauptionen dominant ist. Dies unterstützt, dass das E_r Minimum durch die Gradienten der Hauptionen hervorgerufen wird. In der Randtransportbarriere ist die Hauptionen-Strömung senkrecht zum Magnetfeld nahezu Null. Dies wurde durch direkte Messung der Hauptionen-Spezies in Heliumplasmen bestätigt. Die Übereinstimmung zwischen dem E_r Minimum und dem maximalen Druckgradiententerm der Hauptionen ist im Einklang mit der Tatsache, dass sich die poloidale Strömung der Hauptionen neoklassisch verhält. Untersuchungen der gemessenen poloidalen Strömung von Verunreinigungen als auch der Hauptionen-Spezies zeigen eine sehr gute Übereinstimmung mit neoklassischen Vorhersagen.

Die vorliegende Arbeit gibt Aufschluss über die Physik, die das radiale elektrische Feld antreibt. Es konnte experimentell nachgewiesen werden, dass am Plasmarand die Gradienten der Hauptionen-Spezies für das starke E_r verantwortlich sind. Aus den Messungen geht hervor, dass die Hauptionen eine entscheidende Rolle im Wechselspiel zwischen $\mathbf{E} \times \mathbf{B}$ -Verschierung, Turbulenz- und Transportreduzierung spielen.

Abstract

In magnetically confined fusion plasmas, edge transport barriers (ETBs) are formed during the transition from a highly turbulent state (low confinement regime, L-mode) to a high energy confinement regime (H-mode) with reduced turbulence and transport. The performance of an H-mode fusion plasma is highly dependent on the strength of the ETB which extends typically over the outermost 5 % of the confined plasma. The formation of the ETB is strongly connected to the existence of a sheared plasma flow perpendicular to the magnetic field caused by a local radial electric field E_r . The gradients in E_r and the accompanying $\mathbf{E} \times \mathbf{B}$ velocity shear play a fundamental role in edge turbulence suppression, transport barrier formation and the transition to H-mode. Thus, the interplay between macroscopic flows and transport at the plasma edge is of crucial importance to understanding plasma confinement and stability.

The work presented in this thesis is based on charge exchange recombination spectroscopy (CXRS) measurements performed at the plasma edge of the ASDEX Upgrade (AUG) tokamak. During this thesis new high-resolution CXRS diagnostics were installed at the outboard and inboard midplane of AUG, which provide measurements of the temperature, density and flows of the observed species. From these measurements the radial electric field can be directly determined via the radial force balance equation. The new CXRS measurements, combined with the other edge diagnostics available at AUG, allow for an unprecedented, high-accuracy localization (2–3 mm) of the E_r profile.

The radial electric field has been derived from charge exchange spectra measured on different impurity species including He^{2+} , B^{5+} , C^{6+} and Ne^{10+} . The resulting E_r profiles are found to be identical within the uncertainties regardless of the impurity species used, thus demonstrating the validity of the diagnostic technique. Inside the ETB the E_r profile forms a deep, negative (i.e. directed towards the plasma center) well, which is localized near the last closed magnetic surface. The maximum E_r shear and the steepest gradients in the ion profiles lie inside the position of the minimum of the E_r well indicating that the negative E_r shear region is the important region for turbulence reduction.

The E_r profile has been compared to the main ion pressure gradient term, which is found to be the dominant contribution at the plasma edge, supporting the idea that the E_r well is created by the main ion species. From these measurements the perpendicular main ion flow velocity is evaluated and is found to be close to 0 in the ETB. This result is evidenced by direct measurements of the main ion species in helium plasmas. The fact that the pressure gradient term of the main ions matches E_r in the ETB is consistent with the main ion poloidal flow being at neoclassical levels. Quantitative comparisons between neoclassical predictions and experimental measurements of both impurity and main ion poloidal rotation show that the sign and the magnitude are in remarkably good agreement. The E_r profile has been measured in different confinement regimes including L- and H-mode. The depth of the E_r well is correlated with the ion pressure at the pedestal top, in keeping with the main ion pressure gradient term being the dominant contribution.

The findings obtained in this work shed more light on the physics governing the radial electric field and the ETB and provide experimental evidence that the E_r well is created by the gradients of the main ion species. The results discussed in this thesis underline that the ion channel plays a key role in the interplay between $\mathbf{E} \times \mathbf{B}$ shearing, turbulence and transport reduction.

Contents

1	Introduction	1
1.1	Fusion - an option for a safe long-term energy supply	1
1.2	H-mode in tokamaks	2
1.3	Earlier results and scope of this thesis	4
2	Theoretical background on the radial electric field at the plasma edge	7
2.1	Particle motion and collisional transport in a tokamak	7
2.1.1	Particle drifts in a magnetic field	7
2.1.2	Collisional transport in a fusion plasma	9
2.2	Theoretical description of plasma flows and the radial electric field	10
2.2.1	Basic equations and ambipolarity condition	10
2.2.2	Neoclassical poloidal rotation	14
2.3	The High-confinement mode (H-mode)	15
2.3.1	Edge Transport Barrier (ETB)	15
2.3.2	Edge localized modes (ELMs)	17
2.3.3	Turbulence suppression in sheared plasma flows	18
3	Edge diagnostics and experimental techniques at ASDEX Upgrade	21
3.1	Measurements of plasma parameters	21
3.1.1	Charge Exchange Recombination Spectroscopy (CXRS)	22
3.1.2	Doppler reflectometry	24
3.1.3	Electron temperature and density measurements	26
3.2	Radial plasma sweep technique	29
3.3	Profile alignment	29
4	The edge CXRS diagnostics at ASDEX Upgrade	33
4.1	CXRS measurements at the low-field side of AUG	33
4.1.1	Toroidal edge CXRS system	33
4.1.2	Poloidal edge CXRS system	36
4.2	CXRS measurements at the high-field side of AUG	38
4.3	Characterization and calibration of CXRS diagnostics	40
4.4	Validation of CXRS measurements	46
4.5	Corrections to CXRS measurements	46

4.5.1	Charge exchange cross-section effect	47
4.5.2	Correction due to Zeeman splitting	53
5	The structure of the edge radial electric field at ASDEX Upgrade	55
5.1	Derivation of the radial electric field at the plasma edge of ASDEX Upgrade .	55
5.2	Validation of the radial electric field measurements	58
5.2.1	Comparison of different impurity species	58
5.2.2	Comparison to Doppler reflectometry measurements	59
5.3	Radial electric field at the inner and outer midplane	62
5.3.1	CXRS measurements at the HFS	62
5.3.2	Electrostatic potential at the HFS and comparison to the LFS	66
6	Connections between the radial electric field and the edge transport barrier	69
6.1	Comparison of E_r to the main ion pressure gradient term	69
6.2	Radial electric field profiles in different confinement regimes	72
6.3	Interdependences between E_r , its shear and pedestal parameters	73
6.4	Temporal evolution of E_r during an ELM cycle	79
6.5	Effect of magnetic perturbations on the edge radial electric field	81
7	Comparison to neoclassical theory	87
7.1	Previous results from other tokamaks	87
7.2	Experimental tests of poloidal flows against neoclassical theory	88
7.2.1	Poloidal main ion rotation velocity	89
7.2.2	Measured impurity flows in comparison with neoclassical simulations	91
7.3	Simulation of low collisionality plasmas	95
8	Summary and Discussion	97
8.1	Summary and conclusions	97
8.2	Directions for future work	100
	Acknowledgements	101
	Bibliography	103
	List of Publications	111

Chapter 1

Introduction

1.1 Fusion - an option for a safe long-term energy supply

A physically and economically viable energy source is essential to meet the energy demand of the next generations. Fusion power has a great potential to meet these demands and is one of the considered energy options. Stars, such as our Sun, generate their power mainly by fusing hydrogen nuclei stepwise to helium. However, on Earth the probability of this reaction is too low due to the weak interaction involved in the process. The stars overcome this problem by their huge mass, i.e. the gravitational force. On Earth, the most prominent fusion reaction is the D-T reaction between two isotopes of hydrogen, deuterium (D) and tritium (T), due to its high cross-section and high energy yield [1]:



The D-T reaction releases the binding energy of 17.6 MeV as kinetic energy shared between a helium ion He (3.5 MeV) and a neutron n (14.1 MeV). D is a non-radioactive isotope which can be extracted from water, while T does not occur naturally on Earth, but can be generated from lithium (Li). In a fusion reactor T will be produced in a self-sustained manner through the reaction between Li and neutrons inside of the so-called Li blanket, just behind the first wall. For a self-sustained cycle of fusion reactions the particles need to be confined such that they experience many collisions before losing their energy. There are different methods for confining the particles: gravitational confinement (like the Sun), inertial confinement (where the heating needs to be faster than the expansion of the fuel and the burn-up condition needs to be fulfilled) and magnetic confinement (where strong magnetic fields are imposed to confine the plasma particles). The technology developed within the magnetic confinement community has good prospects for constructing a viable fusion power plant as a continuous power production is envisaged. The highest energy confinement to date has been achieved in a tokamak configuration [1] (see section 1.2).

The efficiency of a future fusion reactor depends on the fusion power gain Q , the ratio of fusion power to externally applied heating power. If the fusion power is equal to the auxiliary power then $Q = 1$ and ‘break-even’ is obtained. The highest fusion power gain obtained so far has been achieved in a D-T plasma in the JET tokamak, located in Abingdon, England, with $Q \approx 0.62$ [2]. In a future fusion power plant the challenge is to get a self-maintained burning plasma where enough particles are confined for a sufficient time and at a sufficiently high density and temperature such that the heating from the alpha-particles, which are produced during

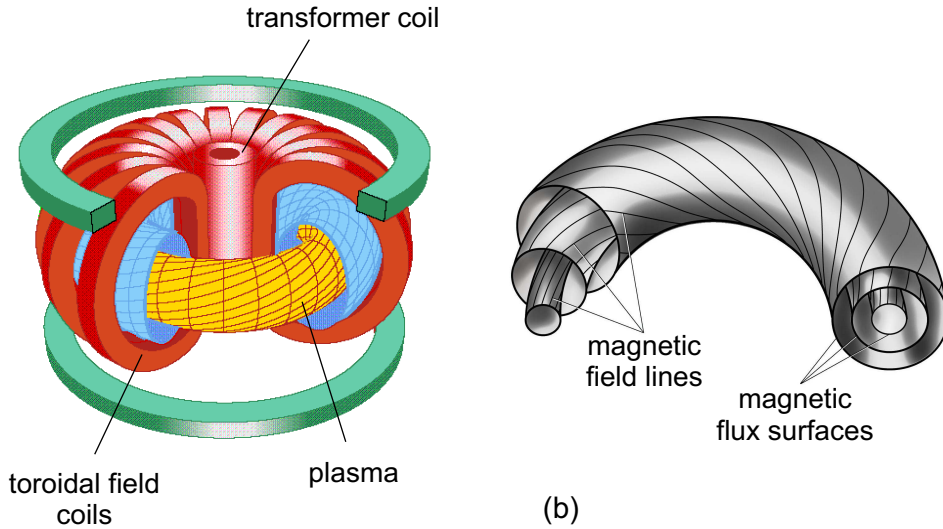


Figure 1.1: (a) Schematic of a tokamak device, (b) magnetic flux surfaces spanned by helical magnetic field lines in a torus.

the fusion reaction, is the main source of heating for the plasma. The threshold for ignition is given by the Lawson criterion, which states that the triple product, i.e. the product of the density, temperature and energy confinement time, needs to be higher than 5×10^{21} keV s m⁻³.

1.2 H-mode in tokamaks

The tokamak is one of the established configurations in the magnetic confinement fusion community. Here, the toroidal magnetic field is produced by external coils, while the poloidal field component is produced by an inductively driven plasma current. This current is induced by a transformer which uses the plasma as a secondary coil. The magnetic flux through the central coil changes inducing a toroidal electric field, which sustains the plasma current. Overlaying the poloidal magnetic field with the externally imposed toroidal magnetic field creates a helical field structure. In figure 1.1(a) an example tokamak configuration is shown, while figure 1.1(b) illustrates the magnetic flux surfaces which are spanned by the helical field lines. The magnetic flux surfaces can be labelled with an index ρ_{pol} which ranges from $\rho_{pol} = 0.0$ in the plasma center to $\rho_{pol} = 1.0$ at the last closed flux surface (LCFS), also called separatrix in a divertor configuration. This normalized poloidal flux label ρ_{pol} is defined as:

$$\rho_{pol} = \sqrt{\frac{\Psi - \Psi_a}{\Psi_s - \Psi_a}} \quad (1.2)$$

where Ψ is the poloidal flux, Ψ_a and Ψ_s are the poloidal flux at the magnetic axis and at the separatrix, respectively. Typical parameters of the ASDEX Upgrade (AUG) tokamak, in which the work for this thesis was performed, are given in table 1.1. AUG is a mid-size tokamak located at the Max-Planck Institute for Plasma Physics in Garching, Germany.

In the 1980s a high energy confinement regime, the H-mode, was observed for the first time at the predecessor experiment ASDEX [3]. The H-mode is characterized by an improved energy confinement, which is about a factor of 2 higher than in the low-confinement regime (also called L-mode), and accompanied by a sharp decrease in the fluctuation level at the plasma

major plasma radius R_0	1.65 m
minor plasma radius a	0.5 m
toroidal magnetic field B_ϕ	1.8–2.8 T
plasma current I_p	0.4–1.2 MA
heating power	up to 30 MW
plasma volume	14 m ³
plasma mass	3 mg
plasma types	D, H, He

Table 1.1: Typical parameters of ASDEX Upgrade.

edge. With the onset of an H-mode the formation of an edge transport barrier is observed and a steep pressure gradient builds up at the edge of the plasma (see figure 1.2(a)). Due to this steepening the pressure profile is shifted upwards along the whole plasma radius leading to the formation of a characteristic pedestal structure. The plasma confinement in the core is directly connected to the edge transport barrier since the height of the pedestal sets the boundary conditions for the core plasma performance. In addition, the radial electric field E_r is observed to develop a deep well in the edge transport barrier, which results in strong gradients in E_r (see figure 1.2(b)). These gradients in E_r are believed to be fundamental for suppressing edge turbulence thus, aiding the formation of the edge transport barrier and leading to the transition from L- to H-mode [4]. However, after 30 years of active research on this field the mechanism responsible for the transition into H-mode is still an open issue. The paradigm in explaining the physics underlying the formation of the edge transport barrier calls for a continuous development and improvement of diagnostic techniques. This is especially true because the edge transport barrier and the E_r well are formed in a thin layer at the plasma boundary, not wider than 2 cm on AUG. Note the scale 5 mm as indicated in figure 1.2(b).

One method for determining E_r is active charge exchange recombination spectroscopy (CXRS) [5] which provides measurements of flows, temperatures and densities. The radial electric field is diagnosed spectroscopically through the radial force balance equation [6]:

$$E_r = \frac{1}{n_\alpha Z_\alpha e} \frac{\partial p_\alpha}{\partial r} - v_{\theta,\alpha} B_\phi + v_{\phi,\alpha} B_\theta. \quad (1.3)$$

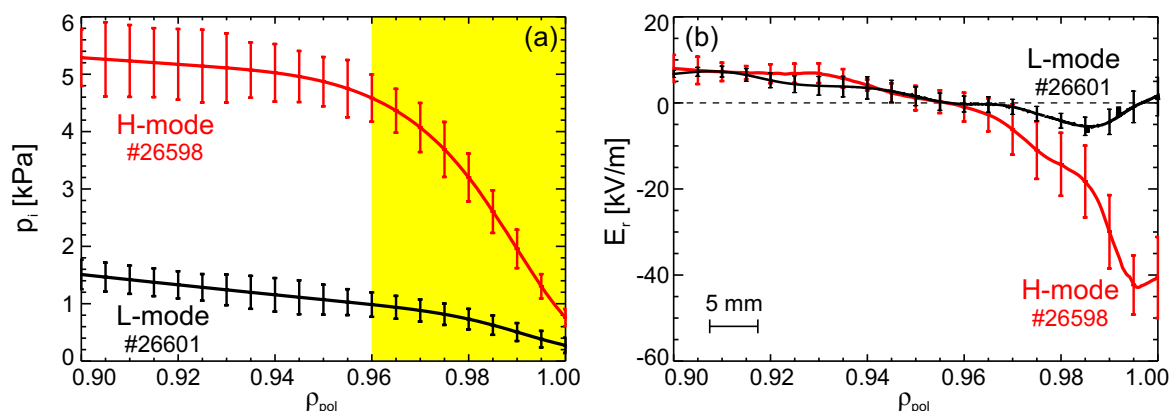


Figure 1.2: Edge profiles in L- and H-mode of the (a) ion pressure and (b) radial electric field. The edge transport barrier region is highlighted in yellow in subfigure (a). Note that the input power in H-mode differed by a factor of ~ 5 compared to the L-mode discharge.

Here, r is the radial coordinate, n_α the density, Z_α the charge state, e the elementary charge, $\frac{\partial p_\alpha}{\partial r}$ the radial pressure gradient and $v_{\theta,\alpha}$ and $v_{\phi,\alpha}$ the poloidal and toroidal rotation velocities of the observed species α . B_ϕ and B_θ denote the toroidal and poloidal magnetic field. CXRS measurements combined with knowledge of the magnetic field components provide all quantities needed to evaluate E_r . Details on the setup of the edge CXRS diagnostics at AUG are given in chapter 4.

1.3 Earlier results and scope of this thesis

In 1988 the importance of the role of the radial electric field E_r in the L-H transition was recognized [7, 8] and since then extensive effort has been directed to the measurement of E_r . The most commonly used tool to determine the radial electric field is active charge exchange recombination spectroscopy (CXRS) [5]. The diagnostic technique exploits spectral lines which are produced by charge transfer from neutral atoms into excited states of impurity ions. Using an external source of neutral particles, such as a neutral beam, provides the advantage of spatial localization as the measured active CX signal is localized in the volume where the lines of sight of the CXRS diagnostics intersect the path of the neutral beam particles.

At DIII-D, a mid-size tokamak located at General Atomics in San Diego, CXRS measurements were performed in the early 1990s [9, 10, 11], which revealed that the radial electric field forms a negative well just inside the last closed flux surface. A correlation between an increased E_r shear and confinement improvement was observed [12]. In standard H-mode operation the depth of the E_r well was found to range between 10 and 30 kV/m, however, depths of up to 100 kV/m were later measured in quiescent H-mode discharges [13]. The width of the E_r well (≈ 1 cm) did not alter significantly despite varying the magnetic field, current, topology and density [14]. At JET, to date the largest tokamak experiment in Europe located at the Culham Centre for Fusion Energy in Abingdon, CXRS measurements of the edge E_r profile [15, 16] showed that the width of the E_r well is of the order ~ 2 cm and reaches depths of up to 50–60 kV/m. High-resolution CXRS measurements at Alcator C-Mod [17], a compact high-field tokamak (up to 8 T) at the Massachusetts Institute of Technology in Cambridge, USA, showed that the E_r well reaches depths of up to 300 kV/m, while the width was found to be 5 mm. Combining the E_r data with other machines indicated a scaling of the E_r well with machine size [17]. Recent upgrades to the CXRS diagnostics at JT-60U [18], a tokamak operated at the Naka Fusion Institute in Japan which has a size similar to JET, enabled radially and temporally resolved E_r measurements which indicate that the E_r shear is not directly connected to higher plasma confinement, but rather a complex relation exists between these two parameters. In H-mode discharges the depth of the E_r well reached values of up to 80 kV/m.

Another diagnostic technique capable of measuring the radial electric field is Doppler reflectometry [19], which measures the perpendicular velocity of density fluctuations and can be related to the $\mathbf{E} \times \mathbf{B}$ velocity and thus, to E_r . In addition, the heavy ion beam probe [20, 21], which provides radial measurements of the plasma potential and hence E_r , or probes, which measure the potential in the scrape-off layer and in the very edge of the plasma, may be used to diagnose E_r .

At AUG previous radial electric field measurements were based on CXRS in the plasma core [22], Doppler reflectometry [23, 24] in the plasma core and at the edge and passive He^+ emission spectroscopy, which provides measurements at the plasma edge and in the

scrape-off layer [25]. The previous CXRS measurements of E_r provided temporally and radially resolved profiles in the core of the plasma, however, the interpretation of the data was challenging due to atomic physics effects in the measured spectra [22]. These effects are discussed in chapter 4. Using passive emission spectroscopy of He^+ allows E_r profiles to be measured in all types of discharges without disturbing the plasma by a beam or a gas puff, however, a deconvolution of the line-integrated measurements is required to obtain an E_r profile. This was performed by forward modelling in the framework of integrated data analysis using Bayesian probability theory [26]. However, this approach lacks radial resolution as the measurements are integrated along the lines of sight and the localization of the E_r well depends on the magnetic equilibrium. Doppler reflectometry on the other hand is a powerful diagnostic to measure fast transient events as the time resolution is of the order of μs . However, the measurements require turbulent fluctuations, thus hampering measurements in the H-mode edge pedestal region where turbulence is strongly reduced. The radial positioning of the measurements relies on the local density profile and thus, the localization of E_r depends on additional diagnostics.

The work presented in this thesis is based on CXRS measurements performed at the plasma edge of AUG using the new edge CXRS diagnostics, which were installed to enable an independent and local measurement of the radial electric field. The main advantage of deriving E_r from active CXRS is the high accuracy in the spatial localization of the measurements. The evaluation of E_r is independent of measurements of other diagnostics and relies solely on the CXRS measurements and magnetic field components, which are very well known at the plasma edge. Furthermore, a high-accuracy alignment with respect to the edge kinetic profiles is possible because the ion temperature is part of the CXRS measurements and thus, is rigidly connected to the E_r profile. The edge diagnostic suite available at AUG provides high-accuracy measurements with high temporal and spatial resolution which are required for the measurement of complete edge kinetic profiles and their gradients. This unique diagnostic set combined with an established alignment procedure enables a full and very detailed comparison between the E_r profile and the edge kinetic profiles. Comparing multiple impurity species allows for a validation of the diagnostic technique and to test whether the E_r profile is consistently determined. The installation of novel CXRS measurements at the inboard midplane allows the unprecedented study of E_r at two different poloidal locations and thus, provides an experimental consistency check of the electrostatic potential Φ being a flux function.

The aim of this thesis is to gain a better understanding of the connections between the radial electric field E_r , E_r shear, the edge transport barrier and plasma particle and energy confinement. The structure, the evolution and the behaviour of E_r is studied in a variety of plasma regimes. In particular, the physics questions which are addressed in this work are:

- What is the structure of E_r in the H-mode edge transport barrier? How is E_r characterized with respect to the edge kinetic profiles?
- What is the behaviour of E_r in different confinement regimes?
- Are the impurity density, temperature and flows forming an equilibrium within a flux surface? Is the electrostatic potential constant along the flux surface?
- Neoclassical transport theory, which is the extension of classical diffusion to include the toroidal tokamak geometry, allows the prediction of transport fluxes and the poloidal

flows. Is neoclassical theory sufficient to describe the observed poloidal rotation velocities at the plasma edge?

This thesis is structured as follows:

Chapter 2 describes the underlying physical background important to this thesis. In chapter 3 an overview on the available edge diagnostics at AUG, which are relevant for the present work, is presented. Chapter 4 describes the details of the diagnostic setup of the edge CXRS systems and discusses the data analysis techniques used in this thesis. In chapter 5 a general description on the evaluation of E_r is provided. The structure of E_r is presented along with a validation of the E_r measurements. The poloidal flow structure of the impurities and the radial electric field measured at the inner and outer midplane are described. Chapter 6 discusses the interdependence of E_r and the edge kinetic profiles and its gradients. The E_r profiles measured in different confinement regimes are presented and the connections between E_r and the edge transport barrier are described. In chapter 7, a comparison between the measured poloidal rotation velocities to neoclassical theory is presented and the findings are discussed. Chapter 8 summarizes the results and main points of this thesis and gives a brief outlook for future work.

Chapter 2

Theoretical background on the radial electric field at the plasma edge

The edge radial electric field and its shear play a key role in the sudden plasma transition to a higher energy confinement state, also called H-mode. In this chapter the relation between the plasma rotation, the radial electric field E_r and heat and particle transport is presented. The basic principles for deriving an expression for the radial electric field are discussed. The general characteristics of the H-mode are described and an overview of the most widely accepted model to explain the transition into H-mode is given.

2.1 Particle motion and collisional transport in a tokamak

2.1.1 Particle drifts in a magnetic field

The high temperatures required for fusion reactions imply that the interaction between the hot plasma particles and the plasma facing components needs to be minimized in order to avoid damage of the first wall. Magnetic fields are used to confine the charged particles, thus keeping them away from the wall. In a magnetic field, a charged particle α with electric charge q_α and mass m_α feels the Lorentz force, which is perpendicular to the particle velocity \mathbf{v}_α and to the magnetic field \mathbf{B} :

$$\mathbf{F} = m_\alpha \frac{d\mathbf{v}_\alpha}{dt} = q_\alpha \mathbf{v}_\alpha \times \mathbf{B}. \quad (2.1)$$

This force causes the particle to gyrate around the magnetic field lines at the gyro-frequency $\omega_{c,\alpha}$ (the cyclotron frequency) and with the gyro-radius $r_{L,\alpha}$ (also called Larmor radius):

$$\omega_{c,\alpha} = \frac{|q_\alpha| B}{m_\alpha} \quad r_{L,\alpha} = \frac{v_{\perp,\alpha}}{\omega_{c,\alpha}} = \frac{m_\alpha v_{\perp,\alpha}}{|q_\alpha| B} \quad (2.2)$$

where $v_{\perp,\alpha}$ is the velocity component perpendicular to the magnetic field. If an additional force \mathbf{F} with a non-zero component perpendicular to the magnetic field acts on the charged particles, guiding center drifts occur [1]. In this ansatz the gyromotion is separated from the motion of the center of the gyration, which is called the guiding center. For magnetic fields that feature large spatial gradient scale lengths $\nabla B/B$ and slow temporal changes of magnitude $\frac{\partial B}{\partial t}/B$ with respect to the Larmor radius and cyclotron frequency, this approximation is valid.

The guiding center drifts are different to the gyration, because they move the particles across the magnetic field. In general, this particle drift velocity is given by the expression:

$$\mathbf{v}_d = \frac{\mathbf{F} \times \mathbf{B}}{q_\alpha B^2}. \quad (2.3)$$

In a tokamak important guiding center drifts are, amongst others, the $\mathbf{E} \times \mathbf{B}$ -drift (2.4), the ∇B -drift (2.5) and the curvature drift (2.6). If an electric field \mathbf{E} perpendicular to the magnetic field \mathbf{B} exists the charged particles will feel an additional force, i.e. $\mathbf{F} = q\mathbf{E}$, which results in the $\mathbf{E} \times \mathbf{B}$ velocity drift:

$$\mathbf{v}_{\mathbf{E} \times \mathbf{B}} = \frac{\mathbf{E} \times \mathbf{B}}{B^2}. \quad (2.4)$$

Note that the $\mathbf{E} \times \mathbf{B}$ drift is independent of the charge of the particle and is, therefore, in the same direction for both electrons and ions. The shear of an $\mathbf{E} \times \mathbf{B}$ velocity drift is believed to be fundamental for turbulence suppression in the plasma edge, thus leading to an improved plasma confinement regime, the H-mode (see section 2.3). Hence, this drift is a crucial ingredient in this thesis and its interconnection to turbulence suppression and confinement improvement will be discussed in detail in section 2.3.

In a tokamak the absolute value of the magnetic field has a gradient in the direction of the major radius R and an additional force perpendicular to both the magnetic field and its gradient acts on the gyrating particles and causes the ∇B -drift:

$$\mathbf{v}_{\nabla B, \alpha} = -\frac{m_\alpha v_{\perp, \alpha}^2}{2q_\alpha B^3} \nabla B \times \mathbf{B}. \quad (2.5)$$

The particles moving along the magnetic field lines are subject to a centrifugal force, since the field lines are curved. The centrifugal force results in the curvature drift:

$$\mathbf{v}_{curv, \alpha} = -\frac{m_\alpha v_{\parallel, \alpha}^2}{q_\alpha B^3} \nabla B \times \mathbf{B}. \quad (2.6)$$

A charged particle travelling along the magnetic field lines will pass through regions of different magnetic field strengths. If the particle moves into a region with stronger magnetic field its perpendicular velocity component $v_{\perp, \alpha}$ increases while the parallel velocity component $v_{\parallel, \alpha}$ decreases due to the conservation of the particle energy $E = mv^2$ and its magnetic moment $\mu = mv_{\perp}^2/2B$. Particles with low parallel velocity compared to their perpendicular velocity will get trapped in a magnetic mirror as the magnetic field is not constant along a field line.

Due to the curvature and ∇B drifts the trapped particles are displaced from the magnetic surface and the projection of their orbits onto a poloidal cross-section of the plasma has a banana-like shape since they are reflected as soon as the parallel velocity is fully converted into the perpendicular velocity.

Another drift motion important to this thesis is the diamagnetic drift (see section 2.2.1). This drift is not a guiding center drift, but an apparent drift motion (i.e. a fluid drift) arising from the presence of a gradient perpendicular to the magnetic field. Figure 2.1 illustrates the situation for ions in the presence of a density gradient. Due to the density gradient, in a given volume element there are more particles gyrating in the upward direction than in the downward direction, thus causing a net current. This current is also called the diamagnetic current \mathbf{j}_{dia} . The particles seem to drift, but they are not displaced. A similar effect is caused by a temperature gradient and the general formula for the diamagnetic drift is $\mathbf{v}_{dia, \alpha} = -\frac{\nabla p_\alpha \times \mathbf{B}}{q_\alpha n_\alpha B^2}$, where n_α is the

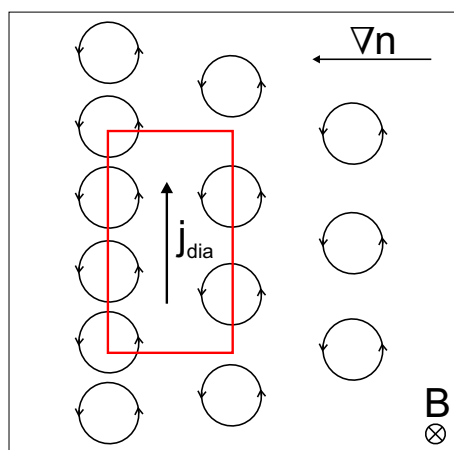


Figure 2.1: Schematic principle of the diamagnetic drift for ions: in the presence of a density gradient, in a given volume element more particles are gyrating in the upward direction than in the downward direction, leading to an apparent drift motion and causing a net current \mathbf{j}_{dia} .

density of the considered species α . Note that the diamagnetic drift depends on the charge of the particles and hence, the diamagnetic drift direction is opposite for electrons and ions.

Other drifts such as the polarization drift or gravitational drift exist, however, only the drifts presented above are relevant to this thesis.

2.1.2 Collisional transport in a fusion plasma

As discussed above, charged particles are bound to the magnetic field, but since they gyrate around the field lines they can collide with particles moving on other magnetic flux surfaces. This leads to radial particle transport (i.e. perpendicular to the magnetic flux surfaces), called classical transport. Here the typical scale length is given by the Larmor radius r_L (equation (2.2)) and the typical time scale is the collision time, i.e. the time needed for cumulative collisions to scatter the pitch angle of the particle by 90° in the velocity space. The inverse of the collision time is also termed as collision frequency for collisions of 90° .

In a tokamak, effects due to the toroidal geometry arise taken into account in neoclassical transport theory [27] which represents classical diffusion corrected for the effects of the toroidal curvature. The main differences to classical transport are: (i) particles can get trapped in a magnetic mirror as the magnetic field is not constant along the field line, (ii) the banana orbits of the trapped particles due to the curvature and ∇B drifts (as described above) [1]. Here, the typical scale length is the banana width given by $r_b = r_L q / \sqrt{\epsilon}$, where q is the safety factor and ϵ the inverse aspect ratio, i.e. $q = m/n$ and $\epsilon = r/R$ (with m and n the number of toroidal and poloidal turns of a magnetic field line to close on itself, r the minor radius and R the major radius of the tokamak). The typical time scale is given by the effective collision frequency $\nu_{eff} = \nu / 2\epsilon$ where ν is the collision frequency for 90° collisions. The fact that a trapped particle becomes a passing particle for scattering angles of $\sqrt{2\epsilon}$ is taken into account in the theory [28].

The curvature of the plasma enhances the diffusion process and, depending on the collisionality ν_* , the transport induced by Coulomb collisions is split into three regimes. The collisionality is defined as the effective collision frequency normalized to the trapped particle bounce

frequency ω_b [29]:

$$\nu_* = \nu_{\text{eff}}/\omega_b = \frac{\nu q R}{\epsilon^{3/2} v_{th}} \quad (2.7)$$

where v_{th} is the thermal particle velocity. In the high collisionality regime ($\nu_* > \epsilon^{-3/2}$), the Pfirsch-Schlüter regime, trapped thermal particles typically do not complete a single banana orbit without experiencing a collision. In the banana regime (the low collisionality regime, $\nu_* < 1$) particles complete several banana orbits before colliding. In the intermediate regime, the plateau regime ($1 < \nu_* < \epsilon^{-3/2}$), trapped particles collide before completing a banana orbit, while slowly gyrating particles with low parallel velocity are almost collisionless. These particles dominate the transport in this regime [1]. At the plasma edge the impurities, which are intrinsically present in the plasma or actively injected (e.g. nitrogen seeding), are usually in the high collisionality regime, while the main ions can be either in the low, medium or high collisionality regime.

The radial particle and thermal transport present in tokamak plasmas is not well described by means of neoclassical theory [27, 30, 29], which also predicts the heat transport, since at all radii the measured heat and particle diffusivities are typically larger than the theoretical predictions. Experiments demonstrate that in tokamak plasmas the heat flux of electrons is two orders of magnitude higher than the neoclassical value and under certain conditions also the ion heat transport is a few times larger than the neoclassical prediction [31]. Neoclassical theory does not account for micro-instabilities in the plasma. These are believed to play a crucial role in the enhancement of transport, called turbulent transport, due to variations in the electric field (electrostatic turbulence) arising from small scale density and/or temperature fluctuations or due to variations in the magnetic field (magnetic turbulence) [32]. However, in the edge transport barrier of an H-mode plasma (see section 2.3) turbulent transport is strongly reduced. In this region the ion heat transport level and the particle transport of impurities [33] is near neoclassical values, while the electron heat transport is also reduced but still larger than the neoclassical prediction.

Neoclassical theory predicts the flux-surface averaged transport fluxes and the poloidal flows of main ions and impurities. The basic concepts of the theoretical description of plasma flows and the radial electric field E_r are presented in the next section.

2.2 Theoretical description of plasma flows and the radial electric field

2.2.1 Basic equations and ambipolarity condition

The motion of a particle species α which experiences electric and magnetic forces can be derived from the Fokker-Planck equation [1, 34]:

$$\frac{\partial f_\alpha}{\partial t} + \mathbf{v}_\alpha \cdot \nabla_r f_\alpha + \frac{q_\alpha}{m_\alpha} (\mathbf{E} + \mathbf{v}_\alpha \times \mathbf{B}) \cdot \nabla_v f_\alpha = C_\alpha(f) \quad (2.8)$$

where m_α , q_α are the mass and charge of the particle and $f_\alpha = f_\alpha(\mathbf{r}, \mathbf{v}, t)$ is its distribution function in a six-dimensional phase space. The Fokker-Planck collision operator $C_\alpha(f) = \sum_\beta C_{\alpha\beta}$ describes the change per unit of time of the distribution function f_α given by Coulomb collisions with the particle species β . An equation for the mean velocity of all particles of

species α may be obtained by taking the first order velocity moment of (2.8) and allowing for an external force. This results in the momentum or force balance equation [29]:

$$m_\alpha n_\alpha \left(\frac{\partial \mathbf{v}_\alpha}{\partial t} + (\mathbf{v}_\alpha \cdot \nabla) \mathbf{v}_\alpha \right) = n_\alpha q_\alpha (\mathbf{E} + \mathbf{v}_\alpha \times \mathbf{B}) - \nabla p_\alpha - \nabla \cdot \mathbf{\Pi}_\alpha + \mathbf{R}_\alpha + \mathbf{F}_\alpha. \quad (2.9)$$

Here, n_α denotes the density, \mathbf{v}_α the fluid velocity, p_α the scalar pressure, $\mathbf{\Pi}_\alpha$ the viscous stress tensor, \mathbf{R}_α the collisional friction and \mathbf{F}_α represents the external momentum change per volume due to e.g. neutral beam injection. The fluid velocity is formally derived from (2.9) by taking the cross product with the magnetic field $\mathbf{B} = bB$ from the right:

$$\mathbf{v}_\alpha = v_{\parallel,\alpha} \mathbf{b} - \left[\frac{1}{n_\alpha q_\alpha} \left(m_\alpha n_\alpha \dot{\mathbf{v}}_\alpha + \nabla p_\alpha + \nabla \cdot \mathbf{\Pi}_\alpha - \mathbf{R}_\alpha - \mathbf{F}_\alpha \right) - \mathbf{E} \right] \times \frac{\mathbf{B}}{B^2} \quad (2.10)$$

where $\dot{\mathbf{v}}_\alpha = \frac{\partial \mathbf{v}_\alpha}{\partial t} + \mathbf{v}_\alpha \cdot \nabla \mathbf{v}_\alpha$. The second term on the right-hand side of equation (2.10) (i.e. the cross-product with \mathbf{B}/B^2) describes the perpendicular velocity. To lowest order, i.e. the viscous forces are much smaller than the pressure gradient and inertia, collisional friction and external forces are neglected, equation (2.10) simplifies to:

$$\mathbf{v}_\alpha = v_{\parallel,\alpha} \mathbf{b} + \left[-\frac{\nabla p_\alpha}{n_\alpha q_\alpha} + \mathbf{E} \right] \times \frac{\mathbf{B}}{B^2} \quad (2.11)$$

$$\Rightarrow \mathbf{v}_{\perp,\alpha} = -\frac{\nabla p_\alpha \times \mathbf{B}}{n_\alpha q_\alpha B^2} + \frac{\mathbf{E} \times \mathbf{B}}{B^2} = \mathbf{v}_{dia,\alpha} + \mathbf{v}_{\mathbf{E} \times \mathbf{B}}. \quad (2.12)$$

Hence, the perpendicular velocity of a species is given by the sum of the diamagnetic drift and the $\mathbf{E} \times \mathbf{B}$ velocity. Note that $\mathbf{v}_\perp = \mathbf{e}_\perp v_\perp$ where $\mathbf{e}_\perp = \mathbf{b} \times \mathbf{e}_\Psi$ is the unit vector in the perpendicular direction and \mathbf{e}_Ψ the unit vector along $\nabla \Psi$, Ψ being the poloidal magnetic flux. In axisymmetric configurations the equality $\frac{\nabla \Psi \times \mathbf{B}}{B^2} = \frac{RB_\theta}{B} \mathbf{e}_\perp$ holds, where R is the local major radius and B_θ the poloidal magnetic field. The pressure p_α and the electrostatic potential Φ are assumed to be flux functions. Using $\nabla p_\alpha = \frac{\partial p_\alpha}{\partial \Psi} \nabla \Psi$ and $\mathbf{E} = -\nabla \Phi = -\frac{\partial \Phi}{\partial \Psi} \nabla \Psi$ the perpendicular species velocity may be rewritten to:

$$\mathbf{v}_{\perp,\alpha} = -\left(\frac{1}{n_\alpha q_\alpha} \frac{\partial p_\alpha}{\partial \Psi} + \frac{\partial \Phi}{\partial \Psi} \right) \frac{\nabla \Psi \times \mathbf{B}}{B^2} \quad (2.13)$$

$$\Rightarrow v_{\perp,\alpha} = -\left(\frac{1}{n_\alpha q_\alpha} \frac{\partial p_\alpha}{\partial \Psi} + \frac{\partial \Phi}{\partial \Psi} \right) \frac{RB_\theta}{B}. \quad (2.14)$$

Introducing the radial coordinate r and using the equality $\frac{\partial r}{\partial \Psi} = \frac{1}{RB_\theta}$ yields:

$$v_{\perp,\alpha} = -\left(\frac{1}{n_\alpha q_\alpha} \frac{\partial p_\alpha}{\partial r} \frac{\partial \Psi}{\partial r} + \frac{\partial \Phi}{\partial r} \frac{\partial r}{\partial \Psi} \right) \frac{RB_\theta}{B} \quad (2.15)$$

$$\Rightarrow v_{\perp,\alpha} = -\left(\frac{1}{n_\alpha q_\alpha} \frac{\partial p_\alpha}{\partial r} + \frac{\partial \Phi}{\partial r} \right) \frac{1}{B}. \quad (2.16)$$

Solving equation (2.16) for the radial electric field $E_r = -\frac{\partial \Phi}{\partial r}$ results in the **radial force balance** equation:

$$E_r = \frac{1}{n_\alpha q_\alpha} \frac{\partial p_\alpha}{\partial r} + v_{\perp,\alpha} B \quad (2.17)$$

$$= \frac{1}{n_\alpha q_\alpha} \frac{\partial p_\alpha}{\partial r} - v_{\theta,\alpha} B_\phi + v_{\phi,\alpha} B_\theta. \quad (2.18)$$

Using the relation $\mathbf{e}_\perp = -\frac{B_\phi}{B}\mathbf{e}_\theta + \frac{B_\theta}{B}\mathbf{e}_\phi$, where \mathbf{e}_θ and \mathbf{e}_ϕ are the unit vectors in the poloidal and toroidal directions, equation (2.17) transforms to equation (2.18). Here, $v_{\theta,\alpha}$ and $v_{\phi,\alpha}$ correspond to the poloidal and toroidal rotation velocities of the species, while B_ϕ and B_θ denote the toroidal and poloidal magnetic field. The radial force balance relates the lowest-order flow ($v_{\theta,\alpha}$ and $v_{\phi,\alpha}$) on a magnetic surface to the local $\mathbf{E}\times\mathbf{B}$ velocity (caused by the radial electric field) and to the diamagnetic flow (pressure gradient) [27]. Using the radial force balance equation, the radial electric field E_r can be evaluated from the pressure gradient term of the ion species α , which depends on the density n_α , the charge $q_\alpha = Z_\alpha e$ (Z_α being the charge state and e the elementary charge) and the radial pressure gradient $\frac{\partial p_\alpha}{\partial r}$, the poloidal rotation term and the toroidal rotation term.

The radial force balance may be rewritten to give an expression for the parallel ion velocity $v_{\parallel,i}$. The general velocity expression $\mathbf{v} = v_{\parallel}\mathbf{b} + \mathbf{v}_\perp$ (equation (2.11)) may be combined with $\mathbf{v} = v_\phi\mathbf{e}_\phi + v_\theta\mathbf{e}_\theta$ to give:

$$v_{\parallel,i} = v_{\theta,i}\frac{B}{B_\theta} + v_{\perp,i}\frac{B_\phi}{B_\theta} = v_{\theta,i}\frac{B}{B_\theta} + \frac{1}{B}\left(E_r - \frac{1}{n_i q_i}\frac{\partial p_i}{\partial r}\right)\frac{B_\phi}{B_\theta} \quad (2.19)$$

Multiplying equation (2.19) with the magnetic field B and taking the flux surface average leads to:

$$\langle v_{\parallel,i}B \rangle = v_{\theta,i}\frac{\langle B^2 \rangle}{B_\theta} + RB_\phi\left[-\frac{\partial\Phi}{\partial\Psi} - \frac{1}{n_i q_i}\frac{\partial p_i}{\partial\Psi}\right] \quad (2.20)$$

where $\Phi = \Phi(\Psi)$ is the electrostatic potential and $\frac{v_{\theta,i}}{B_\theta}$ is constant on a flux surface. Using the neoclassical expression for the poloidal rotation velocity (see section 2.2.2) and the flux function $f(\Psi) = RB_\phi$ results in [27]:

$$\langle v_{\parallel,i}B \rangle = \frac{1}{2}v_{th,i}\rho_i K_1 \frac{d(\ln T_i)}{d\Psi} f(\Psi)B + f(\Psi)\left[-\frac{\partial\Phi}{\partial\Psi} - \frac{1}{n_i q_i}\frac{\partial p_i}{\partial\Psi}\right] \quad (2.21)$$

where $v_{th,i}$ is the thermal ion velocity, ρ_i the ion Larmor radius and K_1 a collisionality-dependent viscosity coefficient as defined in [35]. Hence, with knowledge of the radial electric field and the gradients of the ion temperature and ion pressure, the parallel ion velocity may be obtained.

Theory allows the prediction of the radial electric field E_r via the ambipolarity condition of the radial particle fluxes, which connects the radial electric field with the flows in a plasma. This condition can be derived as follows: summing the momentum balance equation (2.9) over all species results in:

$$mn\dot{\mathbf{v}} = \mathbf{j} \times \mathbf{B} - \nabla p - \nabla \cdot \Pi + \mathbf{F} \quad (2.22)$$

where \mathbf{j} is the total current of all species. Here, the electric field \mathbf{E} drops out as it is the same for all species and the collisional friction forces between charged particles vanish as $\sum_\alpha \mathbf{R}_\alpha = 0$. Taking the cross product with the magnetic field from the right results in:

$$\mathbf{j} = j_{\parallel}\mathbf{b} - \left[mn\dot{\mathbf{v}} + \nabla p + \nabla \cdot \Pi - \mathbf{F} \right] \times \frac{\mathbf{B}}{B^2} \quad (2.23)$$

$$\Rightarrow \mathbf{j}_\perp = mn\frac{\dot{\mathbf{v}} \times \mathbf{B}}{B^2} + \frac{\nabla p \times \mathbf{B}}{B^2} + \frac{\nabla \cdot \Pi \times \mathbf{B}}{B^2} - \frac{\mathbf{F} \times \mathbf{B}}{B^2} \quad (2.24)$$

The fundamental requirement for the ambipolarity condition is given by a divergence-free current, i.e. $\nabla \cdot \mathbf{j} = 0$ [29, 36], leading to:

$$\nabla \cdot (j_{\parallel}\mathbf{b} + \mathbf{j}_\perp) = 0. \quad (2.25)$$

Here, \mathbf{j}_\perp is the current perpendicular to the magnetic field and is the parameter in which the radial electric field enters through the flows, \mathbf{v} . Taking the flux surface average and using $\langle \nabla \cdot \mathbf{j}_\parallel \mathbf{b} \rangle = 0$ results in:

$$\langle \nabla \cdot \mathbf{j} \rangle = \langle \nabla \cdot \mathbf{j}_\perp \rangle = \frac{\partial}{\partial r} \langle j_r |\nabla \Psi| \rangle = 0. \quad (2.26)$$

Using the identity $\nabla \Psi = \partial \Psi / \partial r = RB_\theta$, equation (2.26) may be rewritten to $\langle RB_\theta j_r \rangle = 0$. Thus, in a pure plasma with only electrons and ions the ambipolarity condition which determines the radial electric field E_r is given by:

$$\langle RB_\theta j_r \rangle = \Gamma_i(E_r) - \Gamma_e(E_r) = 0. \quad (2.27)$$

and the main features can be described in terms of the two-fluid equations. In equation (2.27) $\Gamma_{i,e} = \langle \Gamma_{i,e} \cdot \nabla \Psi \rangle$ are the flux surface averaged transport fluxes of the ions and electrons, respectively.

In the case of dominant external forces, such as neutral friction [37], the radial electric field can be determined as follows: The diamagnetic flows in the ion and electron fluid arise due to the pressure gradient and are pointing into opposite directions. Thus, a diamagnetic current $\mathbf{j}^{dia} = \rho(v_{dia,i} - v_{dia,e})$ is built up and is subject to a friction force $F_{ei,fr} = \eta \mathbf{j}^{dia}$, where ρ is the charge density and η the plasma resistivity. This causes ambipolar radial transport of ions and electrons which is described by the radial drift velocity $u_{r,i} = u_{r,e} = F_{ei,fr} / enB$, where n is the density and B the magnetic field. In addition, the force arising due to neutral friction acts differently on electrons and ions and hence, leads to bipolar losses. The perpendicular neutral friction force density acting on the species α is given by $F_{\alpha,n} = -n\hat{\nu}_{\alpha,n}m_\alpha^{1/2}v_{\perp,\alpha}$, where $\hat{\nu}_{\alpha,n}$ is the collision frequency between particles and neutrals normalized to the mass of the particle m_α , i.e. $\hat{\nu}_{\alpha,n} = \nu_{\alpha,n}/m_\alpha^{1/2}$. The perpendicular flow velocity of the species, $v_{\perp,\alpha}$, is given by the diamagnetic and the $\mathbf{E} \times \mathbf{B}$ drifts:

$$v_{\perp,\alpha} = v_{dia,\alpha} - \frac{E_r}{B} \quad (2.28)$$

Due to the neutral friction force, radial outward drifts of both electrons and ions arise. The drift velocity is given by $v_{r,\alpha} = F_{\alpha,n} / q_\alpha nB$. The ambipolarity condition, which demands equal radial drift velocities ($v_{r,i} = v_{r,e}$), can only be fulfilled if $F_{i,n} = -F_{e,n}$, which is obtained when the $\mathbf{E} \times \mathbf{B}$ drift velocity (and thus, the perpendicular flow velocity (2.28) of each species) adjusts such that the perpendicular neutral friction force densities are the same for both electrons and ions. Hence, the radial electric field is determined by the ambipolarity condition leading to [37]:

$$\frac{E_r}{B} = \left(\frac{1 - \left(\frac{m_e}{m_i}\right)^{1/2} \frac{\hat{\nu}_{n,e}}{\hat{\nu}_{n,i}} \frac{\partial p_e}{\partial r} / \frac{\partial p_i}{\partial r}}{1 + \left(\frac{m_e}{m_i}\right)^{1/2} \frac{\hat{\nu}_{n,e}}{\hat{\nu}_{n,i}}} \right) v_{dia,i} \quad (2.29)$$

In case of $T_e \approx T_i$ and $\hat{\nu}_{n,e} \approx \hat{\nu}_{n,i}$ equation (2.29) simplifies to:

$$E_r = \left(\frac{1 - \left(\frac{m_e}{m_i}\right)^{1/2}}{1 + \left(\frac{m_e}{m_i}\right)^{1/2}} \right) v_{dia,i} B \approx v_{dia,i} B \quad (2.30)$$

Since the electron to ion mass ratio is small, the radial electric field is determined by the diamagnetic drift velocity of the ions. This in turn means that the $\mathbf{E} \times \mathbf{B}$ drift and the ion diamagnetic drift are in balance and the ion fluid velocity is almost zero. The radial electric field is defined by the ambipolarity condition leading to:

$$E_r \approx \frac{\nabla p_i}{en_i} \quad (2.31)$$

Note that neutral friction might only be important at the very edge of the plasma, where the density of the neutrals is high while further inwards it drops exponentially.

If impurities are present in the plasma, the friction terms between all species become relevant and need to be considered, however, the basic physics principle remains similar as described above. In neoclassical codes such as NEOART [38] the friction terms between main ions, impurity and electrons are treated consistently.

In the more general case, in which the neutral friction force is not the dominant mechanism, the radial electric field is determined by other non-ambipolar particle transport mechanisms, such as neoclassical toroidal viscosity [39, 40], turbulent Reynolds stress [41, 42], ion orbit losses [43], fast-ion orbit width effects [44] and auxiliary toroidal torque via e.g. neutral beam injection. Only in specific cases all these contributions can produce a simple relationship as in equation (2.31), which requires in particular both the poloidal and the toroidal rotation velocity to be damped to small values, as it is indeed observed in the pedestal region (see chapters 6 and 7).

2.2.2 Neoclassical poloidal rotation

Using the Hirshman and Sigmar moment approach [30], the equilibrium flux-surface averaged parallel component of the momentum force balance (2.9) for one main ion and one impurity species is [35]:

$$\langle \mathbf{B} \cdot \nabla \cdot \mathbf{\Pi}_\alpha \rangle = \langle \mathbf{B} \cdot \mathbf{F}_\alpha \rangle \quad (2.32)$$

where \mathbf{F}_α is the friction force. Here, external forces, the parallel electric field E_{\parallel} and the electron contributions to the viscous and friction forces are neglected. The equilibrium flux-surface averaged parallel momentum equation (2.32) describes a balance between viscous and friction forces. In the Pfirsch-Schlüter regime, the neoclassical main ion and impurity poloidal rotation velocities, $v_{\theta,i}^{\text{neo}}$ and $v_{\theta,\alpha}^{\text{neo}}$, respectively, which can be derived from equation (2.32), are given by [35]:

$$v_{\theta,i}^{\text{neo}} = \frac{1}{2} v_{th,i} \rho_i \left(K_1 \frac{1}{L_{T_i}} \right) \frac{BB_\phi}{\langle B^2 \rangle} = \frac{1}{2e} f(\Psi) k(\Psi) \frac{\partial T_i}{\partial \Psi} B_\theta \quad (2.33)$$

$$v_{\theta,\alpha}^{\text{neo}} = \frac{1}{2} v_{th,i} \rho_i \left[\left(K_1 + \frac{3K_2}{2} \right) \frac{1}{L_{T_i}} - \frac{1}{L_{p_i}} + \frac{Z_i T_\alpha}{Z_\alpha T_i} \frac{1}{L_{p_\alpha}} \right] \frac{BB_\phi}{\langle B^2 \rangle} \quad (2.34)$$

where $v_{th,i}$ is the thermal velocity of the main ions, ρ_i is the ion Larmor radius, K_1 and K_2 are the collisionality-dependent viscosity coefficients as defined in [35], $f(\Psi) = RB_\phi$ and $k(\Psi)$ are flux functions. L_{T_i} denotes the ion temperature gradient scale length with $L_{T_i}^{-1} = d(\ln T_i)/dr$, while L_{p_i} is the ion pressure gradient scale length. Note that for the main ion poloidal rotation velocity (2.33) the ion temperature gradient is crucial, while for the impurity poloidal rotation velocity also the pressure gradient scale length of the main ions is important. The impurity pressure gradient contribution is small as it is multiplied by Z_i/Z_α . In the edge

transport barrier of H-mode plasmas (see section 2.3), the impurity poloidal rotation velocity can reach large values due to the steep ion pressure gradient ∇p_i . The impurities typically rotate in the electron diamagnetic drift direction. The main ion poloidal rotation velocity can be close to zero or even change its sign (i.e. pointing into the electron or into the ion diamagnetic drift direction), depending on the ion parameters at the plasma edge, mainly on the ion collisionality $\nu_{*,i}$ which changes the neoclassical coefficient K_1 .

The conventional neoclassical approach (equation (2.33) and (2.34)) to main ion and impurity poloidal rotation velocities is used in this thesis to compare neoclassical calculations to the measured poloidal rotation velocity. Furthermore, full neoclassical models such as NEOART [38], NEO [45] and HAGIS [46] are compared to the measurement.

2.3 The High-confinement mode (H-mode)

2.3.1 Edge Transport Barrier (ETB)

In tokamaks, the confinement time depends on the edge density and temperature profiles, which set boundary conditions for the profiles in the plasma core. Understanding the transport at the plasma edge is, therefore, of crucial importance in present and next-step fusion devices. A high energy confinement regime, the H-mode [3], occurs spontaneously in a divertor tokamak like ASDEX Upgrade (AUG) when power is injected. The transition into H-mode is characterized by a sudden change in plasma confinement, resulting in a global rise of temperature and density and an increase in stored energy. An edge transport barrier (ETB) is observed to emerge causing a reduced level of particle and heat transport perpendicular to the magnetic field. The ETB is responsible for the steep edge temperature and density gradients, thus, resulting in a steeper pressure profile compared to the L-mode (see figure 2.2). In this edge region the radial particle and energy transport is significantly reduced compared to the L-mode and to the plasma core, thus, leading to an improved confinement in the core. The steeper pressure gradient leads to an upward shift of the pressure profile along the whole plasma radius and a characteristic pedestal structure is formed which determines the increase in the particle and energy confinement found in the H-mode. The top of the pedestal lies just within the edge transport barrier (marked by an arrow in figure 2.2).

The characteristics of the barrier and the temperature value at the pedestal top are two of the factors determining how well the plasma, including impurities and the He ash, are confined. This is important as the presence of impurities leads to plasma dilution and radiation and might

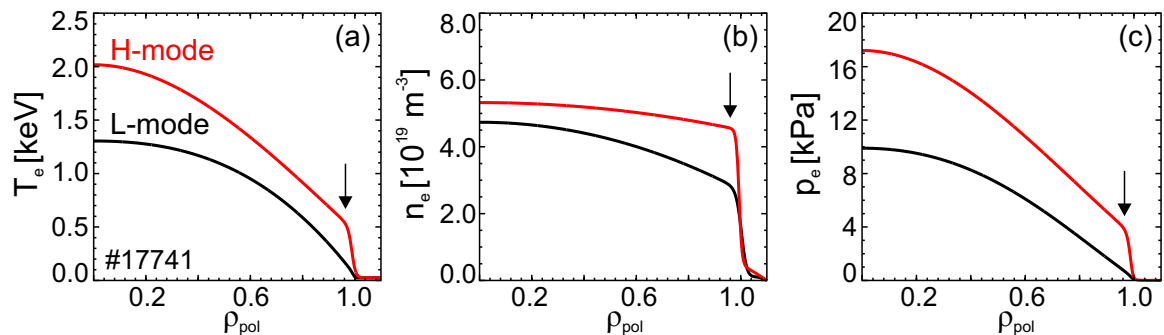


Figure 2.2: Kinetic electron profiles in L- and H-mode: (a) temperature, (b) density and (c) pressure (reprinted from [47]).

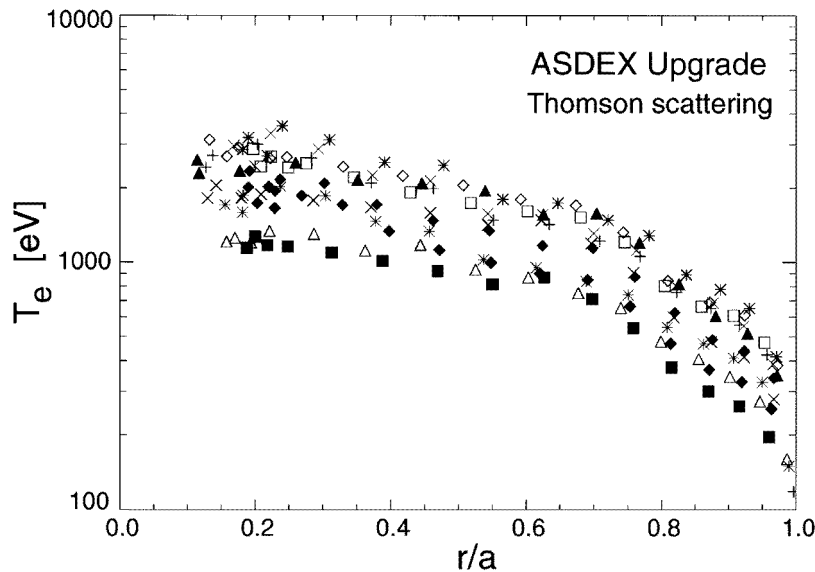


Figure 2.3: Profile resilience at AUG: Electron temperature (T_e) profiles in H-mode discharges (reprinted from [48]).

limit the performance of the fusion plasma. As the ETB exhibits short gradient scale lengths ($L_X = X/\nabla X$, where X is the temperature T , density n or pressure p) and is built up in a region bridging closed and open field lines, the transport modelling in the pedestal is quite complex. Full transport models are needed to explain the existence and the characteristics of the H-mode barrier, especially the pedestal height and width, which determine the boundary conditions for the transport in the core of the plasma. Due to the complexity of the pedestal behaviour, edge and core transport modelling are usually treated separately.

Since the 1980s, ‘profile resilience’ [48, 49] has been observed on many tokamaks. Profile resilience refers to the observation that the temperature profiles are ‘stiff’, i.e. they exhibit a strong trend to keep the same gradient lengths despite very different experimental conditions. The temperature profiles plotted on a logarithmic axis keep the same shape and are only shifted vertically depending on the edge temperature value (see figure 2.3).

The stiffness of the profiles arises from the fact that the ion and electron temperature profiles, T_i and T_e , are limited by a critical temperature gradient scale length $L_T = T/|\nabla T|$. Beyond this critical temperature gradient scale length the heat diffusivities increase [50] thus, resulting in profile stiffness. Hence, with stiff profiles the edge temperature is a key to attaining higher core temperatures and, therefore, higher confinement of the plasma. The physical mechanism of the core profile resilience is plasma turbulence driven by gradients, such as ion temperature gradient modes (∇T_i), trapped electron modes (∇T_e and partly ∇n_e) and electron temperature gradient modes (∇T_e). The turbulence is excited above a certain threshold of the normalized temperature and density gradient scale lengths, R/L_T and R/L_n where R is the major radius. In the pedestal region of H-mode plasmas, however, turbulent particle transport is strongly reduced due to the existence of strong radial gradients in the electric field \mathbf{E} perpendicular to the magnetic field \mathbf{B} [4]. The sheared electric field translates via $\mathbf{E}\times\mathbf{B}$ to a sheared plasma flow, which distorts the turbulent eddies and eventually tears them apart. It is widely accepted that the suppression of the edge turbulence via $\mathbf{E}\times\mathbf{B}$ velocity shearing leads to the formation of the pedestal and, therefore, to the H-mode and better confinement thanks to a reduced loss of energy and particles. Details on the $\mathbf{E}\times\mathbf{B}$ shearing model are presented in subsection 2.3.3

along with an alternative mechanism which could be responsible for the L-H transition. Access to the H-mode occurs above a certain power threshold P_{thr} [51], which increases with plasma density \bar{n}_e and toroidal magnetic field B_ϕ . The power threshold scaling $P_{thr} = 0.049 B_\phi^{0.8} \bar{n}_e^{0.72} S^{0.94}$, with S the plasma surface area, is only valid above a certain line averaged density. Below this critical value, the power threshold increases with decreasing density as observed in many devices [52, 53, 54, 55]. Experiments at AUG indicate that the transition appears to be closely related to the magnitude of the E_r well [56]. However, a full understanding of the transition from L- to H-mode has not yet been achieved.

2.3.2 Edge localized modes (ELMs)

Edge localized modes (ELMs) [57] are plasma edge instabilities that occur after the edge profiles steepen up to a limit that is thought to be defined by the peeling-ballooning limit [58, 59]. ELMs eject particles and energy from the pedestal region and cause a transient degradation of the edge pedestal. They appear as a periodic relaxation event and lead to a crash of the density and temperature gradients for a few 100 μs [60].

Figure 2.4 shows time traces of the (a) edge ion and electron temperature, (b) line-averaged edge electron density and (c) thermocurrents in the divertor which indicate the ELMs. After an ELM the gradients recover and build up again until the next ELM occurs. Each ELM produces energy losses between 1 and 10% of the total plasma energy and leads to large heat and particle loads on the divertor targets during a time period of about 1 ms. These loads can be high enough to cause damage and rapid erosion of these targets. Hence, small frequent ELMs are preferred to large and infrequent ELMs as the latter cause a much higher power load per ELM.

For the next step fusion experiment ITER [61] and for future fusion devices the control or even full suppression of ELMs is mandatory, while at the same time the pedestal top pressure, which determines the global energy confinement, should not be reduced.

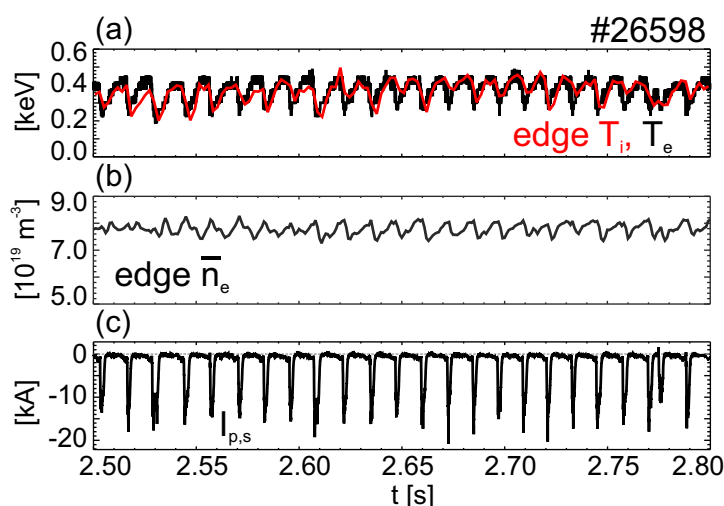


Figure 2.4: Temporal evolution of (a) the edge ion and electron temperature, (b) the line-averaged electron density at the plasma edge and (c) the thermocurrents in the divertor.

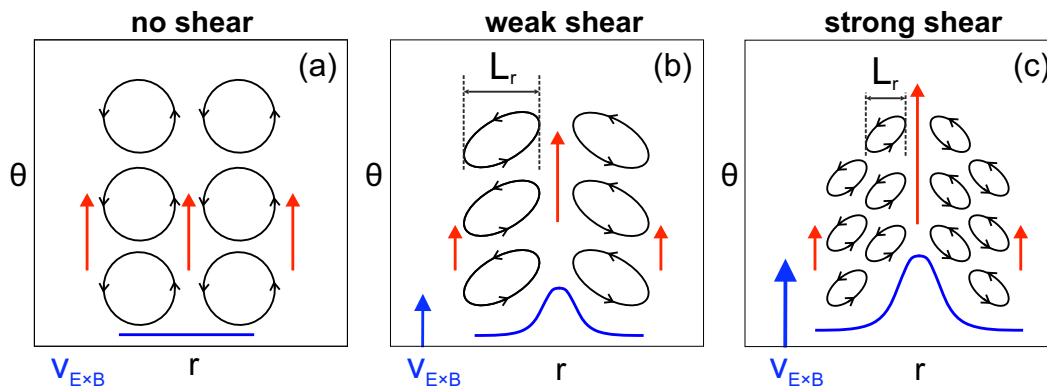


Figure 2.5: Basic principle of an $\mathbf{E} \times \mathbf{B}$ velocity shear acting on a turbulent eddy: The shear breaks up the structure of the eddies, reducing their radial correlation lengths, L_r , thus leading to turbulence suppression.

2.3.3 Turbulence suppression in sheared plasma flows

The most prominent candidate mechanism to explain the sustenance of the ETB is the existence of a strong radial shear in the plasma flow perpendicular to the magnetic field caused by a local radial electric field E_r . It is widely accepted that this $\mathbf{E} \times \mathbf{B}$ velocity shear is fundamental for suppressing edge turbulence [4] and thus, aiding the formation of the ETB and leading into H-mode.

In 1990, Biglari, Diamond and Terry [4] showed that an $\mathbf{E} \times \mathbf{B}$ velocity shear leads to the reduction of the radial correlation length of the turbulence and to the suppression of turbulent transport at the plasma edge. The $\mathbf{E} \times \mathbf{B}$ velocity shear decorrelates the turbulent eddies and changes the phase between density and potential fluctuations [62]. This results in reduced radial transport as the transport is determined by the $\mathbf{E} \times \mathbf{B}$ convection around the eddies. This decorrelation mechanism appears to be independent of the sign of both E_r and its shear.

Figure 2.5 shows a schematic picture of the physical mechanism of the turbulence decorrelation. In a constant background flow an eddy is carried along by the flow without being distorted (cf. figure 2.5(a)). If the background flow has a shear then the eddy will experience a distortion in the direction of the velocity flow and the eddy is elongated (see figure 2.5(b)). If the shear in the background flow is large enough, the eddy is torn apart (see figure 2.5(c)). Compared to the original eddy, the resulting elements have much smaller widths and thus, much smaller radial correlation lengths. The criterion for the shear decorrelation of the turbulent eddies is given by:

$$\left| \frac{\nabla E_r}{B_\phi} \right| > \frac{\omega_t}{k_\theta L_r}. \quad (2.35)$$

Here, ∇E_r is the radial gradient of E_r , B_ϕ the toroidal magnetic field, ω_t the lifetime of a turbulent eddy, k_θ^{-1} the poloidal elongation with k_θ being the poloidal wavenumber of the turbulence, and L_r the initial radial correlation length. The turbulent eddies are decorrelated if the shearing rate significantly exceeds the turbulence decorrelation time, i.e. decorrelation takes place when the background flow shear is strong enough. However, the turbulent energy is not reduced, but rather leads to a redistribution of the energy from large turbulent scales to smaller scales [37].

An alternative mechanism for reducing turbulent transport is vortex thinning [63]. Smaller eddies can be strongly elongated if the flow shear is large enough and can be reduced by a

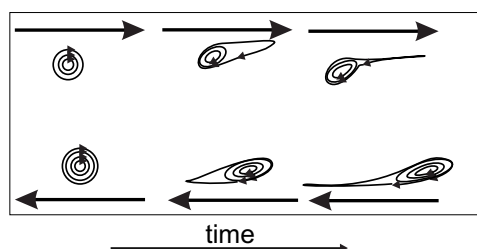


Figure 2.6: Straining-out process (reprinted from [63]): Small eddies are absorbed by the shear flow.

straining-out mechanism. During this process, the energy of the smaller eddies is absorbed by a zonal flow (as defined below) leading to a reduction of the turbulent fluctuation [63]. This mechanism efficiently reduces the turbulent energy. Figure 2.6 shows the basic concept of the straining-out mechanism. Smaller eddies are tilted, elongated and are pulled into the larger background flow shear, i.e. they are absorbed. It represents a non-local process, which transfers the vorticity from the microturbulence to the large-scale shear flow.

The $\mathbf{E} \times \mathbf{B}$ shear model [4] is, nowadays, the most widely accepted theory for explaining the formation of the ETB due to its success in explaining several observations across the L-H transition [12, 62]. Recent AUG experiments showed that a critical value of E_r of ~ 15 kV/m is needed to access the H-mode regime [56]. Thus, the background $\mathbf{E} \times \mathbf{B}$ shear flows caused by a sheared radial electric field might be the important player for the L-H transition. However, the dynamics of the transition into the H-mode regime remains ambiguous due to the associated timescales ($\sim \mu\text{s}$). In addition, turbulence itself could modify the sheared background flow via Reynolds stress [41], which couples the level of turbulence with the sheared flows and E_r . In more recent L-H transition theories the role of zonal flows as a possible trigger mechanism leading to the development of a transport barrier has been discussed [64, 65, 66]. These theories have characteristics of a predator-prey model, in which the background flow and the zonal flow are predators and the fluctuation level is the prey, and thus, imply that turbulence and E_r or the mean background flows need to be calculated self-consistently. Zonal flows are non-oscillating turbulence-driven $\mathbf{E} \times \mathbf{B}$ flows with finite radial extent and are homogeneous in the poloidal and toroidal directions [64, 65]. Hence, zonal flows cannot drive radial transport and cannot tap energy directly from the free energy sources, such as ∇T , ∇n , but indirectly from the turbulence (which is driven by the gradient) [65].

Zonal flows can be excited by all types of microinstabilities and can cause transport reduction [37]. The nonlinear damping of zonal flows leads to coherent flow oscillations, so-called geodesic acoustic modes (GAMs), which are localized in a narrow radially extended region at the plasma edge. AUG results [67] support that GAMs provide the main turbulence shearing mechanism in the L-mode regime and, together with the background flow, might be the trigger for the shear-flow turbulence suppression feedback loop to enter into the H-mode [68]. These oscillations as well as the turbulence-driven $\mathbf{E} \times \mathbf{B}$ zonal flows play an important role in regulating turbulent transport as they can amplify the background flow shearing of turbulent eddies and also constitute an additional energy sink via collisional and/or Landau damping [64].

However, as described above, the fluctuation level is also influenced by the background sheared flows via tilting and stretching the turbulent eddies. An anisotropy is created which stimulates the Reynolds stress drive leading to an autonomous zonal flow amplification. Thus, the $\mathbf{E} \times \mathbf{B}$ shearing rate, turbulence and transport are tightly intertwined in multiple feedback loops.

Other trigger mechanisms [6] that can modify E_r and lead to the transition into H-mode are,

amongst others, ion orbit loss [69], turbulent Reynolds stress [41] and poloidal spin up due to Stringer instabilities [70, 71].

Despite extensive study by both the theoretical and experimental fusion communities, the actual mechanism responsible for the L-H transition is not completely elucidated. The self-consistent evolution of the E_r profile, pedestal shape and improvement in plasma confinement are one of the fundamental open issues. Hence, detailed measurements of E_r are highly desirable to get a better understanding of the $\mathbf{E} \times \mathbf{B}$ shear and its connection to the transition from L- to H-mode.

Chapter 3

Edge diagnostics and experimental techniques at ASDEX Upgrade

At the plasma edge the requirements for temporal and spatial resolution are considerably more demanding than in the plasma core due to the fast transport phenomena and steep gradients. This is one of the main reasons why special attention is necessary for the edge measurements. In order to study the interconnection between the edge radial electric field (E_r) and the edge transport barrier (ETB) it is important to gather data from all available edge diagnostics. This chapter gives an overview of the edge diagnostic systems available at ASDEX Upgrade (AUG), with special focus on the measurement techniques used in this thesis. Details on the edge charge exchange recombination spectroscopy diagnostics, which have been installed and upgraded in the course of this thesis, are presented in section 4.

3.1 Measurements of plasma parameters

At AUG temperature, density and rotation profiles of impurity ions are measured using charge exchange recombination spectroscopy (CXRS) as diagnostic tool. From these measurements the radial electric field, E_r , can be evaluated using the radial force balance (equation (2.18)) for impurity ions. The basic principles of CXRS are discussed in section 3.1.1. Another diagnostic technique capable of measuring E_r is Doppler reflectometry which measures the perpendicular velocity of density fluctuations, u_{\perp} . With knowledge of the magnetic field B the radial electric field can be directly obtained using the relation $E_r = u_{\perp}B$. Details on the diagnostic principle are given in section 3.1.2.

The electron temperature profiles are measured using the electron cyclotron emission (ECE) and the Thomson scattering (TS) diagnostics, while the electron density profiles are obtained via TS, impact excitation spectroscopy at a Lithium beam and laser interferometry, which are described in section 3.1.3. Using the radial plasma sweep technique (see section 3.2) and combining all measurements, detailed edge kinetic profiles can be obtained. However, special attention is required when combining the measured data as the profiles need to be aligned in order to map them along the normalized poloidal flux coordinate, ρ_{pol} . This method is presented in section 3.3.

Figure 3.1(a) shows a poloidal cross-section of AUG indicating the measurement locations of the various systems, which will be presented in detail below, while figure 3.1(b) shows the lines of sight in a top-down view of the AUG vessel. In figure 3.1(a) only one line of sight

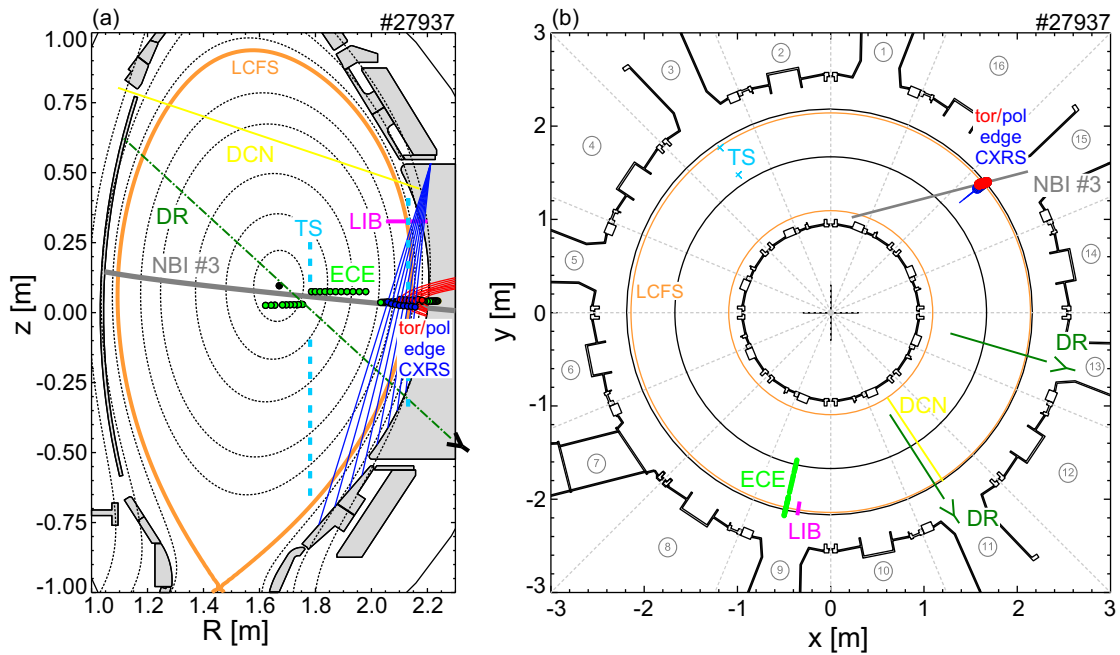


Figure 3.1: (a) Poloidal cross-section and (b) top-down view of AUG showing the measurement locations of various diagnostics. The last closed flux surface (LCFS) is shown in orange.

is shown for the Thomson scattering (TS), interferometry (DCN) and Doppler reflectometry (DR) systems. The last closed flux surface (LCFS, also called separatrix) is shown in orange.

3.1.1 Charge Exchange Recombination Spectroscopy (CXRS)

Basic principles of CXRS

Charge exchange recombination spectroscopy (CXRS) [5, 72, 73] is the most common method used to measure the ion temperature and rotation in a tokamak plasma. The technique exploits spectral lines which are produced by charge transfer from a neutral species, usually deuterium (D) or hydrogen (H), into excited states of impurity ions:



The recombined ion is born in an excited state and during the subsequent decay it emits photons $h\nu$ at characteristic wavelengths, which can be observed via dedicated spectrometers. The observation of these spectral emissions for diagnostic purpose is CXRS. The resulting spectrum gives information on the emitting ion species.

The neutral atoms (H or D) are typically injected into the plasma via neutral beam injection (NBI) and induce CX processes. Along the neutral beam line a local CX signal is measured since the impurity ions radiate in the region where the lines of sight (LOS) of the CXRS diagnostic intersect the path of the neutral beam particles. The light emitted due to charge exchange (CX) reactions between fully ionized impurities and injected neutral atoms yields localized information on impurity ion temperature and velocity from the Doppler widths and Doppler shifts of the measured spectra. Impurity densities are obtained from the radiance of the measured spectral line.

Typically, CXRS diagnostics analyze emission lines from low-Z impurities, such as boron or

carbon, rather than from high-Z elements or from main ions (usually deuterium at AUG). The impurity concentrations of high-Z elements are typically too low for CXRS and high-Z impurities are usually not fully stripped, i.e. the emission from a given transition is localized to a shell within the plasma in which the charge state of the ion exists. Low-Z impurities are fully stripped throughout the plasma volume enabling CXRS measurements to be obtained in the plasma edge as well as in the core. For the application to D, background emissions and the beam halo [74], i.e. charge exchange between beam neutrals and bulk ions, prevent a simple interpretation of the spectra.

For thermal neutrals the radiance of the CX signal observed by a LOS of a CXRS diagnostic is given by

$$L_{CX}(\lambda) = \frac{h\nu}{4\pi} \int_{LOS} \sum_{n=1}^{n_{max}} n_{\alpha,Z} n_{N,n} \langle \sigma_n v \rangle_{\text{eff},\lambda} dl \quad (3.2)$$

where $n_{\alpha,Z}$ is the density of the impurity α in ion stage Z , $n_{N,n}$ the neutral density with main quantum number n and $\langle \sigma_n v \rangle_{\text{eff},\lambda}$ the effective CX rate coefficient. $\langle \rangle$ indicates the Maxwellian average over the cross-section σ and the relative velocity v between the reaction partners, i.e. $v = |\mathbf{v}_{N,n} - \mathbf{v}_{\alpha,Z}|$ with $\mathbf{v}_{N,n}$ being the velocity of the neutral and $\mathbf{v}_{\alpha,Z}$ the velocity of the impurity in ionization stage Z . Here, the integration is along the LOS and the contributions from all states of the hydrogen or deuterium neutrals (ground and excited states) are summed up. The formula may be rewritten if the radiance of a transition that has been excited by CX with a neutral beam is considered:

$$L_{CX}(\lambda) = \frac{h\nu}{4\pi} \sum_{n=1}^{n_{max}} \sum_{k=1}^{n_b} \langle \sigma_n v \rangle_{k,\text{eff},\lambda} \int_{LOS} n_{\alpha,Z} n_{N,k,n} dl \quad (3.3)$$

where all beam components n_b are summed up. $\langle \sigma_n v \rangle_{k,\text{eff},\lambda}$ is the effective CX rate coefficient of the specific transition including the velocity of the k -th beam component and the neutral density of each beam component n_k . The radiance of the CX signal yields information on the impurity density if the neutral beam density is known at each intersection point of the LOS of the CXRS diagnostic with the neutral beam. The neutral density of the beam and the associated beam halo is obtained via modeling of all beam components taking into account the beam geometry and the measured kinetic profiles. Several neutral excited states have to be considered as the CX cross-sections depend on energies and n -levels [74]. The local neutral beam density may also be derived from beam emission spectroscopy [75].

The assumption of a constant impurity density in the volume where the beam crosses the LOS is made and thus, n_α is determined by:

$$n_\alpha = \frac{4\pi}{h\nu} \frac{L_{CX}(\lambda)}{\sum_n \sum_k \langle \sigma_n v \rangle_{k,\text{eff},\lambda} \int_{LOS} n_{N,k,n} dl}. \quad (3.4)$$

As the impurity ions have a Maxwellian velocity distribution, also the line-integrated spectra obtained from CXRS have a Maxwellian distribution, which leads to a Gaussian line shape:

$$I_{CX}(\lambda) = I_0 \sqrt{\frac{m_\alpha c^2}{2\pi k_B T_\alpha \lambda_0^2}} \cdot \exp \left[-\frac{m_\alpha c^2}{2k_B T_\alpha} \frac{(\lambda - \lambda_0)^2}{\lambda_0^2} \right]. \quad (3.5)$$

Here, $I_{CX}(\lambda)$ is the line shape function of the CX line normalized to a radiance of 1, I_0 the observed radiance, m_α the mass of the species α , c the speed of light, k_B the Boltzmann

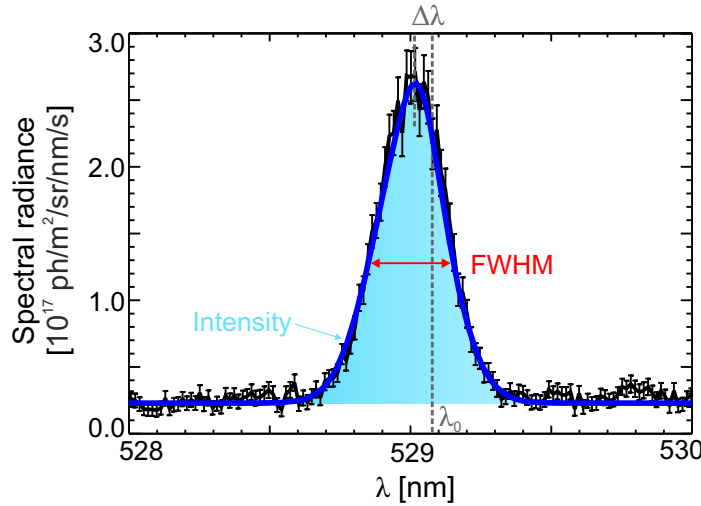


Figure 3.2: CXRS spectrum: The Doppler shift, width and intensity of the spectral line give information on the rotation velocity, temperature and density of the observed species.

constant, T_α the temperature of the considered species and λ_0 the theoretical wavelength of the measured spectral line. Figure 3.2 shows an example spectrum. Note that though the CX emission results from $A^{(Z-1)+}$, the CXRS measurements represent the original ion population A^{Z+} and the CXRS spectra contain the information of the fully ionized impurity ion. The temperature of the species is determined by the Doppler broadening of the spectral line and is proportional to the width of the distribution:

$$T_\alpha = \frac{m_\alpha c^2}{8 \ln(2) \lambda_0^2 e^2} \text{FWHM}^2 \quad (3.6)$$

where FWHM is the full width at half maximum. Here, it is assumed that Doppler broadening is the dominating line-broadening mechanism. In this work, $T_\alpha \approx T_i$, T_i being the main ion temperature, since the energy equilibration time between impurities and main ions is short ($\sim \mu\text{s}$) compared to local transport time scales ($\sim \text{ms}$). Thus, this quantity is denoted as the ion temperature T_i throughout this thesis.

The Doppler shift of the spectral lines, $\Delta\lambda$, is directly connected to the rotation velocity $\mathbf{v}_{rot,\alpha}$ of the considered species α :

$$\frac{\Delta\lambda}{\lambda_0} = \frac{\mathbf{v}_{rot,\alpha} \cdot \mathbf{e}_{LOS}}{c} \quad (3.7)$$

where \mathbf{e}_{LOS} is the unit vector along the LOS.

A combination of poloidal and toroidal views of the plasma enables the measurement of the impurity ion temperature, density and poloidal and toroidal rotation velocity. Thus, the radial electric field, E_r , can be calculated directly from these measurements (see chapter 5). A detailed description of the setup of the edge CXRS systems at AUG is given in chapter 4.

3.1.2 Doppler reflectometry

Doppler reflectometry (DR) [19] is a diagnostic technique which uses backscattering of electromagnetic waves and provides a complementary method for measuring E_r profiles. DR uses a microwave beam which is launched obliquely into the plasma with a tilt angle θ relative to the normal onto the plane cutoff layer. The incident beam is reflected, and, in the presence of

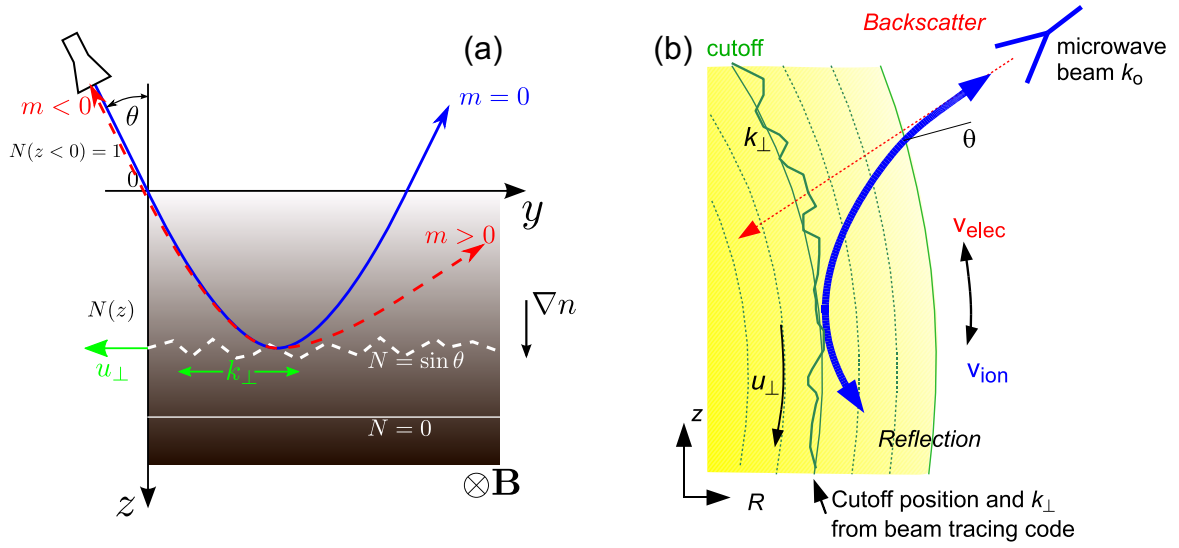


Figure 3.3: The principle of Doppler reflectometry: (a) backscattering of an oblique microwave beam in a slab plasma geometry (adapted from [78]), (b) in real geometry (reprinted from [79]).

fluctuations, Bragg scattered at a cutoff surface in the plasma. The refractive index N is determined by the wave equation which is derived from the Maxwell equations and the two-fluid MHD equations [1, 76]. For the ordinary mode (O-mode), where the electric field \mathbf{E} of the wave is parallel to the static magnetic field \mathbf{B}_0 of the plasma, N is given by:

$$N^2 = 1 - \frac{\omega_p^2}{\omega^2}. \quad (3.8)$$

Here, ω_p is the plasma frequency and ω the angular frequency of the wave. For oblique incidence the wave is at a plane cutoff surface when the refractive index reaches a minimum at $N = \sin \theta$ and is reflected, while it is resonant with the plasma when N approaches infinity and the wave does not propagate further. For normal incidence, as is the case in conventional reflectometry, cutoff occurs at $N = 0$ and $\omega^2 = \omega_p^2$.

For the extraordinary mode (X-mode), where the electric field of the wave is perpendicular to the magnetic field, $\mathbf{E} \perp \mathbf{B}_0$, the index of refraction at oblique incidence is given by [77]:

$$N^2 = 1 - \frac{\omega_p^2 \omega^2 - \omega_p^2}{\omega^2 \omega - \omega_h^2} \quad (3.9)$$

with ω_h the upper hybrid frequency $\omega_h^2 = \omega_p^2 + \omega_c^2$ and ω_c the gyro-frequency as defined in section 2.1. The cutoff condition for the X-mode, equation (3.9), yields two solutions, the right-hand and left-hand cutoff frequencies, ω_R and ω_L .

In the case of a corrugated cutoff layer, when turbulence is present at the cutoff surface (see figure 3.3(a)), the wave is also scattered. For coherent microwave scattering the momentum conservation equation holds [80] and the wave vector \mathbf{k} of the fluctuations is given by the difference of the scattered wave vector \mathbf{k}_s and the incident wave vector \mathbf{k}_i , i.e. $\mathbf{k} = \mathbf{k}_s - \mathbf{k}_i$. The backscattered reflected wave is either detected by a nearby antenna or by the same launching antenna. For a setup where the scattered microwave is measured by the launching antenna the diffraction pattern of the -1st order is selected (Bragg backscattering) [79]. Thus, the Bragg condition is $k_\perp = 2k_0 \sin \theta$, where k_\perp is the turbulence perpendicular wavenumber and k_0 is the

probing wavenumber.

The spectrum of the backscattered microwave is Doppler shifted by $\omega_D = \mathbf{u} \cdot \mathbf{k}$ and gives information on the velocity of the plasma fluctuations, \mathbf{u} , and on its wavenumber \mathbf{k} . By aligning the reflectometer perpendicular to the magnetic field such that the antenna is only sensitive to the perpendicular wavenumber, the Doppler shift results in $\omega_D = u_\perp k_\perp$, where u_\perp is the perpendicular velocity of the electron density fluctuations and k_\perp their perpendicular wavenumber. The perpendicular wavenumber of the turbulence fluctuations and the actual cutoff position are obtained from ray tracing calculations, which take into account the real geometry, i.e. the curvature of the magnetic flux surfaces (see figure 3.3(b)), using the density profile and the magnetic equilibrium as inputs [79].

With knowledge of the perpendicular wavenumber, u_\perp is determined directly from the measured Doppler shift ω_D . The perpendicular velocity corresponds to the sum of the $\mathbf{E} \times \mathbf{B}$ velocity of the plasma ($v_{\mathbf{E} \times \mathbf{B}}$) and the phase velocity of the density fluctuations (v_{ph}), $u_\perp = v_{\mathbf{E} \times \mathbf{B}} + v_{ph}$. Usually, v_{ph} is assumed to be negligible: an assumption that is supported by comparative measurements performed, amongst others, at W7-AS [81], TJ-II [82], DIII-D [83] or AUG in the plasma core [24]. Hence, knowing the magnetic field B , u_\perp gives a direct measure of the radial electric field E_r :

$$E_r = u_\perp B = \frac{\omega_D B}{k_\perp}. \quad (3.10)$$

As such, the measured Doppler shifts, the position of the cutoff layer of the probing wave and k_\perp are required to derive the E_r profile.

At AUG the edge DR system consists of two identical V-band Doppler reflectometers (frequency range of 50–75 GHz) [23, 84, 85], which have steppable launching frequencies with X- or O-mode polarization. Two pairs of bistatic antennas (one being the launching and the other the receiving antenna) are used for each polarization. The edge system is complemented by a core system which uses a W-band Doppler reflectometer (75–110 GHz, O- or X-mode polarization) [86, 87]. The time resolution of the DR diagnostics is in the μs -range, while the radial resolution, which depends on the wavenumber sensitivity of the diagnostics, is < 1 cm at AUG.

Comparing the E_r profile derived from CXRS to the one obtained with DR enables a validation of the E_r measurements. In chapter 5 a comparison of these measurements at the plasma edge of AUG is presented.

3.1.3 Electron temperature and density measurements

Electron cyclotron emission (ECE)

The electron cyclotron emission (ECE) of the plasma gives information on the electron temperature T_e . The electrons emit radiation at the angular electron cyclotron frequency $\omega_{c,e} = \frac{eB}{m_e}$ and its harmonics $\omega_k = k \omega_{c,e}$ while gyrating around the magnetic field lines. In optically thick plasmas, i.e. assuming that T_e is equal to the radiation temperature at the cold resonance position of the measured frequency, the intensity at the cyclotron frequency equals the Planck curve. Due to the Maxwellian velocity distribution of the electrons and when the measured plasma element is optically thick, Planck's law of black-body radiation holds. For high temperatures, this results in the classically derived Rayleigh-Jeans expression:

$$I_\omega = \frac{\omega^2}{2\pi^2 c^2} k_B T_e \quad (3.11)$$

where I_ω is the spectral radiance at a given frequency ω . In optically thick plasmas the measured emission region is identified with the position of cold resonance $\omega_{c,e}$ (neglecting relativistic and Doppler effects when the ECE antenna is measuring radiation perpendicular to the magnetic field B). Owing to the spatial variation of B in a tokamak configuration ($B \propto 1/R$), the location of the emission can be identified. Thus, by measuring the spectral radiance at the corresponding frequency, the electron temperature can be deduced directly via the Rayleigh-Jeans approximation. In general, the optically thick plasma approach is applied. If the plasma is optically thin the assumptions of black-body radiation and discretely localized emission are not applicable due to the shine-through effect. The shine-through peak, i.e. an increased radiation temperature measured around the separatrix and in the near scrape-off layer, is observed when T_e exhibits a steep gradient in a low density region [88] (e.g. at the plasma edge of H-modes).

At AUG the ECE diagnostic consists of a heterodyne microwave radiometer which measures the spectral radiance at 60 different frequencies between 89 and 187 GHz [89]. The system is based on measuring the second harmonic of the ECE in the extraordinary mode (X-mode). It has a high frequency resolution (300 or 600 MHz bandwidth) and therefore, a high radial resolution (up to 1 cm). The sampling rate of the diagnostic with the standard acquisition time is 32 kHz, thus enabling highly temporally resolved T_e profiles to be obtained. A new acquisition system was recently installed enabling sampling rates of up to 1 MHz.

Thomson scattering (TS)

The technique of incoherent scattering of laser light is the most common diagnostic tool to measure the electron temperature (T_e) and density (n_e) in tokamaks. Thomson scattering (TS) is based on elastic scattering of an electromagnetic wave by a charged particle (here, free electrons). The particle gets accelerated by the electromagnetic wave and while it accelerates it emits radiation and the wave is scattered. The Doppler effect has to be taken into account for the scattered radiation since the particle moves relative to the incident wave, but also relative to the scattered wave. Hence, the scattered wave is Doppler-shifted by

$$\Delta\omega = \mathbf{v} \cdot (\mathbf{k}_i - \mathbf{k}_s) \quad (3.12)$$

where \mathbf{v} is the velocity of the charged particle, \mathbf{k}_i is the wave vector of the incident wave and \mathbf{k}_s the wave vector of the scattered wave. In tokamaks, TS is usually performed at a scattering angle of about 90° and due to $m_e \ll m_i$ (m_e being the electron mass and m_i the ion mass) mainly electrons are accelerated and emit radiation. The Doppler width of the measured scattered spectrum gives information on T_e . In addition, the intensity of the scattered radiation is proportional to n_e , thus allowing for a simultaneous measurement of T_e and n_e .

At AUG edge T_e and n_e profiles are measured with the standard multi-pulse Nd-YAG (neodymium yttrium aluminium garnet) laser TS diagnostic, which consists of an edge and a core system [90]. The edge (core) system employs six (four) 20 Hz laser beams (with a pulse energy of about 1 J and a pulse duration of 10 ns) with a diameter of about 2 mm which are launched vertically through the plasma edge (core). The scattered light is collected through a horizontal port via 10 (16) four channel polychromators allowing simultaneous n_e and T_e measurements at the same radial position to be obtained. The spectral ranges of the four channels of the polychromators are determined by interference filters which are set up in front of avalanche diodes. The spatial range of the edge TS system can be extended using the radial plasma sweep technique (see section 3.2). The repetition rate of the diagnostic is 8 ms, while

the radial resolution is 3 mm for the edge system and 25 mm for the core system [90]. Complete, detailed radial T_e profiles are obtained by combining the profiles measured with the TS and ECE diagnostics, provided that the toroidal magnetic field is high enough to avoid the ECE propagation cut-off at high density.

Impact excitation spectroscopy on a lithium beam

Injecting a neutral lithium (Li) beam into the plasma allows the Li^0 resonance line at 670.8 nm, corresponding to the transition $\text{Li}^0(2p \rightarrow 2s)$ to be measured [91]. The injected Li atoms collide with the plasma particles and hence, the resulting emission profile is directly connected to the electron density, n_e . Ionization and charge exchange with the background plasma particles attenuate the Li beam, which restricts the measurements to the plasma edge (typically up to $\rho_{pol} = 0.95$, depending on the density). From the emission profile the electron density is calculated via a collisional-radiative model, which accounts for electron impact excitation, ionization and charge exchange.

At AUG neutral Li atoms are injected horizontally into the plasma, i.e. near the equatorial midplane of the torus, at an energy of 30 to 60 keV [92, 93]. The beam is observed with an optical head, which is equipped with 35 LOS. The emissivity of the $\text{Li}^0(2p \rightarrow 2s)$ transition is measured using interference filters and photomultipliers. The background radiation from the plasma is subtracted by chopping the Li beam periodically. The modulation periods of 56 ms beam on and 24 ms beam off are used to measure the background, thus allowing an accurate background subtraction in stationary plasmas [93]. For the study of transient events such as the L-H transition or the edge localized mode (ELM) cycle the modulation frequency of the beam chopping technique can be increased to 2 kHz. The Li beam diagnostic can be operated with a temporal resolution down to 50 μs , while the radial resolution is determined by the observation volume which has an extent of 5 mm.

DCN laser interferometry

Another method to measure the n_e profile is laser interferometry, which is based on the interaction of electrons with an electromagnetic wave with the additional dependence on the variation of the plasma refractive index N . N is directly connected to n_e :

$$N = \sqrt{1 - \frac{\omega_p^2}{\omega_0^2}} = \sqrt{1 - n_e \frac{e^2}{\epsilon_0 m_e \omega_0^2}} \quad (3.13)$$

$$\approx 1 - n_e \frac{e^2}{2\epsilon_0 m_e \omega_0^2} \quad (3.14)$$

where ω_p is the plasma frequency, e the elementary charge, ϵ_0 the electric constant, m_e the electron mass and ω_0 the angular frequency of the electromagnetic wave. Using a Taylor expansion, which holds if $\omega_0 \gg \omega_p$, the refractive index can be simplified to equation (3.14). The phase difference $\Delta\phi$ is measured by comparing the propagation of an electromagnetic wave along a path through the plasma to the propagation along a path through vacuum. This phase shift is proportional to the line-integrated electron density of the plasma. Introducing the classical electron radius $r_e = e^2/4\pi\epsilon_0 m_e c^2$, where c is the speed of light, and the vacuum

wavelength $\lambda_0 = 2\pi c/\omega_0$ of the laser, the phase shift can be described by:

$$\Delta\phi = \frac{\omega_0}{c} \frac{e^2}{2\epsilon_0 m_e \omega_0^2} \int n_e(x) dx = \lambda_0 r_e \int n_e(x) dx. \quad (3.15)$$

Here, x is the coordinate along the beam path.

At AUG the line-integrated electron density is measured along five channels using a phase-modulated Mach-Zehnder-type interferometer with a heterodyne detection system and a deuterium cyanide (DCN) laser [94, 95]. The DCN laser operates at a wavelength of 195 μm . At this wavelength, a phase shift of 2π translates to a line-integrated density of $5.7 \times 10^{18} \text{ m}^{-2}$. The sampling rate of the interferometer is 10 kHz. The system has a time resolution of 300 μs and enables the measurement of the line-integrated density along 5 distinct lines of sight through the plasma. The radial density profile is obtained via a deconvolution of the signal using an Abel inversion.

3.2 Radial plasma sweep technique

A radial sweep of the plasma edge through the lines of sight (LOS) of the diagnostics is performed to cover the whole plasma edge and to obtain full and very detailed edge profiles. Typically, the plasma position is moved by 2 cm in about 800 ms during a steady-state phase of the discharge (see figure 3.4(a)-(b)). The radial scan also allows the refinement of the relative sensitivity calibration of different LOS of the edge CXRS diagnostics (see chapter 4) as slight differences in the calibration show up as discontinuities in the spectral radiance profiles, after mapping the measurements onto the plasma coordinate system ρ_{pol} . Furthermore, this technique enables the alignment of the edge CXRS systems via the ion temperature and spectral radiance profiles.

In figure 3.4(a)-(d) several plasma parameters from an H-mode discharge, which includes a radial plasma sweep, are shown. The time period highlighted in yellow contains the radial scan of the plasma. Figure 3.4(e) shows the ion temperature profile as measured with the edge poloidal and toroidal CXRS systems, which are described in chapter 4.

The radial plasma sweep technique enables the alignment of the measured data obtained with different diagnostics and to align the electron and ion profiles relative to each other (see section 3.3). Hence, a high-accuracy alignment of E_r with respect to the edge kinetic profiles and to the separatrix position is possible.

3.3 Profile alignment

The kinetic profiles measured by each diagnostic are combined to reduce the uncertainties in the radial position, which arise due to the mapping onto the magnetic equilibrium. The various diagnostics measure at different toroidal and poloidal positions of the tokamak vessel, however, the profiles are aligned radially using the assumption of a toroidal symmetric magnetic equilibrium. The steep gradients in the edge transport barrier (ETB) of the H-mode allow for an accurate alignment of the profiles [97]. The measured data are ELM-synchronized, i.e. the measurements are selected relatively to the occurrence of ELMs to ensure that the profiles and their gradients are not obscured by ELMs.

For an accurate study of the plasma edge, the position of the separatrix must be known with

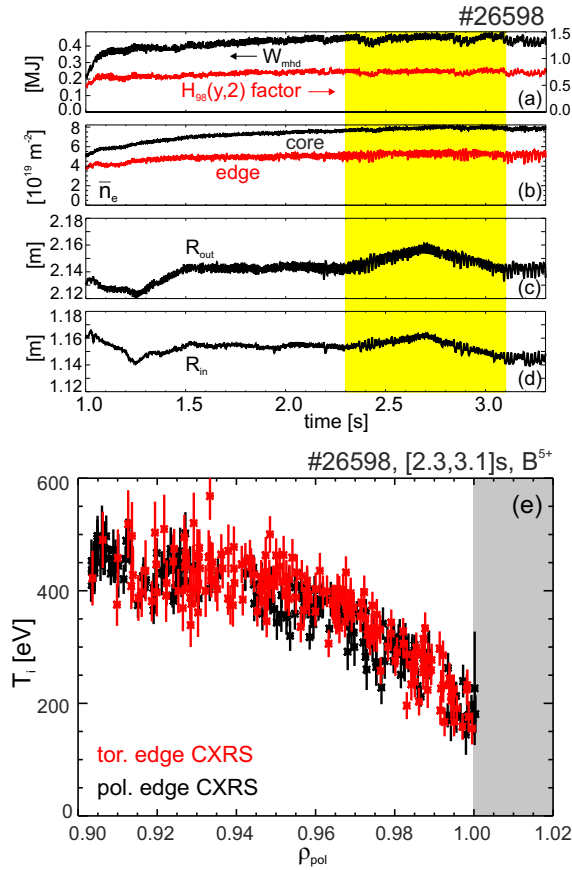


Figure 3.4: Plasma parameters from an H-mode discharge that includes a radial plasma sweep: (a) plasma stored energy W_{mhd} (black) and confinement factor (red) denoted by $H_{98}(y,2)$, which is the H/L scaling factor with respect to the ITER confinement scaling [96], (b) line-integrated electron density in the plasma core (black) and edge (red), (c) radial plasma position at outer midplane, (d) radial plasma position at inner midplane, (e) ion temperature profile, as measured with the toroidal and poloidal edge CXRS diagnostics (see chapter 4), plotted against the normalized poloidal flux coordinate ρ_{pol} obtained during the radial plasma scan highlighted in yellow.

sufficient accuracy. The nominal separatrix position is determined from the reconstruction of the magnetic equilibrium. However, this determination is not sufficiently accurate for H-mode edge transport analysis. Power balance and parallel heat transport studies using a 1D heat conduction model [98] and the measured parallel heat flux maximum in the divertor lead to the assumption that the true separatrix position is located at [99]:

$$T_{e,sep} = \left(T_{div}^{7/2} + \frac{7}{2} (P_{heat} - P_{rad}) \frac{L_c}{A_{q,\parallel} \kappa_0} \right)^{2/7} \quad (3.16)$$

where $T_{e,sep}$ is the electron temperature at the separatrix, T_{div} the divertor temperature, P_{heat} the heating power and P_{rad} the radiation power. L_c is the connection length, i.e. the distance from the midplane to the divertor target along a field line, $A_{q,\parallel}$ the surface area for the parallel power flux through which the power is entering the scrape-off layer and κ_0 the constant of the parallel heat conductivity $\kappa = \kappa_0 T_e^{5/2}$. In type-I ELMy H-mode discharges $T_{e,sep}$ is typically ≈ 100 eV. This condition holds in a variety of discharges due to the insensitivity of the model

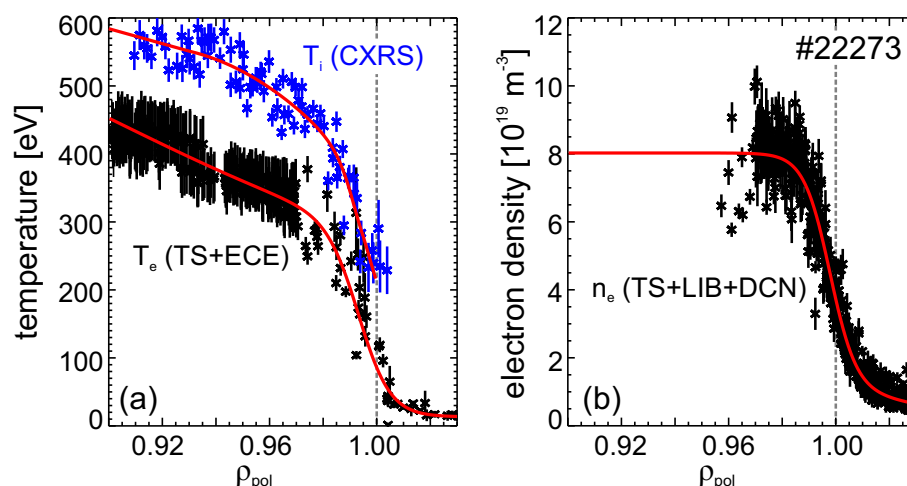


Figure 3.5: Radial profile alignment of T_i , T_e and n_e , adapted from [100].

to $T_{e,sep}$ which arises from the power dependence of $\frac{2}{7}$.

To optimize the radial profile alignment and to reduce the uncertainties due to the magnetic equilibrium, the following procedure is performed for the analysis of the radial electric field from the edge CXRS measurements: The T_e profile measured by TS is shifted such that $T_e \approx 100$ eV at the separatrix. The T_e profile measured by ECE is aligned to the profiles measured with TS such that the upper ETB region matches. Note that the region which is affected by the shine-through, which is typically the region around the separatrix and in the near scrape-off layer, is excluded since the measured radiation temperature is not directly correlated to T_e [88] (see section 3.1.3).

The n_e measurements obtained with the Li beam diagnostic are aligned to the profiles measured by TS, which has identical measurement volumes for both n_e and T_e . These measurements are complemented by those obtained with the interferometry system, which is used to constrain n_e at the pedestal top. To align the CXRS profiles relative to the electron profiles it is assumed that the position of the steepest gradients in T_i coincide with those in T_e . This assumption holds in high-collisionality plasmas [47], which are analyzed in this work.

Figure 3.5 shows the alignment of the T_i , T_e and n_e profiles. The shifts applied for the profiles are within the radial resolution of each diagnostic. The accuracy of this relative profile alignment is estimated to ~ 2 -3 mm as T_e is closely connected to the separatrix position. This enables the determination of the position of the radial electric field with respect to the electron profiles and the separatrix position with an accuracy of ~ 2 -3 mm, because T_i is part of the CXRS measurements and thus, is rigidly connected to the E_r profile.

When non-axisymmetric magnetic perturbations (MPs) [101] are applied to the plasma edge special care has to be taken when analyzing the measured data of different diagnostics since the MP field causes a toroidally non-symmetric equilibrium. When applying MPs in the $n = 2$ configuration, n being the toroidal mode number, it was found that the density profile mapped along the normalized poloidal flux label ρ_{pol} shows a displacement of about 4 mm compared to the phase without MPs, while in real space, i.e. as a function of the major radius, no displacement was observed [102]. The displacement of the profile results from an artefact in the interpretation of the magnetic measurements, which are used for the equilibrium reconstruction. Since the edge n_e , T_e and T_i profiles are measured by different diagnostics located in different sectors of the AUG vessel, the radial position of each diagnostic relative to the position of the magnetic measurements becomes important when interpreting the experimental

data. When mapping the profiles along ρ_{pol} the displacement varies and depends on the position of each diagnostic. The displacement due to the equilibrium distortion at the plasma edge caused by the MPs is taken into account in the analysis of the E_r measurements when MPs are applied (see chapter 6) and the same procedure as described above is used to align the ion and electron profiles.

Chapter 4

The edge CXRS diagnostics at ASDEX Upgrade

The most commonly used tool to derive radial electric field (E_r) profiles is active charge exchange recombination spectroscopy (CXRS) due to its relatively easy applicability in tokamak plasmas. This chapter gives details on the setup of the edge CXRS diagnostics [103] at ASDEX Upgrade (AUG), which have been designed, installed and upgraded in the course of this thesis. The data analysis techniques used in this work are discussed.

4.1 CXRS measurements at the low-field side of AUG

At AUG three toroidal CXRS systems viewing the core and the edge of the plasma at the low-field side (LFS) of the vessel (see figure 4.1) are installed to provide temporally and radially resolved CXRS profiles. During this thesis, the edge toroidal CXRS system was upgraded and complemented with a poloidal view to provide full edge rotation profiles at AUG, i.e. parallel and perpendicular to the magnetic field. Moreover, the measurements of the new poloidal edge system now enable the determination of the radial electric field from CXRS measurements. In general, all CXRS diagnostics on AUG use an in-vessel optical head which images the plasma onto several lines of sight (LOS). Optical fibers guide the collected light outside the torus hall to Czerny-Turner spectrometers which employ two objective lenses as optical elements.

The setup of the LFS edge toroidal system, which has been upgraded with a new spectrometer, is presented in the next subsection. Section 4.1.2 gives details on the poloidal edge CXRS diagnostic.

4.1.1 Toroidal edge CXRS system

The toroidal edge CXRS diagnostic was installed in 2007 [104] and since then has routinely provided edge ion temperature, toroidal rotation and impurity ion density profiles. It uses an in-vessel $f/4$ optical head which images the plasma edge at the outer midplane onto 8 LOS. The LOS are aligned such that they view the center of the neutral beam injection (NBI) source #3, which is a 60 keV deuterium (D) beam mounted in sector 15 (see figure 4.1). At AUG the NBI heating system consists of two injectors with four sources each that can deliver a total of 20 MW NBI power (2.5 MW each). The injectors are toroidally separated by 180° and on each

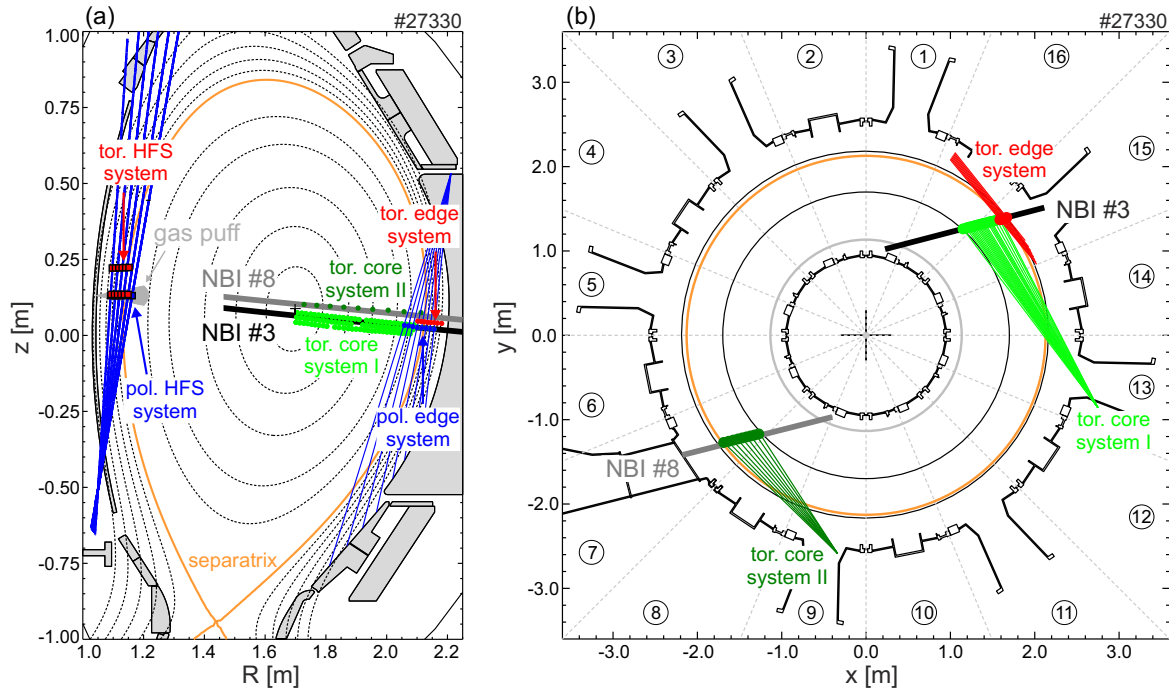


Figure 4.1: (a) Poloidal cross-section of AUG indicating the measurement locations of the CXRS diagnostics, (b) top down view of the AUG vessel showing the lines of sight of the toroidal LFS CXRS systems. The indicated beam lines do not correspond to the actual width of the beams (~ 25 cm).

injector one neutral beam source is used for CXRS measurements (NBI source #3 and #8, see figure 4.1). The injected neutrals have three different energy components since D^+ ions as well as D_2^+ and D_3^+ molecules are generated in the positive ion source.

The LOS of the toroidal edge CXRS diagnostic are separated by about 1 cm and each LOS is equipped with 3 optical fibers (with a diameter of $400 \mu\text{m}$) to improve the signal. At the outer midplane ($R = 2.15$ m) the toroidal curvature of the plasma across the width of the heating beam (~ 25 cm) limits the radial resolution. In order to optimize the radial resolution down to 3 mm the sight lines are realized by individual mirrors. These mirrors are Al mirrors coated with MgF_2 . Radial sweeps of the plasma (see section 3.2) are performed to cover the whole plasma edge and to provide radially dense profiles. In the plasma edge of AUG ($T = 500$ eV, $B = 2$ T), the typical Larmor radii of impurity species are of the order ~ 1 mm and smaller than the radial resolution. Thus, the measurements are averaged over the gyro-radii.

The toroidal edge CXRS diagnostic has been upgraded to increase the intensity level. The system has been equipped with a new spectrometer and a new CCD camera enabling 25 channels to be imaged on the chip simultaneously with a repetition time of 2.65 ms. Shorter exposure times are obtained by using fewer LOS and binning the CCD chip to fewer regions of interest. The CX emission collected along the LOS is transmitted by $400 \mu\text{m}$ fibers to a high throughput $f/4$ Czerny-Turner spectrometer, which utilizes a variable width entrance slit, two objective lenses (Leica APO-ELMARIT-R), and a movable grating with 2400 grooves/mm (see figure 4.2(a)). The spectrometer is coupled to a Princeton Instruments ProEM, back-illuminated, frame-transfer charge coupled device (CCD) camera with on-chip multiplication gain [105]. The latter allows for low light applications while maintaining short repetition times. The camera features a 512×512 $16 \mu\text{m}$ pixel chip which, when coupled with the spectrometer, provides

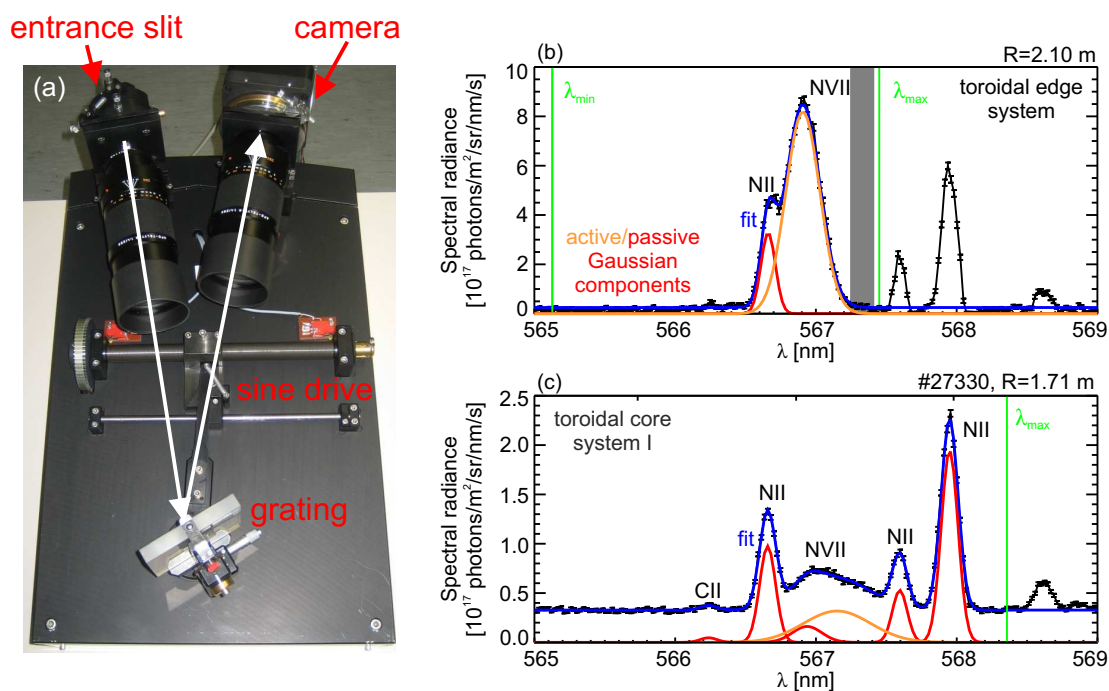


Figure 4.2: Left: (a) Setup of a lense-based Czerny-Turner spectrometer: The fibers, which guide the collected light from the torus to the spectrometer, are stacked vertically along the entrance slit. After passing through the entrance slit the light is collimated, then dispersed by a 2400 grooves/mm grating and focussed onto the camera. The sine drive enables the central wavelength of the spectrometer to be moved. Right: Example spectra from the toroidal CXRS diagnostics: (b) N^{7+} spectrum of the edge system, (c) N^{7+} spectrum of the core system I. The areas highlighted in grey as well as those larger (smaller) than λ_{max} (λ_{min}) are not used for fitting the spectra.

a 13.1 nm spectral range at a central wavelength of 494.5 nm. The entrance slit to the spectrometer is typically set to 50 μm , but can be adjusted to any value between 0 and 400 μm . For a slit width of 50 μm and a central wavelength of 494.5 nm the instrumental width of the spectrometer channels is in the range of 0.031 to 0.036 nm (slight variations of the different spectrometer channels arise due to imperfections of the entrance slit). The collimating lens at the entrance slit has a focal length of 280 mm, while the focusing lens has a focal length of 180 mm. This choice of lenses enables the light from 25 fibers, which are stacked vertically along the entrance slit, to be imaged concurrently on the camera. At a central wavelength of 494.5 nm, the dispersion of the spectrometer is 0.026 nm/pixel.

Compared to a mirror-based Czerny-Turner spectrometer the main advantage of using an optical layout based on objective lenses is the good imaging property (no astigmatism) of the system at high aperture. The ability to move the central wavelength of the spectrometer enables the system to make CX measurements of different impurity species. The system typically utilizes either the B^{5+} ($n = 7 \rightarrow 6$) CX line at 494.467 nm or the C^{6+} ($n = 8 \rightarrow 7$) CX line at 529.059 nm. However, it is also used for He^{2+} , N^{7+} and Ne^{10+} measurements. The toroidal edge CXRS diagnostic typically images 20 channels enabling a time resolution of 2.2 ms. One channel is always connected to a neon lamp which provides a wavelength calibration on a shot-to-shot basis (see section 4.3), thus reducing the instrumental uncertainties.

An example spectrum of the toroidal edge CXRS diagnostic is shown in figure 4.2(b). Here,

the edge system was set to the N^{7+} spectral line ($n = 9 \rightarrow 8$, $\lambda = 566.937$ nm). The N^{7+} spectra are typically fitted with 2 Gaussians, one accounting for the active N^{7+} line and one for a nearby passive N^{1+} line at 566.663 nm [106]. Passive spectral lines are emitted at the plasma edge, mainly due to electron impact excitation and CX with thermal neutral deuterium [107], and blend the active CX signal. The fit to the spectrum is shown in blue, while the Gaussian components are plotted in orange (active lines) and red (passive lines). For the edge system the passive N^{6+} component is negligible as it is very small compared to the active CX line. Figure 4.2(c) shows a typical spectrum obtained with the core system I, which also utilizes NBI #3. The core spectra are fitted with 6 Gaussians; one Gaussian for the active N^{7+} line, one for its passive component, 3 Gaussians accounting for 3 nearby passive N^{1+} lines at 566.663, 567.602 and 567.956 nm and one Gaussian for a passive C^{1+} line at 566.246 nm [106]. A discrimination between electron impact excitation and CX with thermal neutral deuterium [107] is not applied for the passive component as it is typically small compared to the active CX line. Note the difference in scale when comparing the spectral radiances between the core and edge systems, which reflects mainly the attenuation of the beam density. At the plasma edge (see figure 4.2(b)) the spectral radiance of the active line is 4.28×10^{17} photons/m²/sr/s while the full width at half maximum (FWHM) is 0.303 nm (corresponding to an ion temperature of $T_i = 670.5$ eV) and the absolute wavelength shift of the spectral line is 0.039 nm (equal to a rotation of $v_{rot} = 20.7$ km/s). In the core the signal is much lower due to the attenuation of the neutral beam. For the spectrum shown in figure 4.2(c) the radiance of the active line is 1.90×10^{16} photons/m²/sr/s, the FWHM of the spectral line is 0.544 nm ($T_i = 2167.9$ eV) while the wavelength shift is 0.193 nm ($v_{rot} = 103.9$ km/s).

4.1.2 Poloidal edge CXRS system

A newly installed poloidal edge CXRS diagnostic also utilizing beam #3 in sector 15 enables the measurement of poloidal impurity rotation profiles and provides the missing measurements for deriving the radial electric field from the radial force balance equation (2.18).

The diagnostic has been designed to obtain high spatial resolution (down to 5 mm) measurements of the plasma edge at AUG. The system features an $f/2.5$ optics mounted inside the vessel and employs one lense with a focal length of 40 mm. The radial resolution had to be compromised (by 2 mm compared to the toroidal edge system), because the poloidal curvature of the plasma is stronger than the toroidal one. The optical head has 8 LOS which view the edge of the plasma at the outer midplane. Each LOS is comprised of 2 fibers to enhance the signal. In the focal plane the radial distance between two adjacent LOS is 1.25 cm with a spot size of 5 mm. The in-vessel optical head has been aligned such that the 8 LOS view the edge pedestal in a poloidal plane and to ensure that no toroidal rotation component is picked up. Figure 4.3 shows an overview of the viewing geometry of the new system.

The collected light is transmitted to a high throughput $f/4$ Czerny-Turner spectrometer which is similar to the spectrometer used for the toroidal edge system. It employs two objective lenses both with a focal length of 280 mm. Thus, the light from 15 fibers can be imaged on the CCD chip simultaneously. Due to the expected small magnitude of the poloidal rotation velocity, the lenses of the spectrometer were chosen such that the spectrometer has a higher dispersion and thus, a larger spectral resolution compared to the one employed for the toroidal edge CXRS measurements. At a central wavelength of 494.5 nm, the dispersion of the spectrometer employed for the poloidal CXRS measurements is 0.016 nm/pixel.

The entrance slit of the spectrometer is typically set to a width of 50 μ m. At this slit width and

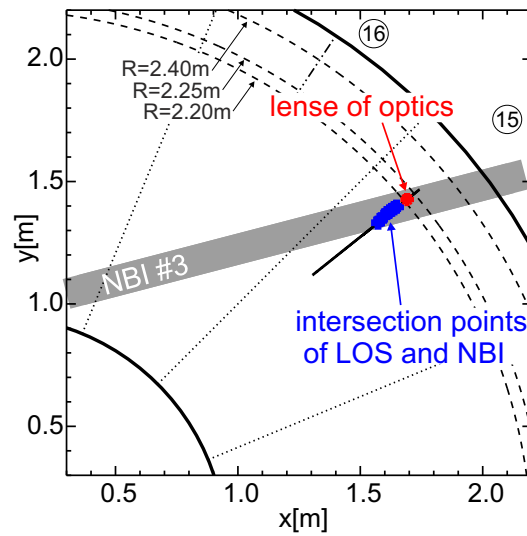


Figure 4.3: Viewing geometry of poloidal edge CXRS diagnostics: top down view of sector 15 indicating the collection regions of the poloidal system with respect to the path of the neutral beam.

at a central wavelength of 494.5 nm the instrumental width of the system is between 0.023 to 0.027 nm depending on the spectrometer channel. The collected photons are imaged onto a frame-transfer CCD camera (Princeton Instruments PhotonMax [105], 512×512 $16 \mu\text{m}$ pixels) capable of an electron multiplication readout. The CCD chip, coupled with the spectrometer, allows for a spectral range of 8.2 nm at a central wavelength of 494.5 nm. The spectra from 12 out of 16 fibers, which are connected to the optical head, are routinely measured with a repetition time down to 1.9 ms. Two channels of the spectrometer are connected to a neon lamp to provide a wavelength calibration measurement (see section 4.3). The poloidal system is typically set to 2.2 ms to obtain concurrent measurements with the toroidal edge CXRS diagnostic. Figure 4.4 shows an example spectrum of the B^{5+} spectral line along with the fit which includes a background and a passive component (B^{4+} , $n = 7 \rightarrow 6$). The spectrum is fitted with 3 Gaussians; one accounting for the active B^{5+} line, one for the passive component

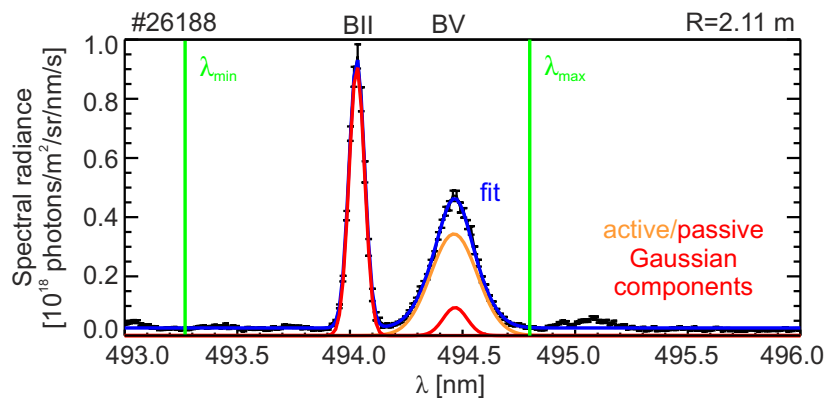


Figure 4.4: Example spectrum of the B^{5+} spectral line using a three Gaussian fit (one accounting for the active B^{5+} line, one for the passive component and one for the passive B^{1+} line); fit in blue, Gaussian components in orange (active line) and red (passive lines); the green lines mark the wavelength range used for the fit.

and one Gaussian for a nearby passive B^{1+} line at a theoretical wavelength of 494.038 nm. The lines marked in green in figure 4.4 show the wavelength range used in the fitting procedure. The measurements of the new poloidal diagnostic are validated by comparing the data to the measurements of the toroidal CXRS systems at the LFS (see section 4.4).

4.2 CXRS measurements at the high-field side of AUG

To study the flow structure and possible asymmetries on a flux surface, an array of CXRS diagnostics viewing the high-field side (HFS) of AUG has been installed. In contrast to the LFS CXRS diagnostics, which use a heating beam that provides the neutrals for the CX reactions, the CXRS diagnostics at the HFS utilize a deuterium (D) gas puff and collect the light, that is emitted after the impurity undergoes a CX reaction with a thermal D particle. Due to the penetration of the thermal D gas puff, the HFS measurements are restricted to the outermost region of the plasma.

The HFS array consists of a toroidal [108] and a poloidal view (see figure 4.5) and each view is equipped with two $f/4$ optical heads. For the toroidal system, one optical head views the gas puff directly, while the other views the background plasma parallel to the ‘active’ optical head (~ 10 cm above the ‘active’ view) and thus, collects the corresponding background spectra. Both optical heads are installed at the LFS and view through the plasma edge at the outer midplane, intersect either the diagnostic gas puff at the HFS or the plasma edge at the inner wall for the ‘background’ view, respectively. Then the views pass through the plasma edge at the other side (again LFS). Hence, the ‘background’ optical head collects passive emission from three separate regions along the LOS, while the ‘active’ optical head collects additional emission from the HFS region when the gas puff is switched on. Similarly, the poloidal system has one optical head viewing the gas puff directly, while the second views the background plasma at the same poloidal location, but at a different toroidal location (sector 3, see figure 4.5) to avoid the active CX signal. These are both installed at the HFS and thus, collect light from the plasma edge at the inner wall.

Due to the installation of two optical heads for each view, the background signals, i.e. the passive emission, can be subtracted from the active spectra. One issue associated with the

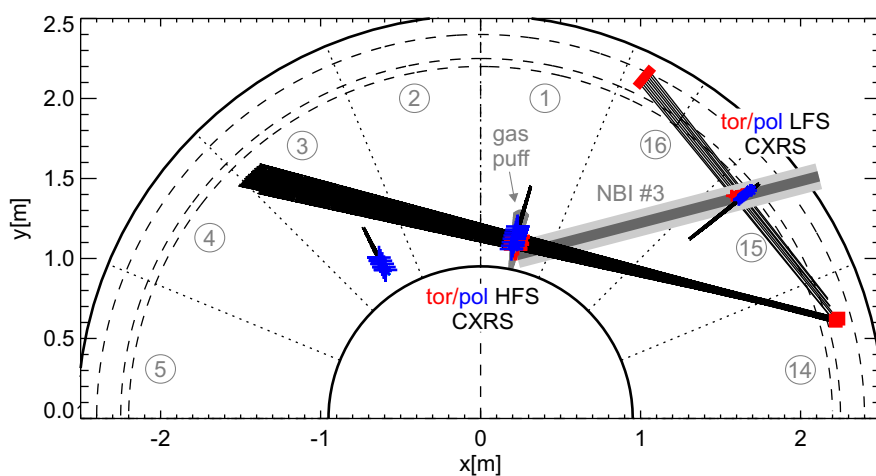


Figure 4.5: Top down view of AUG showing the collection regions (crosses) of the edge CXRS diagnostics. The optical heads are marked by rectangles.

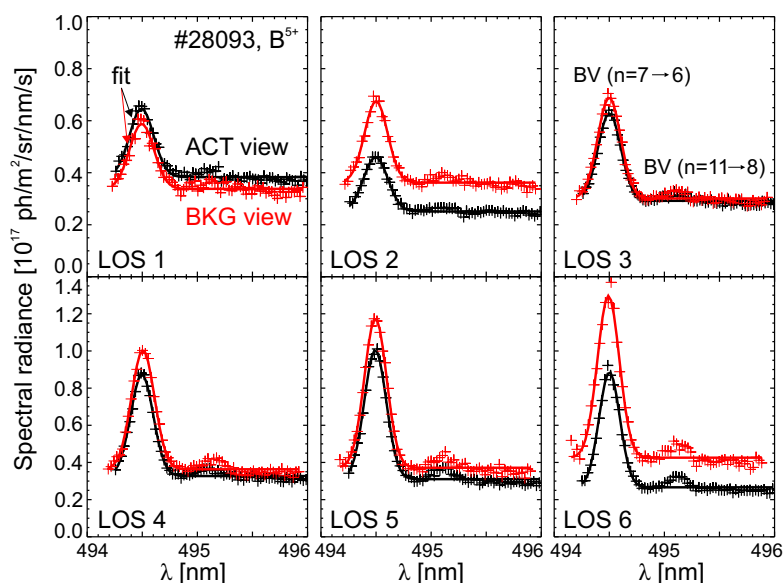


Figure 4.6: Relative calibration: Spectra obtained with the active (ACT) and background (BKG) toroidal HFS diagnostic shortly before the gas puff is applied.

background subtraction is the emission from molecular D_2 , which is injected from the HFS, and might disturb the fitting procedure. However, the molecules radiate in a very limited radial range in the near scrape-off layer. In the present work, the analysis is limited to the edge of the confined plasma where the D_2 molecules are already disassociated.

Each optical head is equipped with six LOS allowing a radial profile to be measured. In the focal plane the spot size of the LOS is 8.8 mm for the toroidal HFS system and 5 mm for the poloidal HFS diagnostic, while the channel spacing is 1.25 cm. The radial resolution can be increased by applying the radial plasma sweep technique (see section 3.2) and moving the plasma position towards the inner wall. All optical heads are aligned such that they view the plasma as tangential to the flux surfaces as possible. The collected light is transmitted to a high throughput $f/4$ Czerny-Turner spectrometer which has identical properties as the one employed for the toroidal edge CXRS system at the LFS.

To obtain measurements at the HFS thermal D is puffed from the inner wall for a certain time period. A few milliseconds before the gas puff is applied, a refinement of the calibration on the background channels relative to the active channels is performed. Relative calibration factors with respect to the corresponding active channels are calculated. Using this method the relative brightnesses of the active and background views, which arise due to imperfections of the calibration, are taken into account.

Figure 4.6 shows the measured spectra from the active and the background view, shortly before thermal D is injected. The spectra are fitted by a Gaussian function (solid line in figure 4.6) and the fitting region is restricted to the B^{5+} ($n = 7 \rightarrow 6$) spectral line. The relative calibration factors for each LOS are calculated from the ratio of the heights of the fitted Gaussians of the active and background LOS. For the example given in figure 4.6 the calibration factors for the different LOS vary between 0.67 and 1.05. To isolate the active CX line, the background spectra measured during the gas puff are multiplied by the corresponding calibration factors and subtracted from the active spectra. The Doppler shift and Doppler width of the measured active spectral line give information on the rotation velocity and on the ion temperature. The direct evaluation of the HFS impurity density profile from the measured radiance of the spectral

line is not yet available at AUG, as a neutral density measurement after the application of the gas puff is missing.

Corrections to the measurements due to the CX cross-section effects [109] (see section 4.5.1) are negligible since at thermal energies the cross-section has a weak dependence on the energy and hence, the temperature dependence of the effective CX reaction rate is small. The HFS measurements, combined with the data obtained from the LFS diagnostics, enables localized CXRS measurements at two different poloidal locations (see figure 4.1(a)) on a flux surface and allows for studying possible asymmetries on a flux surface (see chapter 5).

4.3 Characterization and calibration of CXRS diagnostics

For an accurate interpretation of the CXRS measurements, all components of the diagnostic need to be calibrated. A spatial calibration of the LOS of the systems is needed to know where in the torus the optical heads are focused. Together with the positions of the optical heads the geometry of the LOS can be determined. For the localization of the measurements the intersection of the views with the neutral beam are determined via a 3D model of the beam density and the LOS. A complete radiance calibration enables the calculation of absolute values for the impurity density profile. The instrument function of the systems needs to be measured accurately to deconvolve the spectra from the effect of the spectrometer's optics. Wavelength calibrations are required to provide accurate rotation velocity measurements. The techniques for the various calibrations are presented in this section.

Spatial calibration

The in-vessel setup of the diagnostics was adjusted by backlighting the optical fibers. The foci of the optical heads were aligned to the neutral beam #3 and gas puff, respectively, such that the radial resolution is maximized, i.e. viewing the plasma as tangential as possible. Backlighting the fibers also enables an in-vessel radial calibration of the LOS. The position of the focal points and the optical heads are measured using the 3D measurement technology provided by FARO [110]. The accuracy of the LOS measurements is of the order ≤ 1 mm. From these measurements the 3D geometry of the LOS through the plasma is calculated and used for determining the intersection with the neutral beam or gas puff. Thus, the intersection points of the LOS with the neutral beam and gas puff, respectively, are known with quite high accuracy.

Radiance calibration

A radiance calibration of the whole diagnostic setup is needed to calculate absolute values for the impurity density. Therefore, the in-vessel optical heads and the spectrometers are calibrated. For the calibration a standardized light source with a known spectral radiance (Labsphere, Model Unisource 1200) is used in a two-step approach. First, the integrating sphere is put in front of the optical head such that the viewing cone of the optics is completely filled by the aperture of the sphere. The light emitted by the sphere is then measured at different wavelengths. This results in a radiance calibration as a function of the wavelength for all fibers of the various optical heads.

For a complete radiance calibration the channels of the spectrometers, which are connected to

the fibers of the in-vessel optical head by a connection board, also need to be calibrated. This relative calibration facilitates the interchange of the channels. Each channel is illuminated directly with the integrating sphere thus, enabling a comparison of the detected photons of each channel.

For the calibration a wavelength scan from 370 to 730 nm is performed. While the grating is turning, the CCD chip is illuminated by emission at different wavelengths. The center of the chip is irradiated by the whole wavelength range. Hence, the sensitivity of the CCD chip is obtained. The resulting count rates of each pixel of the CCD chip yields information on the relative efficiency of imaging and detecting the light of a specific wavelength. The efficiency is given by the sensitivity S of the spectroscopical setup which is a function of the wavelength λ , the pixel position in x and y direction of the CCD chip and the spectrometer channel. The dependence is simplified to $S = S(\lambda, x_{\text{pix}}, \text{fibre})$ by separately calibrating each channel of the spectrometers which are binned in the y direction of the camera (see figure 4.9(b)). The sensitivity is the link between the measured signal and the radiance of the integrating sphere

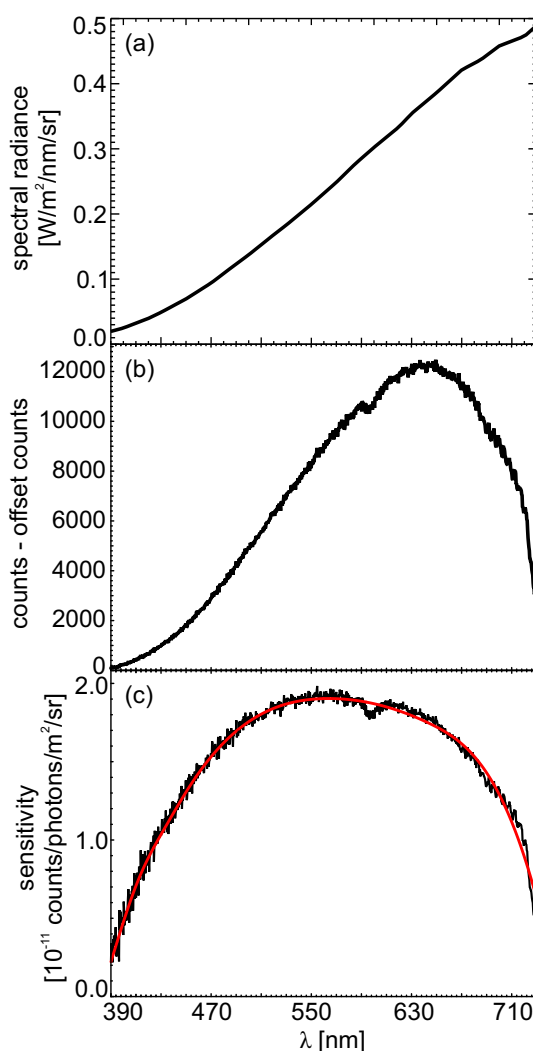


Figure 4.7: (a) Spectral radiance of the integrating sphere, (b) signal measured for one channel and (c) resulting sensitivity curve.

and is used to calibrate the measured spectra of the diagnostics:

$$S = \frac{n_{\text{counts}}}{Lt_{\text{exp}}} = \frac{n_{\text{counts}}}{L_{\lambda} \Delta\lambda_{\text{pix}} t_{\text{exp}}}. \quad (4.1)$$

Here $n_{\text{counts}}/t_{\text{exp}}$ is the counting rate per pixel, L the spectral radiance, L_{λ} the spectral radiance at a certain wavelength and $\Delta\lambda_{\text{pix}}$ the wavelength range detected by a pixel. The sensitivity of the spectroscopical setup is mainly determined by the number of counts per photon, by the acceptance angle of the spectrometer, by the etendue, which is a measure of how much light can be coupled into the spectrometer, and by losses due to transmission, reflection, slit edges and vignetting. Figure 4.7(a) shows the spectral radiance of the integrating sphere, (b) the measured Ulbricht sphere signal and (c) the resulting sensitivity curve of the corresponding channel with a spline fit to the data in red. The dip at ~ 600 nm is owing to the absorption by water molecules within the fibers.

Instrument function

The width of the entrance slit and optical imperfections determine the spectral width of the instrument function. A detailed knowledge of the instrument function of the spectrometers is needed to deconvolve the true CXRS spectra from the effects due to the optics of the system. The instrument functions of each spectrometer channel have been measured with calibration lamps (Hg and Ne lamps) at different wavelengths throughout the visible range and at different slit widths. The edge CXRS diagnostics typically employ a slit width of $50 \mu\text{m}$. For slit widths $\leq 50 \mu\text{m}$ the shape of the instrument functions are well described by a Gaussian function. The deconvolution is performed analytically during the fitting process and the measured width of the spectrum has contributions from the instrumental width and the Doppler width. For a slit width of $50 \mu\text{m}$ the full width at half maximum (FWHM) of the instrument function for the different spectrometer channels is in the range of 0.031 to 0.036 nm for the toroidal LFS and both HFS systems and between 0.023 to 0.027 nm for the poloidal LFS system (at a central wavelength of 494.5 nm). Slight variations of the different spectrometer channels arise due to imperfections of the entrance slit.

Figure 4.8 shows an example instrumental fit in red at a slit width of $50 \mu\text{m}$. The curve in black corresponds to the measured spectral line. To obtain a sub-pixel resolution, the grating is slowly moved for a small wavelength interval (such that the spectral line falls within the

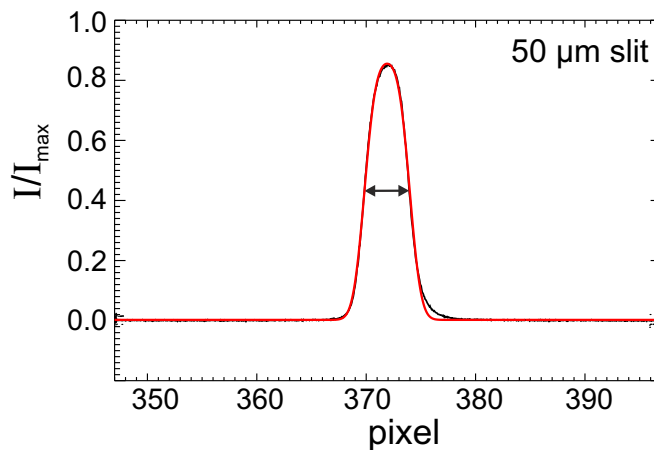


Figure 4.8: Instrument function for a slit width of $50 \mu\text{m}$.

spectral range of the spectrometer) while a large number of frames is recorded. The movement of the spectral line is slow compared to the repetition time. The measured spectra are then used to obtain a highly-resolved spectral line measurement by calculating the center of mass for the spectral line and shifting the spectrum such that the center of mass coincides with the one of the first frame. The asymmetric appearance on the right-hand side of the spectral line is attributed to the spectral line source. The arc lamps used have several lines with long spectral wings on the red side of the spectrum.

Wavelength calibration

For the measurement of the small rotation velocity of the impurity ions at the plasma edge a very accurate knowledge of the wavelength calibration is needed, since systematical uncertainties in the rotation would arise from any error in the wavelength calibration. Special care was taken to minimize the uncertainties of the wavelength axis.

The light collected by each optical head is transmitted by 400 μm optical fibers and guided into a spectrometer. The optical fibers are stacked vertically in front of the entrance slit of the spectrometer. The light is collimated, then dispersed by a 2400 lines/mm grating and focused onto the CCD camera. The grating equation of the spectrometer is given by:

$$ng\lambda = \cos\epsilon(\sin\alpha + \sin\beta) \quad (4.2)$$

where n is the diffraction order, g the number of grooves/mm of the grating, λ the wavelength, ϵ the vertical angle of an off-axis ray (see figure 4.9(a)) and α and β the angle of incidence and diffraction on the grating, respectively. In the image plane of the spectrometer a spectral line has a strong curvature since the wavelength λ depends on $\cos\epsilon$. A vertical entrance slit has off-axis point sources and therefore, the diffraction angle β depends on the vertical angle ϵ . This causes the image of a spectral line to be roughly parabolic [111]. Figure 4.9(b) shows the parabolic image at a wavelength of 650.7 nm measured using a Ne calibration lamp. For a particular central wavelength λ_0 the angle of incidence α is fixed. If ϵ and β are small, λ_0 is

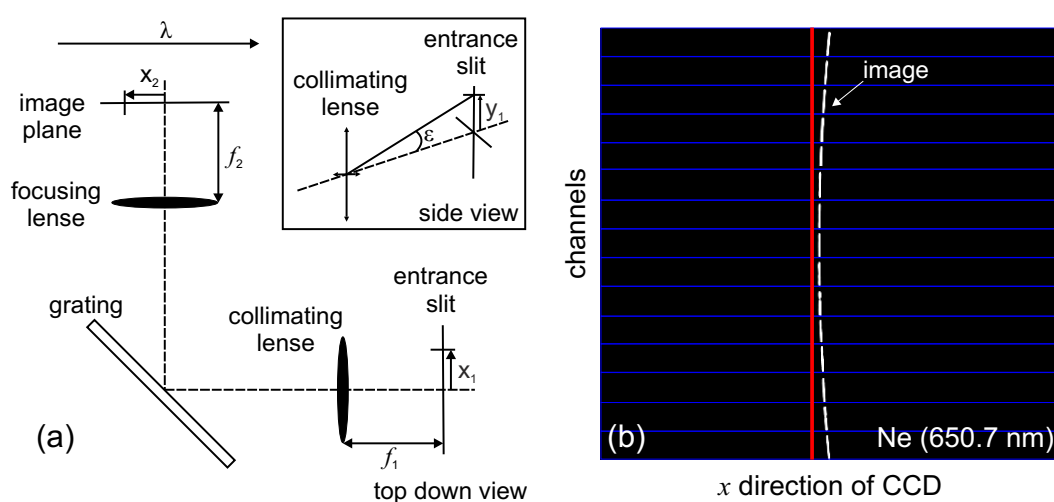


Figure 4.9: (a) Schematic of a grating spectrometer (adapted from [112]), (b) image of the spectrometer channels at a wavelength of $\lambda = 650.7$ nm (Ne lamp).

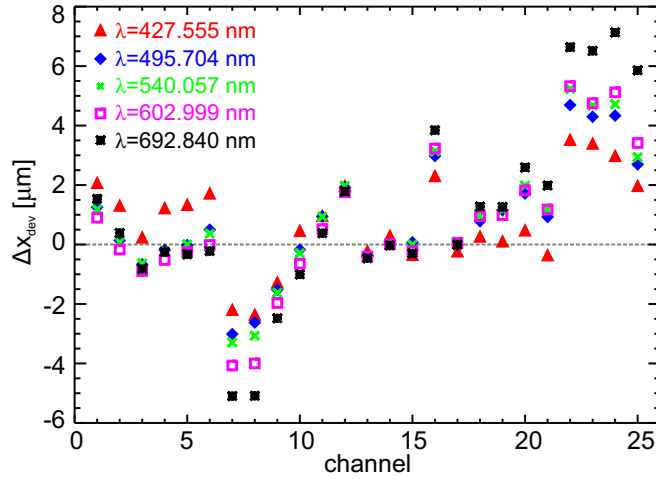


Figure 4.10: Measured deviations from the parabolic image of a straight entrance slit.

given by $\lambda_0 \approx \frac{1}{ng}(\sin \alpha + \beta)$. Expanding λ in equation (4.2) about ϵ and β leads to:

$$\lambda - \lambda_0 = \Delta\lambda \approx -\frac{\epsilon^2}{2}\lambda_0 + \frac{d\lambda}{d\beta}\Delta\beta \quad (4.3)$$

where $\Delta\beta = \beta$. The y -coordinate on the CCD chip (in the vertical direction) of the image of a point source with a vertical angle ϵ is given by $y = f_2 \tan \epsilon$ where f_2 is the focal length of the focusing lens. The vertical deviation from the on-axis image is determined by expanding y about ϵ (ϵ being small) leading to $\Delta y = y - y(\epsilon \approx 0) \approx f_2 \epsilon$. The x -coordinate on the CCD chip (horizontal direction) of the on-axis image of a point source is given by $x = f_2 \tan(\beta - \beta_c)$ where β_c is the angle of diffraction of the central wavelength. The horizontal deviation from the image is obtained by expanding x about β resulting in $\Delta x = f_2 \sec^2(\beta - \beta_c) \Delta\beta$. Thus, equation (4.3) results in:

$$\Delta\lambda \approx -\frac{\Delta y^2}{2f_2^2}\lambda_0 + \frac{\cos\beta}{ng} \frac{1}{\sec^2(\beta - \beta_c)} \frac{\Delta x}{f_2}. \quad (4.4)$$

For a single wavelength, $\lambda = \lambda_0$ and thus $\Delta\lambda = 0$, the parabolic image of a straight slit is described by:

$$\Delta x \approx \frac{ng\lambda_0}{2f_2} \frac{\sec^2(\beta_0 - \beta_c)}{\cos(\beta_0)} (\Delta y)^2. \quad (4.5)$$

However, small displacements of the input fibers from a perfectly vertical arrangement lead to small deviations from this formula, i.e. $\Delta x = \Delta x_p + \Delta x_{\text{dev}}$ where Δx_p describes the parabolic image (equation (4.5)) and Δx_{dev} the deviations. The deviation from the parabolic image of the straight entrance slit of each spectrometer channel has been determined at several different wavelengths using Hg and Ne calibration lamps. Figure 4.10 shows the deviations of the measured pixel position with respect to the theoretical pixel position, Δx_{dev} , for each channel of the spectrometer dedicated to the toroidal edge CX measurements and at different wavelengths. The effect increases linearly with the wavelength as the dispersion of the spectrometer is larger for increasing wavelengths. The deviations are mainly due to a deviation of the slit orientation of ~ 0.03 degrees from the vertical direction and imperfections of the slit edges, which are of the order 1–2 μm . The deviation is similar for the spectrometers which employ the poloidal LFS and the HFS LOS, respectively. Note that in the analysis of the CX measurements these

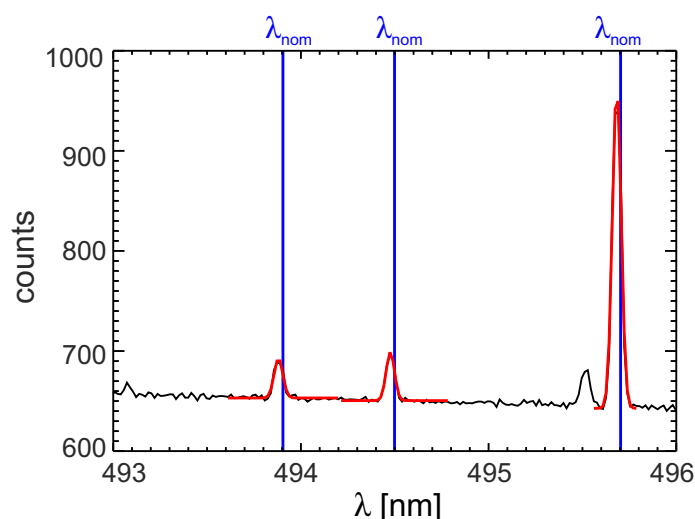


Figure 4.11: Example neon spectrum acquired during a discharge, the poloidal edge CXRS diagnostic was set to the B^{5+} wavelength.

corrections are taken into account.

For the B^{5+} line, the wavelength shift associated with a rotation velocity of 1 km/s is 1.65 pm. On this scale a systematic change in the Doppler shift may even arise from changes in the air pressure and temperature [113]. Therefore, an additional wavelength calibration is performed on a shot-to-shot basis. Two channels of the spectrometer dedicated to poloidal CX measurements (one channel for the spectrometer of the toroidal edge system) are switched to a neon lamp which allows a neon spectrum to be measured in every discharge. One channel is attached to the upper half of the camera and the second channel to the lower half. This also provides a check on the stability of the parabola of the spectrometer as a function of time (e.g. the parabola might change due to the mechanical movement of the spectrometer). In addition, the parabola measurements are retaken after every experimental campaign to track systematic variations and possible changes of the spectrometers.

From the neon spectra, the apparent systematic shift is calculated and the ‘true’ poloidal rotation velocity is evaluated. This method allows the determination of the wavelength calibration quite accurately with uncertainties smaller than 1 km/s. Figure 4.11 shows an example spectrum of the neon lamp acquired during a discharge. The sum of 200 spectra collected at the end of the discharge is used for the calibration. In the vicinity of the B^{5+} wavelength three well-known neon lines are fitted. The lines, marked in blue in figure 4.11, represent the nominal value of the neon lines at 493.904, 494.499 and 495.703 nm [106]. The spectral lines are each fitted using one Gaussian. The average of the difference between the central wavelength and the theoretical wavelength of the three neon lines is then used to calculate the apparent systematic shift. In this discharge, the shift of the neon lines is 0.023, 0.022 and 0.021 nm corresponding to velocities of 13.9, 13.3 and 12.7 km/s, respectively. Note that this shift is mainly given by the mechanical uncertainties of the sine drive, which controls the position of the grating.

A similar wavelength calibration method is used for the HFS CXRS systems. Since the HFS diagnostics are not equipped with a dedicated spectrometer, the wavelength calibration is performed after each discharge in which the HFS systems are used.

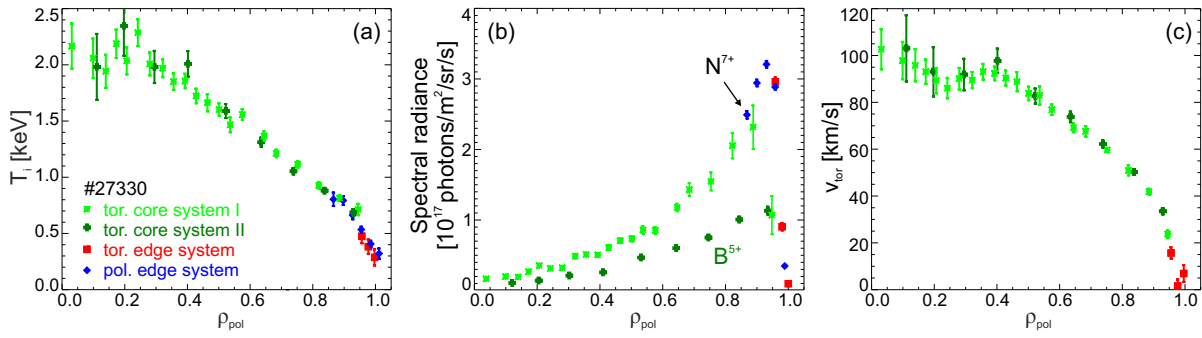


Figure 4.12: Consistency check of LFS CXRS measurements: (a) ion temperature, (b) spectral radiance and (c) toroidal rotation velocity. The profiles obtained from the core systems are shown in green, data from the toroidal edge system are shown in red and measurements obtained with the poloidal edge system in blue.

4.4 Validation of CXRS measurements

At the LFS the edge CXRS measurements may be combined with those measured in the core to obtain full radial profiles, i.e. from the magnetic axis out to the separatrix. A comparison of all the CXRS measurements also provides a consistency check of the diagnostics. At AUG two core systems are installed, one views beam source #3 in sector 15 and the other utilizes beam source #8 in sector 7 (see figure 4.1). For experiments in which the NBI source #8 is not utilized the spectrometer of the core system II is equipped with extra LOS from the optical head of the toroidal core CXRS system I. This enables the measurement of two different impurity species on the same beam and a cross-check on radiance and wavelength calibrations when imaging the same impurity.

Figure 4.12 shows example profiles of ion temperature, spectral radiance and toroidal rotation velocity. In this discharge the edge systems and the core system I measured on N^{7+} ($n = 9 \rightarrow 8$, $\lambda = 566.937$ nm). The spectrometer of the core CXRS system II utilized LOS from the core CXRS system I (i.e. viewing NBI source #3) and measured the B^{5+} spectral line. Good agreement is obtained for the spectral radiance, temperature and toroidal rotation velocities and the profiles are consistent within their uncertainties, giving confidence that the calibrations of the various diagnostics are very accurate.

A validation of the diagnostic technique can also be performed by comparing the radial electric field profile derived from CXRS measurements on multiple impurity species (see chapter 5).

4.5 Corrections to CXRS measurements

Atomic physics effects may affect the spectra and can cause small errors in the temperature and rotation measurements if they are not properly taken into account. These include the CX cross-section effect and the gyro-motion effect, which are presented in subsection 4.5.1. Corrections due to the Zeeman effect are discussed in subsection 4.5.2.

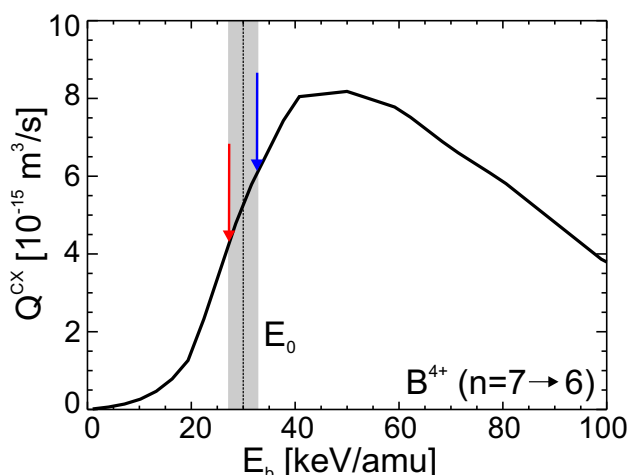


Figure 4.13: Energy dependent CX cross-sectional area for the $B^{5+} + D^0 \rightarrow B^{4+} + D^+$ reaction; E_0 indicates the first beam energy component for a 60 keV D beam, such as the one used for the edge CXRS measurements.

4.5.1 Charge exchange cross-section effect

Due to the energy-dependent CX cross-sections several atomic physics effects arise when measuring CX emission. The main effect is that an apparent wavelength shift, which is not associated with the Doppler motion of the parent ion distribution, can be observed in the measured spectra [109]. This effect depends on the direction of observation and on the geometry of the LOS with respect to the neutral beam. If the observation direction is perfectly perpendicular to the neutral beam, then along the magnetic field (parallel/toroidal observation) this effect would vanish while perpendicular to the magnetic field (poloidal observation) a net effect would arise due to the gyro-motion of the particle (discussed below). Small deviations from a perfectly perpendicular setup with respect to the neutral beam (i.e. small angles in the LOS geometry and/or tilt angles in the beam geometry), which is typically the situation in the experiment, in combination with the energy dependent CX cross-section lead to this effect.

The emission ε_{CX} from the CX process is proportional to $n_b n_\alpha Q$, where n_b is the neutral beam density, n_α the impurity density and Q the effective emission rate. The effective emission rate can be written as $Q(v_{rel}) = \sigma_{eff}^{CX}(v_{rel})v_{rel}$, where σ_{eff}^{CX} is the CX cross-section of a given transition, $v_{rel} = |\mathbf{v}_\alpha - \mathbf{v}_b|$ is the relative velocity between the impurity ion with velocity \mathbf{v}_α and the neutral beam particle with velocity \mathbf{v}_b . The effective emission rate for the $B^{5+} + D^0 \rightarrow B^{4+} + D^+$ reaction is shown in figure 4.13. The first beam energy component E_0 of beam source #3 (60 keV D beam and thus, $E_0 = 30$ keV/amu), which is used as diagnostic beam for the edge CXRS diagnostics, is indicated with a vertical line.

Ions moving towards/away from the beam (and hence, with slightly higher/lower collision velocity) sample different regions of the energy-dependent CX cross-sections (marked with blue and red arrows in figure 4.13) and thus, have a higher/lower probability to undergo CX. In the case of a non-perfect perpendicular view of the neutral beam, this might lead to an enhancement of the observed line intensity on one side of the spectrum, while the other side is reduced. Hence, the spectra are distorted and result in an apparent line broadening and shift not associated with the true ion temperature and velocity.

The cross-section effects on the measured CX spectra have been simulated for the geometry of the edge systems and for a 60 keV deuterium beam (first, second and third beam energy

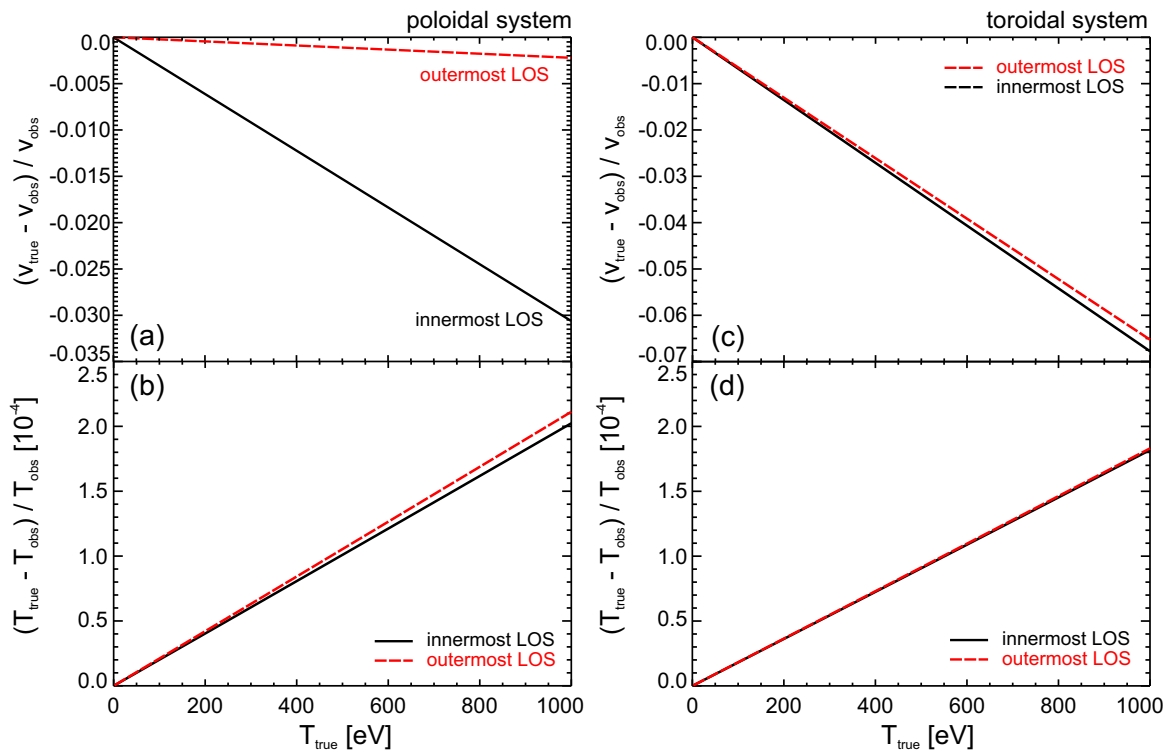


Figure 4.14: Cross-section effects on measured B^{5+} CX spectra for a 60 keV D beam: (a) difference of true and observed velocities, $v_{true} - v_{obs}$, normalized to v_{obs} , (b) difference of true and observed temperature, $T_{true} - T_{obs}$, with respect to T_{obs} for the poloidal diagnostic, (c) velocity and (d) temperature corrections for the toroidal system.

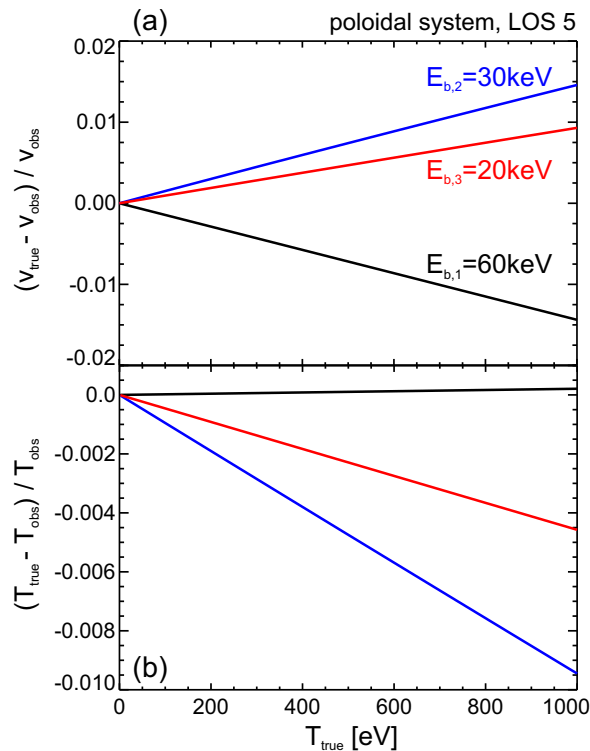


Figure 4.15: Cross-section effects in B^{5+} CX spectra for the first, second and third energy component of a 60 keV D beam: (a) velocity and (b) temperature corrections for the poloidal system.

components) using the approach of von Hellermann *et al.* [109]. At AUG, the neutral beam #3 has a vertical tilt of 4.9 degrees and a toroidal tilt of 19.1 degrees.

In the vicinity of the beam the effective emission rate Q can be represented by $Q = Q_0 \exp(\alpha \Delta v + \beta \Delta v^2)$ where α is proportional to the first derivative of Q and β to its second derivative [109]. The apparent line shift is due to the gradient of Q , while the apparent line broadening arises due to the curvature of Q . The LOS of the edge CXRS systems have a nearly perpendicular view and are aligned in a poloidal (see figure 4.3) and toroidal (see figure 4.1) plane, respectively. Figure 4.14(a) and (b) show the corrections to the observed temperatures, T_{obs} , and velocities, v_{obs} , with respect to the true temperature, T_{true} , and velocity, v_{true} , for B^{5+} for the inner- and the outermost LOS of the poloidal optical head. Figure 4.14(c) and (d) show the corrections for the toroidal edge system. The corrections are well within the error bars of the measurements. For an edge rotation of 20 km/s the correction due to the energy-dependent CX cross-section is less than 1.5 km/s for the toroidal system and less than 0.7 km/s for the poloidal system. In the considered temperature range at the plasma edge (200–500 eV) the temperature corrections are between 0.01 to 0.05 eV.

Figure 4.15 shows the corrections for the first, second and third beam energy components of a 60 keV D beam. Both the velocity and temperature corrections of the second and third beam energy components change sign, while the temperature corrections are an order of magnitude higher compared to the correction of the first beam energy component. Note, however, that the first beam energy component contributes about 90 % to the total CX emission, while the contributions of the second and third component are of the order 8 % and 2 %, respectively (taking into account the effective CX emission rate and the beam energy population densities, $E_0 : E_0/2 : E_0/3 = 65 \% : 25 \% : 10 \%$).

The results obtained from these calculations demonstrate that for the observed temperature and velocity ranges the cross-section effects on the measured spectra are negligible and hence, they are not included in the standard analysis.

Gyro-motion effect

In addition to the CX cross-section effect described above, the effect of the gyro-motion of the impurity ion along with the finite lifetime of the observed state [112] can become important when measuring in the plane of the gyro-orbit. An apparent vertical velocity arises as the ion rotates $\omega\tau$ before emitting a photon, with ω the ion gyro-frequency and τ the lifetime of the excited state of the transition. If the neutral beam has a velocity component in the plane of the gyro-motion, the ions moving towards the beam have a larger collision velocity and are more likely to undergo CX due to the cross-section effect explained above. This leads to a net apparent line shift toward the beam if the LOS have a component parallel to the neutral beam (i.e. the viewing geometry is not perfectly perpendicular to the neutral beam). Since τ of the considered transition is finite the impurity ions gyrate $\omega\tau$ before emitting the CX photon. Hence, after an angular precession of $\omega\tau$ part of the velocity associated with the apparent line shift is directed downward, perpendicular to the neutral beam, i.e. into the poloidal direction (see figure 4.16). The apparent velocity due to the combined gyro-motion and CX cross-section effect is given by [114]:

$$\mathbf{v}_{app}^{local}(\mathbf{v}_{AZ-1}) = \frac{1}{1 + \omega^2\tau^2} \left[\mathbf{v}_{AZ-1} + \frac{\omega\tau}{B}(\mathbf{v}_{AZ-1} \times \mathbf{B}) + \frac{\omega^2\tau^2}{B^2}(\mathbf{v}_{AZ-1} \cdot \mathbf{B})\mathbf{B} \right]. \quad (4.6)$$

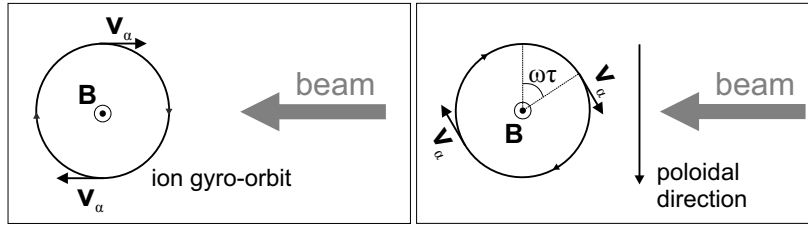


Figure 4.16: The precession of the ion along its gyro-orbit during the lifetime τ of the excited state leads to a net (apparent) velocity pointing downward, i.e. into the poloidal direction.

Here, $v_{A^{Z-1}}$ is the apparent velocity of the product ion $A^{(Z-1)}$ after the CX process. This equation is derived for a local measurement, however, CXRS measurements are integrals along the LOS. The local equation (4.6) is integrated along the LOS to give the correction arising from the gyro-motion and CX cross-section effect [115] and depends on the gyro-frequency, the lifetime of the excited state and the angles between the LOS and the neutral beam.

An estimate for the effect of the gyro-orbit motion during the finite lifetime of the excited state has been calculated for the simplest case assuming that the optical head has a perpendicular view on the neutral beam (i.e. the CX cross-section effect is zero). For a typical magnetic field of 2 T at the low-field side of AUG, the gyro-frequency of B^{4+} is of the order 7×10^7 Hz. A scan of various lifetimes τ has been performed and the apparent velocity due to the gyro-motion effect as a function of τ and $\omega\tau$ is shown in figure 4.17. For $\tau = 0$, i.e. the photon of the excited state is emitted immediately after the CX process, the apparent velocity is zero. For a certain value of τ (cf. figure 4.17) the apparent velocity reaches a maximum (in the case of B^{4+} , $T = 500$ eV and an observed velocity of $v_{obs} = 20$ km/s, τ is approximately 7 ns and the correction is of the order 25 % corresponding to a maximal apparent velocity of 4.8 km/s). For large values of τ the apparent velocity vanishes since the ion gyrates ‘infinitely’ fast and eventually emits the photon.

This analysis has been extended to account for the ‘real’ geometry of the new poloidal edge CXRS system. The typical lifetime for the B^{4+} ($n = 7 \rightarrow 6$) transition is on the timescale

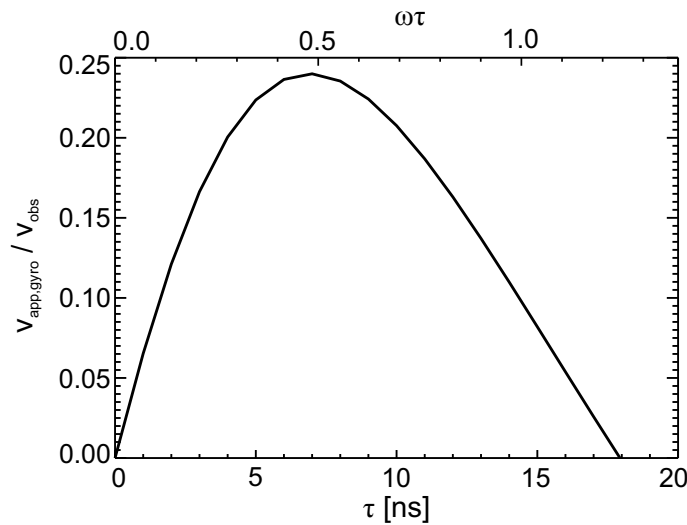


Figure 4.17: Gyro-motion effect for a perpendicular view on the neutral beam: Apparent velocity, $v_{app,gyro}$, normalized to an observed velocity of $v_{obs} = 20$ km/s for B^{5+} as a function of the lifetime of the excited state for $\omega = 7 \times 10^7$ Hz and $T = 500$ eV.

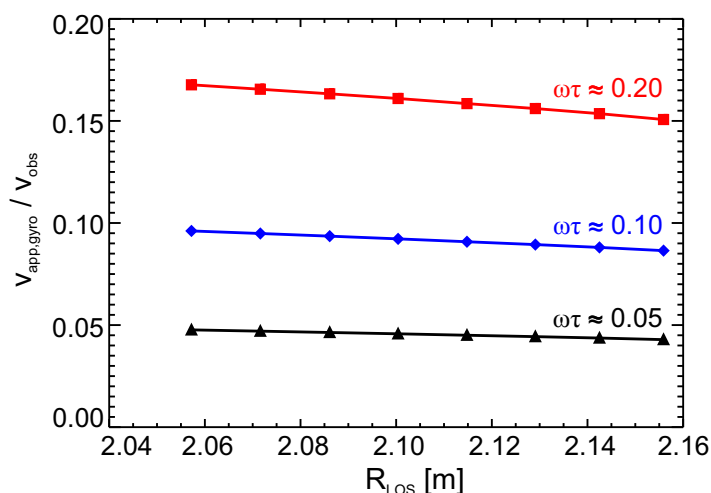


Figure 4.18: Apparent velocity, $v_{app,gyro}$, normalized to an observed velocity of $v_{obs} = 20$ km/s for the B^{5+} spectral line as a function of the major radius of the LOS, R_{LOS} , of the poloidal system arising due to the gyro-motion effect for different values of $\omega\tau$ and $T = 500$ eV.

of ns, similar to the lifetime of C^{5+} ($n = 8 \rightarrow 7$). The Einstein coefficients for B^{4+} and C^{5+} have been calculated using the Cowan code [116] (as provided by the Atomic Data Analysis Structure ADAS [117]), which are in agreement with those derived from Wiese *et al.* [118] (the deviations are smaller than $0.04 \cdot 10^8 s^{-1}$). Calculating the vacuum radiative lifetime of both B^{4+} and C^{5+} yields similar values, i.e. 0.638 ns for B^{4+} and 0.552 ns for C^{5+} , in good agreement with the vacuum radiative lifetime used in ref. [112] (0.54 ns for the C^{5+} transition). Using a collisional-radiative model and allowing radiative decay from higher n levels [112] an effective lifetime for C^{5+} was estimated as 0.7 ns. Measurements on TFTR revealed an effective lifetime of 1.1 ns for the C^{5+} transition [112], while on DIII-D the experimentally derived lifetime was 1.7 ns [114]. For parameters at AUG and considering the B^{4+} transition these lifetimes translate to $\omega\tau \approx 0.05$, $\omega\tau \approx 0.08$ and $\omega\tau \approx 0.12$, respectively. A sensitivity study of increasing lifetimes has been performed and the results are shown in figure 4.18. The apparent velocity, defined as the difference between the true and the observed velocity, due to the gyro-motion of the impurity ion increases for longer lifetimes of the excited state.

The combined effect due to both the gyro-orbit motion and the CX cross-sections is shown in figure 4.19. Figure 4.19(a) shows the velocity corrections for B^{5+} as a function of the major radius of the LOS, R_{LOS} , while figure 4.19(b) shows the dependence on the true ion temperature. For increasing values of $\omega\tau$ the apparent velocity appears to be higher for lower ion temperatures due to competing corrections arising from the CX cross-section and gyro-motion effect. For $\omega\tau = 0$ the remaining effect is due to the energy-dependent CX cross-sections as discussed above (see figure 4.14).

The three beam energy components have also been considered and the resulting velocity corrections for B^{5+} are shown in figure 4.20(a). The corrections are about 40% higher for the second and third beam energy component compared to the first beam energy component. However, as mentioned earlier the main contribution to the total CX emission is given by the first beam energy component. Figure 4.20(b) shows the corrections of the combined CX cross-section and gyro-motion effect for different impurity species calculated for the first beam energy component. The effect scales with the charge state of the considered species. For lower charge states (e.g. He^{2+}) the correction even changes sign due to the counterbalance between

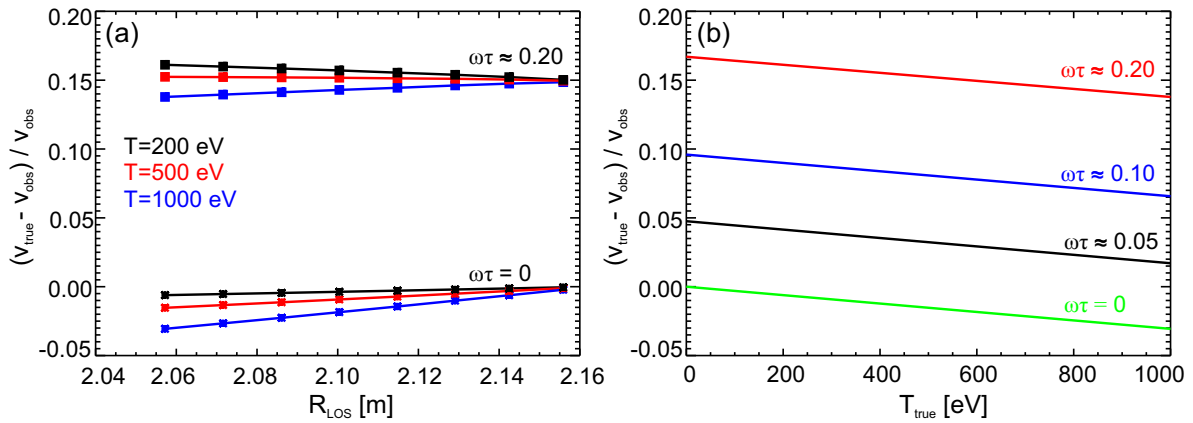


Figure 4.19: Combined CX cross-section and gyro-motion effect for the poloidal system: (a) corrections for B^{5+} spectral line as a function of the major radius of the LOS, R_{LOS} , for two different values of $\omega\tau$ and for different ion temperatures, (b) corrections as a function of the true ion temperature, T_{true} . The curves are normalized to an observed velocity of $v_{obs} = 20$ km/s. For the case $\omega\tau = 0$ (i.e. no gyro-motion effect) the impact of the energy dependence of the CX cross-sections is shown separately (as in figure 4.14).

the CX cross-section and gyro-motion effect.

The combined CX cross-section and gyro-motion effect has been simulated for real impurity ion temperature and poloidal rotation profiles measured at AUG. For this case only the first beam energy component has been considered. The effect of varying the lifetime of the B^{4+} transition is shown in figure 4.21(a), while figure 4.21(b) and (c) show the input temperature and velocity profile. The theoretically and experimentally derived lifetimes [112, 114] discussed above have been used for the simulations. Note that for smaller R_{LOS} the corrections appear to be large, however, for the small observed rotation velocities (see figure 4.21(c)) these values translate to ~ 0.5 km/s.

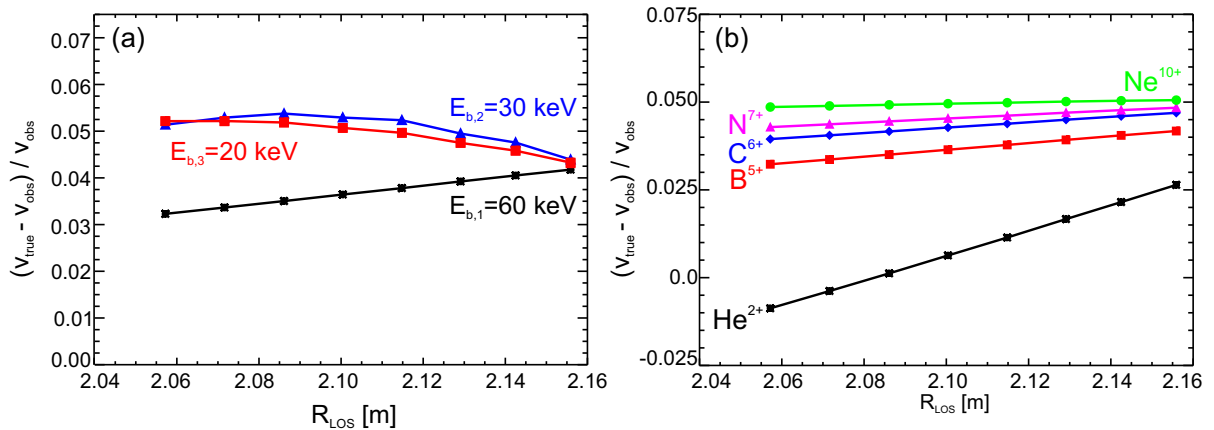


Figure 4.20: (a) Combined CX cross-section and gyro-motion effect for the poloidal system evaluated for the three beam energy components of a 60 keV D beam: corrections for B^{5+} spectral line for an observed velocity of $v_{obs} = 20$ km/s, $\tau = 0.7$ ns, $\omega\tau \approx 0.05$ and $T = 500$ eV. (b) Corrections of the combined effect for different impurity species; here the corrections are shown for the first beam energy component.

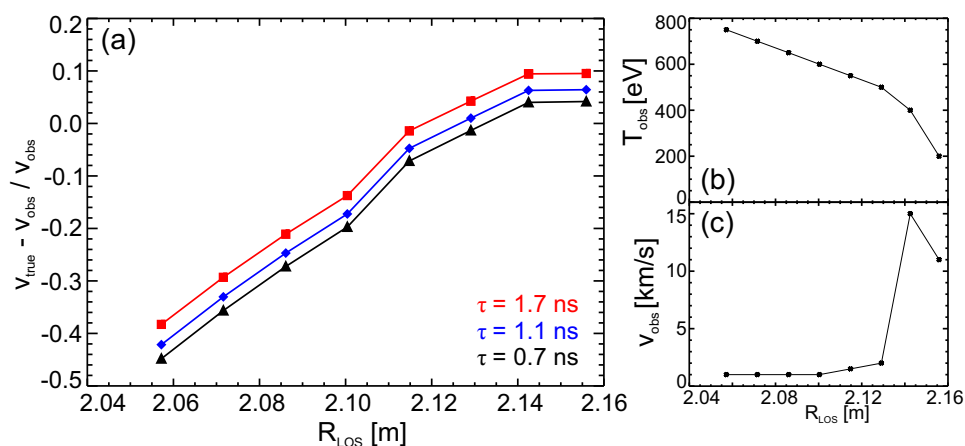


Figure 4.21: Calculations for a real AUG case using measured impurity ion temperature and poloidal rotation profiles: (a) corrections for B^{5+} as a function of the major radius of the LOS, R_{LOS} , of the poloidal system for different values of the lifetime τ , (b) input temperature profile T_{obs} , (c) input rotation velocity profile v_{obs} .

The calculations presented in this subsection show that for the temperature and rotation ranges observed at the plasma edge the corrections due to the CX cross-section and gyro-motion effects on the measured spectra are small. The magnitude of the correction depends on the value of $\omega\tau$, which itself is uncertain within a factor of 2. Therefore, the corrections are not included in the standard analysis. Due to the atomic physics effects an additional uncertainty of ± 0.5 km/s arises for the poloidal rotation measurements, yielding a total uncertainty of 1.5 km/s.

4.5.2 Correction due to Zeeman splitting

Due to the presence of a magnetic field in tokamak plasmas the Zeeman effect needs to be taken into account. Each Zeeman component (π -, $\pm\sigma$ -components) is a Gaussian itself with a Doppler width which represents the true ion temperature. When all of the components are added up a line-shape which is nearly Gaussian is produced. However, the width of this Gaussian overestimates the ion temperature [5, 119]. Several methods are employed to account for the Zeeman splitting in CX spectra. Note that the total Zeeman pattern includes both the Zeeman and the fine structure contributions, i.e. the fine structure is also taken into account in the fitting process.

At AUG, correction factors calculated as a function of the apparent ion temperature [120] are used to account for the Zeeman broadening, assuming that the total line shape of the measured spectra is Gaussian. This assumption is valid at high temperatures and low magnetic fields, where the Doppler broadening is dominant compared to the Zeeman splitting. The Zeeman components are calculated assuming fully mixed populations of the l -states (l being the orbital angular momentum quantum number). The validity of this assumption has been examined for the plasma edge conditions of AUG using an empirical formula [121] for determining the critical plasma density at which a given transition is fully mixed:

$$n_e \geq \frac{1}{8.5 \times 10^{-16}} \sqrt{\frac{Z^{15}}{n^{17}}}. \quad (4.7)$$

Here, n_e is the electron density in cm^{-3} , Z the charge of the particle and n the principal quan-

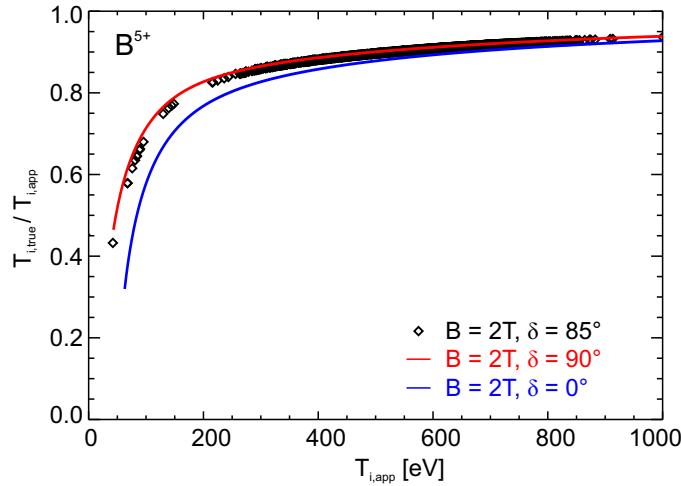


Figure 4.22: Correction factor $T_{i,true}/T_{i,app}$ for B^{5+} to account for Zeeman splitting in CX spectra.

tum number. For the B^{5+} transition, a critical density of $1.3 \times 10^{19} \text{ m}^{-3}$ is obtained which is lower than typical densities at the plasma edge of AUG indicating that the l -levels are fully mixed. Each component of the Zeeman pattern is convolved with a Gaussian which corresponds to the Doppler broadening at the real ion temperature. The resulting feature is well described by a single Gaussian with an apparent ion temperature $T_{i,app}$.

Figure 4.22 shows the dependence of the correction factor for B^{5+} on the apparent ion temperature calculated for the LOS of the poloidal optical head (almost perpendicular view to the magnetic field) and a magnetic field of 2 T. The solid lines in blue and red show the theoretical curves calculated for $B = 2 \text{ T}$ and an angle δ of 0° and 90° , respectively, where δ is the angle between the LOS and the magnetic field. The black diamonds mark the curve which is used for the evaluation of the experimental data. The correction factors vary for different angles δ due to the σ - and π -transitions. The σ -components are dominant for observation angles parallel to the magnetic field, while the π -component dominates in the case of observation angles perpendicular to the magnetic field. The true ion temperature $T_{i,true}$ is obtained by multiplying the measured apparent temperature with the correction factor. This procedure is performed for all of the CXRS diagnostics.

In summary, in the standard analysis of the CXRS measurements on AUG the corrections due to the CX cross-section and gyro-motion effects are not taken into account as they are found to be small, while the corrections due to the Zeeman effect are included.

Chapter 5

The structure of the edge radial electric field at ASDEX Upgrade

The most accepted explanation for the edge transport barrier (ETB) is the existence of a strong shear in plasma flow perpendicular to the magnetic field caused by a local radial electric field E_r . This $\mathbf{E} \times \mathbf{B}$ velocity shear is thought to be fundamental for edge turbulence suppression [4] thus, aiding the formation of the ETB and leading to the L-H transition. However, the origin and development of E_r is still not fully understood although the existence of E_r is ubiquitous to toroidal magnetic confinement devices such as ASDEX Upgrade [22, 24, 25], DIII-D [122], Alcator C-Mod [17], JET [16], JT-60U [18], TFTR [123], TEXTOR [124], MAST [125], NSTX [113], LHD [126], W7-AS [127], TJ-II [128] and RFX [129]. In order to get a better understanding of the $\mathbf{E} \times \mathbf{B}$ shear and its connection to the transition from L- to H-mode detailed measurements of E_r are highly desirable.

This chapter provides a general description of the evaluation of E_r using the new edge charge exchange recombination spectroscopy (CXRS) diagnostics and discusses the validation of the radial electric field measurements. The E_r profile measured at the inner midplane is compared to the beam-based measurements at the low-field side. The electrostatic potential is derived from these measurements, which enables the consistency of the flows and the electrostatic potential on a flux surface to be tested.

5.1 Derivation of the radial electric field at the plasma edge of ASDEX Upgrade

For an accurate evaluation of the radial electric field E_r via the radial force balance equation (see section 2.2.1), the poloidal and toroidal magnetic fields, B_θ and B_ϕ , as well as temperature, density and flow velocities of the observed species α are required:

$$E_r = \frac{1}{n_\alpha Z_\alpha e} \frac{\partial p_\alpha}{\partial r} - v_{\theta,\alpha} B_\phi + v_{\phi,\alpha} B_\theta. \quad (5.1)$$

Here, r is the radial coordinate, n_α the density, Z_α the charge state, e the elementary charge, $\frac{\partial p_\alpha}{\partial r}$ the radial pressure gradient, while $v_{\theta,\alpha}$ and $v_{\phi,\alpha}$ correspond to the poloidal and toroidal rotation velocities of the species. The toroidal and poloidal magnetic fields are determined from the equilibrium reconstruction of the plasma using CLISTE [130]. The edge CXRS diagnostics provide all of the remaining quantities needed to evaluate E_r . The ion temperature

is determined from the Doppler width, the rotation velocity from the Doppler shift and the impurity density from the spectral radiance of the observed CX line (as described in section 3.1.1). For the evaluation of the impurity density the contributions from the three beam energy components and charge transfer from excited deuterium in the $n = 2$ level is taken into account. As the CXRS measurements represent the original ion population, the charge state of the fully ionized impurity ion is used for the evaluation of the pressure gradient term in the radial force balance (first term on the right-hand side of equation (5.1)).

The following sign convention is used in this thesis: ϕ is counter-clockwise viewed from above, while θ points vertically downward at the outer midplane. Hence, counter-clockwise toroidal rotation is positive, while poloidal rotation velocities, which are vertically upward at the low-field side, are negative (in the electron diamagnetic drift direction). In the standard magnetic configuration of AUG B_ϕ is negative and B_θ is positive. The plasma current, I_p , and the neutral beam injection (NBI) are pointing into the positive toroidal direction. The profiles presented in the following are measured at the outer midplane, i.e. at the low-field side of AUG, if not stated otherwise.

Figure 5.1 shows example temperature, density and rotation profiles of B^{5+} ($n = 7 \rightarrow 6$, $\lambda = 494.467$ nm) obtained with the beam-based edge CXRS diagnostics in a type-I ELMy H-mode with B_ϕ on-axis of -2.5 T, I_p of 1 MA, 5 MW of neutral beam injection (NBI), 0.8 MW of electron cyclotron resonance heating (ECRH) and a central line-averaged density of $8 \times 10^{19} \text{ m}^{-3}$. The profiles are ELM-synchronized meaning that the data measured during the occurrence of an ELM crash are excluded. Only measurements up to 2 ms before the onset of an ELM (which corresponds to the time resolution of the edge CXRS diagnostics) are selected if not stated otherwise. To obtain full edge profiles a radial plasma sweep (see section 3.2) of 2 cm is performed during a time window of 800 ms.

Good agreement is obtained for the ion temperature and B^{5+} density profiles, which show a clear H-mode pedestal (cf. figure 5.1(a) and (b)). The toroidal rotation velocity is co-current and exhibits a minimum located around the pedestal top [100]. The poloidal rotation velocity is very low towards the plasma core, while inside the ETB a strongly sheared rotation in the electron diamagnetic drift direction is observed. Note that the measurements in the scrape-off layer (highlighted in grey in figure 5.1) are omitted as in this region the impurity density along with the active CXRS signal drops rapidly and additional background emission disturbs the active spectra making active CXRS measurements unreliable.

For the evaluation of E_r each individual CXRS profile is fit to a spline function. The resulting fits are then used for the determination of E_r . Note that usually the T_i and n_α profiles measured by the toroidal system are used in the fitting procedure since the toroidal diagnostic has a higher radial resolution (3 mm compared to 5 mm for the poloidal system), which enables the gradients in the profiles to be determined to higher accuracy. In the considered discharge (#26598) data for $\rho_{pol} < 0.94$ from the poloidal system have also been used for fitting T_i and n_α .

To reduce uncertainties due to the magnetic equilibrium the ion and electron profiles are aligned relative to each other (as described in section 3.3). The relative alignment of the CXRS systems is of minor importance for the positioning of E_r , as in the plasma edge the evaluation of E_r is dominated by the poloidal impurity rotation contribution (see figure 5.2). While the radial resolutions of the diagnostics are 3 and 5 mm, respectively, the relative profile alignment is possible to a higher accuracy (2–3 mm, indicated by a horizontal error bar in figure 5.1(a)) due to the steepness of the gradients, which are well resolved by the measurements.

Figure 5.2 shows the E_r profile in black deduced from the profiles of B^{5+} in figure 5.1. In

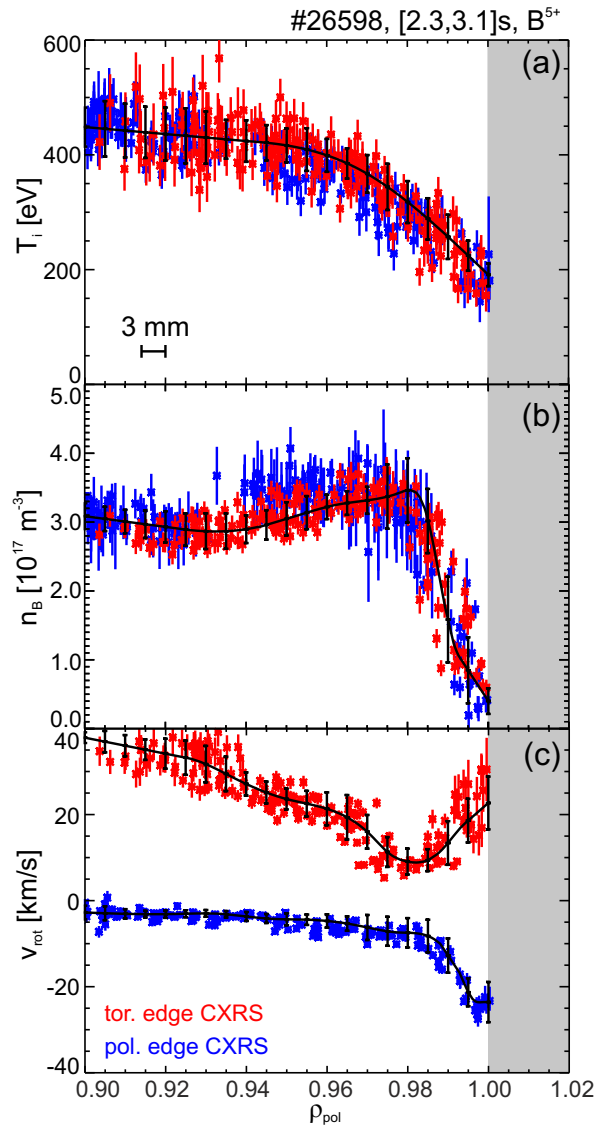


Figure 5.1: CX profiles obtained from measurements on B^{5+} in H-mode: (a) ion temperature, (b) B^{5+} density, (c) toroidal (red) and poloidal rotation velocity (blue). The fits to the data are highlighted in black.

the ETB a negative E_r well, a narrow, localized minimum close to the separatrix, is found. Towards the plasma core, the magnitude of E_r decreases and E_r changes sign (i.e. becomes positive, radially outward). The error bars shown in figure 5.2 are calculated via Gaussian error propagation using the standard deviation of the measured data in a small radial interval (± 0.005 in ρ_{pol} , which is of the order of the radial resolution of the diagnostics).

In figure 5.2 the individual terms in the radial force balance of B^{5+} are colour-coded: the pressure gradient term (green), the toroidal rotation term (red) and the poloidal rotation term (blue). In the radial force balance of impurity ions the poloidal rotation term is the main contribution for the evaluation of the E_r well. Towards the plasma core E_r is dominated by the toroidal rotation velocity.

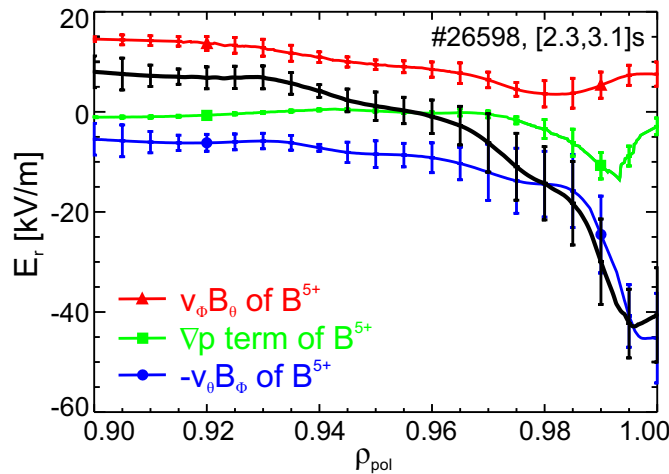


Figure 5.2: Radial electric field profile derived from CX measurements on B^{5+} : E_r in black, toroidal rotation term in red, pressure gradient term in green and poloidal rotation term in blue.

5.2 Validation of the radial electric field measurements

5.2.1 Comparison of different impurity species

Performing CX measurements on different impurity species allows the validation of the diagnostic technique and a consistency check of E_r to be obtained since E_r must be the same for all impurities [9]. Thus, all analyses must arrive at the same E_r profile regardless of the impurity species used. For this purpose the discharge described in section 5.1 was repeated to obtain CX measurements of He^{2+} ($n = 4 \rightarrow 3$, $\lambda = 468.571$ nm) and C^{6+} ($n = 8 \rightarrow 7$, $\lambda = 529.059$ nm). The resulting E_r profiles are shown in figure 5.3(a). Within the uncertainties, good agreement between the three different impurity species is obtained, not only in the minimum of the E_r well, but also in the profile shape towards the plasma core.

In a separate discharge a neon puff was included to cross-check the E_r profile with a fourth species. Due to the spectral range covered by the edge CXRS diagnostics (12.19 nm for the

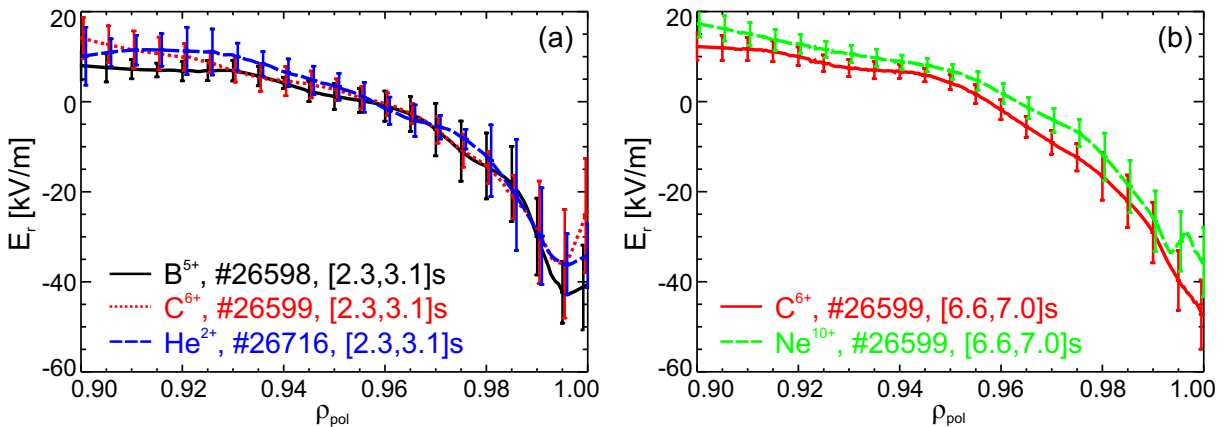


Figure 5.3: Radial electric field profile determined from CX measurements on different impurity species: (a) B^{5+} in black, C^{6+} in red (dotted line), He^{2+} in blue (dashed line), (b) C^{6+} in red and Ne^{10+} in green (dashed line) during the Ne-seeded phase.

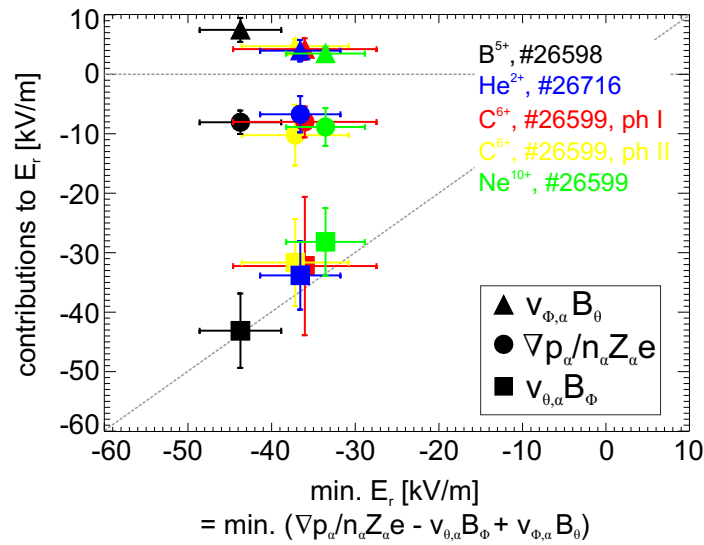


Figure 5.4: Individual impurity contributions for the evaluation of E_r versus minimum of E_r in H-mode: for the impurity ions the poloidal rotation term is the main player in the evaluation of E_r . The label ‘ C^{6+} , #26599, ph I’ corresponds to the non-seeded phase and ‘ C^{6+} , #26599, ph II’ to the Ne-seeded phase.

toroidal system and 7.84 nm for the poloidal system at a central wavelength of $\lambda = 527.5$ nm), simultaneous measurement of both C^{6+} and Ne^{10+} ($n = 11 \rightarrow 10$, $\lambda = 524.897$ nm) is possible. The resulting E_r profiles are shown in figure 5.3(b). The E_r profile is reproducible within the uncertainties regardless of the trace impurity used for the analysis. Note that in the Ne-seeded phase of the discharge, instead of low-frequently type-I ELMs smaller ELMs with a higher frequency appeared due to the neon puff. As the ELM-synchronization method was also used in this discharge less inter-ELM data remain. Therefore, the minimum of the E_r well is not fully resolved in this time period.

For all impurity species analyzed in H-mode plasmas, the poloidal rotation contribution is dominant in the radial force balance. In figure 5.4 the individual impurity contributions at the radial position of the E_r minimum are plotted against the minimum of the E_r well. Note that for the Ne-seeded phase the C^{6+} contributions correspond to the position of the minimum of E_r derived from the Ne^{10+} measurements, as no clear minimum is visible for C^{6+} . For all impurities, the toroidal rotation term and the pressure gradient term have almost the same value in absolute magnitude and cancel each other, while the poloidal impurity rotation term is the dominant contribution for the evaluation of the depth of the E_r well.

5.2.2 Comparison to Doppler reflectometry measurements

The E_r profile derived from the CXRS measurements has been compared to Doppler reflectometry (DR) measurements. As Doppler reflectometry relies on the backscattering of an electromagnetic wave at a corrugated cutoff layer (i.e. turbulent fluctuations are present at the cutoff surface, see also section 3.1.2), edge E_r measurements using DR in fully developed H-mode discharges are challenging due to the low level of density fluctuations at the plasma edge. The radial range of the DR measurements is determined by the frequency and the polarization (O- or X-mode) of the diagnostic. For the AUG systems, detailed edge DR measurements are obtained by regulating the plasma density such that the frequency range of the reflectometer

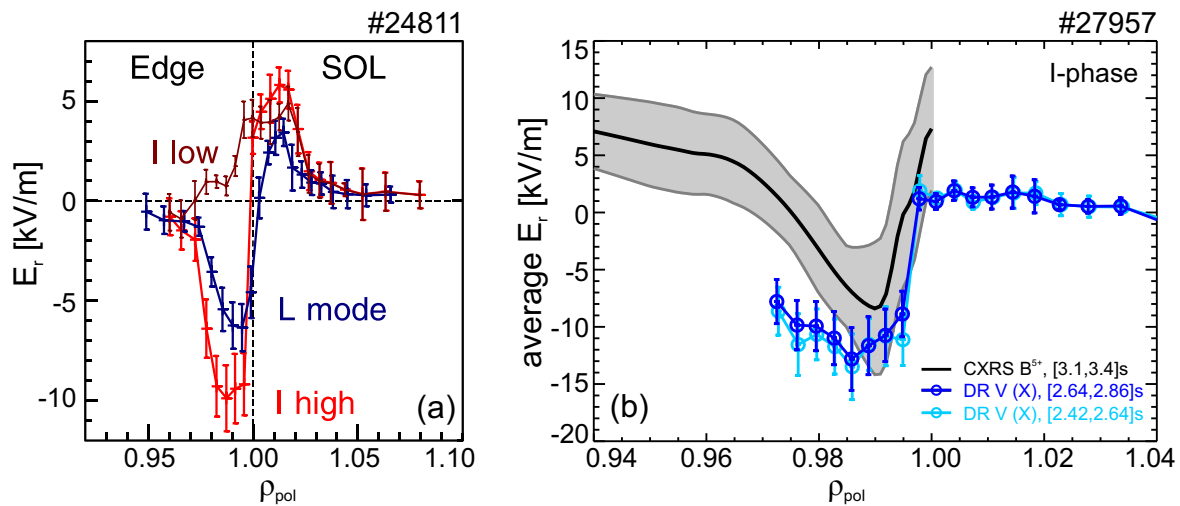


Figure 5.5: (a) Example profiles of E_r in L-mode and E_r oscillations during the I-phase as measured with DR (reprinted from [68]), (b) comparative experiment between CXRS and DR measurements: average E_r profile derived from CXRS (black) and DR (blue) during the I-phase.

(see section 3.1.2) is covered. In contrast, the CXRS diagnostics depend only on the heating beam #3 to provide a measurement of E_r .

To compare the E_r profiles obtained with both diagnostic techniques dedicated discharges were conducted. Two experiments were designed to obtain both a low density L-mode plasma and an H-mode plasma. The L-mode discharge was performed with $B_\phi = -2.3$ T, $I_p = 0.8$ MA, 1 MW of NBI heating and a central line-averaged density of $3.1 \times 10^{19} \text{ m}^{-3}$. At 0.8 MA the density dependence of the L-H power threshold exhibits a minimum of $P_{L-H} \approx 1$ MW at about $\bar{n}_{e,min} \approx 3.5 \times 10^{19} \text{ m}^{-3}$ [131]. Thus, the plasma was close to accessing the H-mode. At low densities the L-H transition is typically preceded by an intermediate limit cycle phase [68]. This intermediate state, the so-called I-phase [68], is obtained by starting from a low density L-mode plasma and increasing either the density or the heating power. The onset of the I-phase is characterized by an increase in the turbulence level across the whole plasma edge, which then starts to pulsate at 2–4 kHz [68]. The pulsing in the turbulence affects the mean flow shear on the turbulence timescale ($\sim \mu\text{s}$) and a strong modulation of E_r , which is synchronized with the turbulence level, is observed.

Figure 5.5(a) shows example profiles of the oscillatory behaviour of E_r during an I-phase (#24811) as measured by Doppler reflectometry [68]. In the comparative experiment (#27957) presented here the density increased slightly such that the plasma entered into the I-phase regime. The density and the heating power were then kept constant such that the I-phase was maintained for several seconds of the discharge. The time resolution of the edge CXRS diagnostics (2.2 ms) is too slow to resolve the cyclic variation of E_r . However, the average profile of these oscillations in E_r is measured by CXRS. Figure 5.5(b) shows the E_r profile derived from the CXRS measurements in black and the average E_r as obtained with DR (V-band, X-mode polarization) in blue. To reconstruct the average profile with DR (see figure 5.5(b)) each frequency step is averaged over a time period of 10 ms, while for the E_r profiles (labelled with ‘I low’ and ‘I high’) shown in figure 5.5(a) the measured data was synchronized with respect to the onset of a turbulence pulse. As the plasma density was rather low in the presented discharge only the V-band system in X-mode could resolve the plasma edge. While

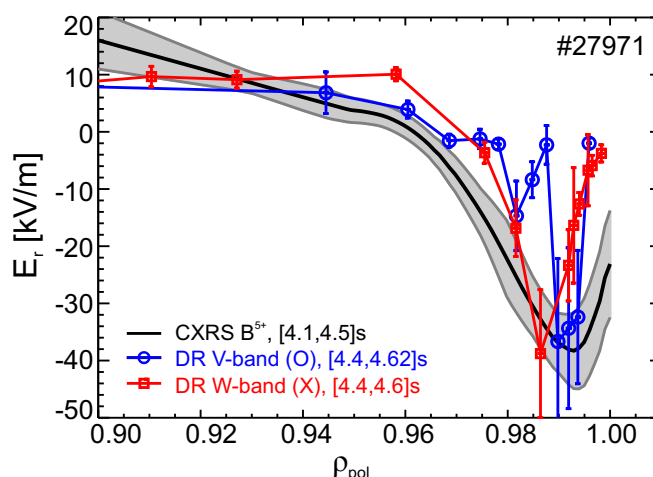


Figure 5.6: Radial electric field profile derived from CXRS (black) and DR measurements (blue and red).

for CXRS high radially resolved measurements were obtained by performing a radial plasma sweep, the DR profiles result from frequency sweeps over a time period of 220 ms. It may be noted that the DR measurements are a trade-off between radial resolution, which is determined by the number of frequency steps, and the accuracy of the Doppler shift, which is defined by the lower limit of the step length. The repetition rate of the profiles is thus given by the number of frequency steps and the step length. In the discharge dedicated to the comparison of the CXRS and DR measurements, the DR system was set to 22 steps of 10 ms.

The absolute magnitude and the radial location of the E_r well (cf. figure 5.5(b)) are in good agreement. The width of the E_r well appears to be narrower for the CXRS measurements which might arise due to the different characteristics of the radial resolution of each diagnostic (as discussed below). Note that the average E_r profile of the discharge presented in figure 5.5(a) (of the order ~ 5 kV/m) differs from the comparative experiment (figure 5.5(b)) as the plasma conditions and the heating power were different.

The second experiment presented was performed in H-mode with $B_\phi = -2.3$ T, $I_p = 0.8$ MA, 2.5 MW NBI, 1.7 MW ECRH and a central line-averaged density of $5.7 \times 10^{19} \text{ m}^{-3}$. A radial plasma scan was included to provide detailed edge CXRS profiles. The plasma density was regulated such that both the V-band and the W-band systems could resolve the edge pedestal. Figure 5.6 shows the E_r profile derived from CXRS measurements on B^{5+} in black and the profile obtained with DR in blue (V-band, O-mode polarization) and red (W-band, X-mode polarization). Good agreement is found for the depth of the E_r well and its radial position is consistent within the uncertainties of the diagnostics. The differences in the width of the E_r well result in different levels of E_r shear and might be explained by the radial resolution of each system. While the DR diagnostics rely on the local density profile to determine the exact measurement location, the CXRS measurements are fixed in real space. In addition, the location of the DR measurements might be sensitive to fluctuations of the edge density, which could explain the non-monotonic appearance of the E_r profiles from DR (i.e. at $\rho_{pol} \sim 0.985$ E_r decreases to almost 0 and then increases again). The turbulence level might affect the propagation of the electromagnetic wave and thus, the measurement location might be shifted from the actual position. Small changes in the local density profile can affect the radial localization of the E_r profile. The radial resolution of the DR systems depends on the density gradient, the frequency and the polarization. For the AUG DR diagnostics the radial resolution is of

the order $\lesssim 0.01$ in ρ_{pol} , while for the edge CXRS systems it is approximately 0.006. Further comparative measurements are needed to quantify the difference in the E_r shear.

5.3 Radial electric field at the inner and outer midplane

The novel charge exchange recombination spectroscopy (CXRS) measurements at the inner midplane of AUG enable the evaluation of the E_r profile at the high-field side (HFS) and a comparison to the beam-based measurements at the low-field side (LFS), thus allowing the study of possible asymmetries on a flux surface. In this section the question of whether the measured impurity flows, density and temperature profiles and the electrostatic potential form a consistent equilibrium is addressed.

5.3.1 CXRS measurements at the HFS

The temperature and rotation measurements at the HFS are obtained by injecting thermal D through a valve at the inner wall for the time period of interest (see section 4.2). Dedicated discharges have been carried out to compare the gas-puff based CXRS measurements at the HFS with the beam-based measurements at the LFS. The experiment presented here was performed in H-mode with B_ϕ on axis of -2.5 T, $I_p = 1$ MA, 5 MW NBI and 1.6 MW ECRH power. Figure 5.7 shows time traces of the (a) stored energy W_{mhd} , (b) line-averaged density in the plasma core and at the edge, (c) gas puff rate of the diagnostic valve and (d) radial plasma position at the outer midplane. The plasma is radially scanned through the views of the LFS and HFS diagnostics to measure detailed edge profiles. First, the plasma is moved towards the outer wall and then towards the inner wall (see figure 5.7(d)). Shortly before the plasma is moved to the HFS the gas puff is switched on (cf. figure 5.7(c)). Note that the gas puff and the radial plasma scan do not affect the stability of the plasma (see figure 5.7(a)-(b)).

Figure 5.8 shows inter-ELM profiles of (a) T_i , (b) poloidal and (c) toroidal rotation velocities

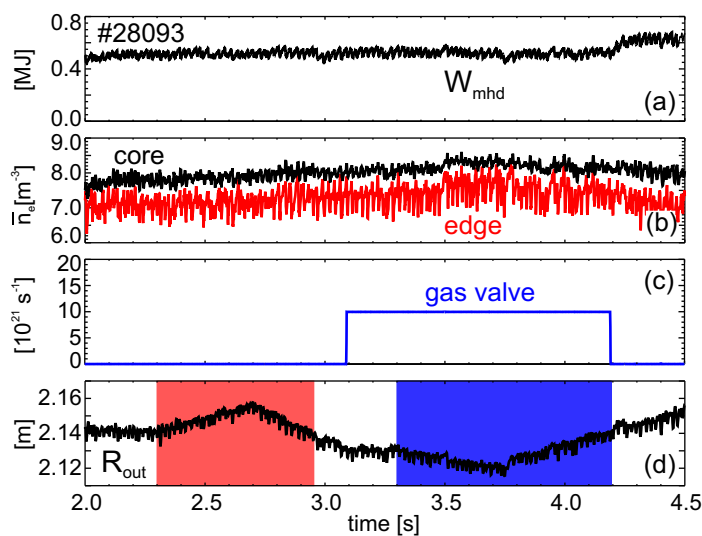


Figure 5.7: Time traces of discharge #28093: (a) stored plasma energy W_{mhd} , (b) line-averaged electron density in the plasma core and at the edge, (c) gas puff of diagnostic valve and (d) radial plasma position at the outer midplane.

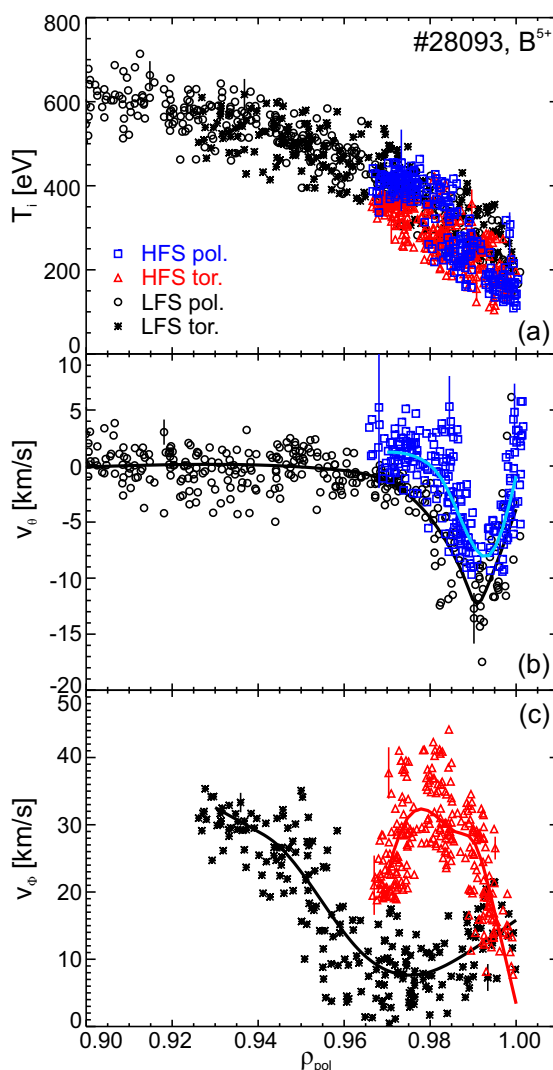


Figure 5.8: CXRS measurements at the HFS and LFS: (a) T_i , (b) poloidal rotation and (c) toroidal rotation of B^{5+} . Data obtained with the LFS systems are shown in black, while measurements from the HFS systems are shown in blue (poloidal view) and red (toroidal view). For better clarity the uncertainties of the measurements are shown at distinct radial positions.

measured at the HFS and LFS of AUG. The HFS measurements are limited to the outermost region of the plasma due to the penetration of the gas puff. The alignment of the HFS and LFS profiles is performed via the T_i profiles. Here it is assumed that the ion temperature is constant on the flux surface [132]. After aligning the HFS profiles with respect to those at the LFS, the following flow structure is observed: Inside the ETB the poloidal impurity flow exhibits a strongly sheared rotation in the electron diamagnetic direction both at the LFS and HFS. The HFS poloidal rotation velocity is about a factor of 1.5–2 lower than at the LFS. The toroidal rotation velocity is co-current at both the LFS and HFS, however, the profile exhibits an asymmetric structure [108]. At the LFS the toroidal rotation velocity exhibits a minimum located around the pedestal top [100], while at the HFS the profile is reversed and exhibits a maximum at this position (cf. figure 5.8(c)). Towards the separatrix the toroidal flow at the LFS increases, while it decreases at the HFS.

Both the toroidal flow asymmetry and the difference in magnitude of the poloidal flow might

be explained by an excess of impurity density at the HFS, as postulated in [133, 108] and observed in Alcator C-Mod [134]. A poloidal impurity density asymmetry can be inferred based on the neoclassical formalism for the total flow on a flux surface [133, 108]. Allowing for a poloidal dependence of the impurity density, the lowest order divergence-free flow of a species α on a flux surface is characterized by [27, 30, 133, 108]:

$$\mathbf{v}_\alpha = \omega_\alpha(\Psi) R \mathbf{e}_\phi + \frac{k_\alpha(\Psi)}{n_\alpha} B \mathbf{e}_\parallel \quad (5.2)$$

where ω_α and k_α are flux functions (defined below), Ψ is the poloidal magnetic flux, R the local major radius, \mathbf{e}_ϕ and \mathbf{e}_\parallel the unit vectors in the toroidal and parallel direction, n_α the impurity density and B the magnetic field. The divergence-free flow on a flux surface is a composite of the rigid body rotation (first term on the right-hand side of equation (5.2)) and the parallel flow. Using the sign convention defined in section 5.1, the following relations hold between the unit vectors in each direction:

$$\mathbf{e}_\parallel = \frac{B_\theta}{B} \mathbf{e}_\theta + \frac{B_\phi}{B} \mathbf{e}_\phi \quad \mathbf{e}_\perp = -\frac{B_\phi}{B} \mathbf{e}_\theta + \frac{B_\theta}{B} \mathbf{e}_\phi \quad (5.3)$$

$$\mathbf{e}_\phi = \frac{B_\phi}{B} \mathbf{e}_\parallel + \frac{B_\theta}{B} \mathbf{e}_\perp \quad \mathbf{e}_\theta = \frac{B_\theta}{B} \mathbf{e}_\parallel - \frac{B_\phi}{B} \mathbf{e}_\perp. \quad (5.4)$$

Here, B_θ and B_ϕ are the poloidal and toroidal magnetic field components and \mathbf{e}_\perp , \mathbf{e}_θ are the unit vectors in the perpendicular and poloidal direction, respectively. The flux function k_α is determined by taking the dot product of equation (5.2) with \mathbf{e}_θ :

$$\mathbf{v}_\alpha \cdot \mathbf{e}_\theta = v_{\theta,\alpha} = \frac{k_\alpha(\Psi)}{n_\alpha} B_\theta \quad \Rightarrow \quad k_\alpha(\Psi) = \frac{n_\alpha}{B_\theta} v_{\theta,\alpha} \quad (5.5)$$

Assuming that the impurity density is a flux function, $k_\alpha(\Psi)$ would result in $k_\alpha(\Psi) = \frac{v_{\theta,\alpha}}{B_\theta}$ and thus, $v_{\theta,\alpha}$ is expected to scale with B_θ . The measurements presented above show that this dependence is violated. However, the condition of divergence-free flows may be fulfilled if a poloidal impurity density asymmetry exists [133, 108].

Using the flux constant k_α the impurity density at the HFS can be calculated directly from the measured poloidal rotation velocities via:

$$n_\alpha^{\text{HFS}} = n_\alpha^{\text{LFS}} \frac{v_{\theta,\alpha}^{\text{LFS}} B_\theta^{\text{HFS}}}{v_{\theta,\alpha}^{\text{HFS}} B_\theta^{\text{LFS}}}. \quad (5.6)$$

Here, n_α^{LFS} is the impurity density measured at the LFS.

Alternatively, the HFS impurity density profile may also be calculated using the toroidal rotation measurements at the HFS and both poloidal and toroidal rotation measurements at the LFS [108]. This allows a cross-check on the different evaluation methods and the assessment of the uncertainties arising due to e.g. radial alignment of the HFS and LFS profiles. Here the HFS impurity density is derived as follows. Taking the dot product of equation (5.2) with \mathbf{e}_\parallel yields:

$$\mathbf{v}_\alpha \cdot \mathbf{e}_\parallel = v_{\parallel,\alpha} = \omega_\alpha(\Psi) R \frac{B_\phi}{B} + \frac{k_\alpha(\Psi)}{n_\alpha} B = \omega_\alpha(\Psi) R \cos \delta + \frac{k_\alpha(\Psi)}{n_\alpha} B \quad (5.7)$$

where δ is the inclination angle of the magnetic field line. At both the LFS and HFS the cosine of δ is 1. Thus, the impurity density at the HFS may be obtained by solving equation (5.7) for

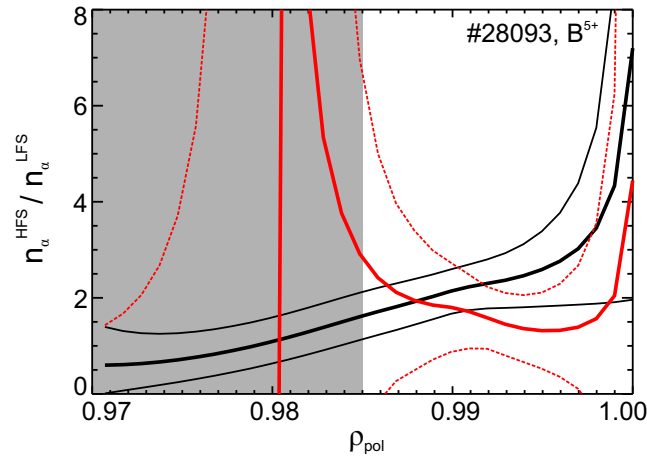


Figure 5.9: Impurity density asymmetry factors for B^{5+} as derived from the poloidal rotation measurements at the HFS and LFS in red and from parallel HFS/LFS and perpendicular LFS flows [108] in black.

the flux function $k_\alpha(\Psi)$ and rearranging for n_α^{HFS} :

$$n_\alpha^{\text{HFS}} = n_\alpha^{\text{LFS}} \left(\frac{v_{\parallel,\alpha}^{\text{LFS}} - \omega_\alpha R_{\text{LFS}}}{v_{\parallel,\alpha}^{\text{HFS}} - \omega_\alpha R_{\text{HFS}}} \right) \frac{B^{\text{HFS}}}{B^{\text{LFS}}}. \quad (5.8)$$

Here, $\omega_\alpha = \omega_\alpha(\Psi)$ is a flux function and can be derived by taking the dot product of equation (5.2) with \mathbf{e}_\perp :

$$\mathbf{v}_\alpha \cdot \mathbf{e}_\perp = v_{\perp,\alpha} = \omega_\alpha(\Psi) R \frac{B_\theta}{B} \quad \Rightarrow \quad \omega_\alpha(\Psi) = \frac{v_{\perp,\alpha}}{R} \frac{B}{B_\theta} = \frac{v_{\perp,\alpha}}{R \sin \delta} \quad (5.9)$$

Hence, using equation (5.8) the impurity density asymmetry may be calculated from the parallel and perpendicular velocities, which are determined by the toroidal and poloidal rotation measurements [108]. Figure 5.9 shows the asymmetry factors $n_\alpha^{\text{HFS}}/n_\alpha^{\text{LFS}}$ calculated from the poloidal rotation measurements (equation (5.6)) in red and using equation (5.8) in black. At $\rho_{\text{pol}} \sim 0.98$ the asymmetry factor calculated from the poloidal HFS and LFS rotation measurements exhibits a value of ~ 25 and then reverses (see red curve of figure 5.9). This behaviour is unphysical and arises due to the zero-crossing and sign change of the HFS poloidal rotation velocity at this radial position (see figure 5.8). In this region the uncertainty of the HFS measurement is significantly larger as the neutral density of the gas puff drops rapidly. For $\rho_{\text{pol}} > 0.985$ the profiles exhibit a different shape, however, the absolute values match within the uncertainties of the measurements.

A poloidal impurity density asymmetry may arise due to the interplay between inertia, friction, the pressure and the electric force and the orbit width effect in the parallel momentum balance [135]. The dominant mechanism responsible for the observed effect remains, as yet, unclear. For large poloidal impurity flows, which are present in the H-mode edge pedestal, the parallel impurity flow may approach the sound speed and the impurity density accumulates at the HFS leading to an asymmetric profile [136]. A direct measurement of the HFS n_α profile is not yet available as a measurement of the neutral density of the gas puff is missing. However, the radial electric field can be determined from the CXRS measurements at the HFS and LFS as the evaluation of the impurity pressure gradient term does not depend on absolute values of n_α , but rather on $\nabla n_\alpha/n_\alpha$. The influence of an asymmetric n_α profile on E_r is discussed in

the next section. The evaluation of the radial electric field at both poloidal positions enables a test of the consistency of the electrostatic potential with the flow structure on a flux surface (see next section).

5.3.2 Derivation of the electrostatic potential at the HFS and comparison to the LFS

The structure of the edge radial electric field E_r at both the HFS and LFS allows us to test if the electrostatic potential Φ is consistent with the measured impurity flows. For the determination of the impurity pressure gradient term at the HFS, which is part of the evaluation of E_r , two approaches are used: (i) the impurity density n_α is constant on a flux surface and (ii) n_α exhibits a poloidal asymmetry. For (ii) both formalisms of the impurity density asymmetry as described above are used.

Figure 5.10 shows the E_r profile at the LFS in black and at the HFS in red assuming that the impurity density is constant along the flux surface. The difference in the magnitude of E_r between the LFS and HFS is expected due to the different flux expansions of the magnetic field. The impact of an asymmetric n_α profile is shown in green (using equation (5.6) for the HFS n_α) and blue (using equation (5.8)). The green profile is restricted to the region $\rho_{pol} > 0.98$ since the asymmetry factor exhibits unphysical behaviour outside of this region (as discussed above). In both cases the impurity density asymmetry does not have a significant effect on the evaluation of E_r as the asymmetry enters the pressure gradient term of the radial force balance via the inverse gradient scale length $\nabla n_\alpha/n_\alpha$. In addition, the pressure gradient term in the radial force balance of B^{5+} is small compared to the poloidal rotation term. The fact that E_r is not affected by the impurity density asymmetry indicates that the electrostatic potential is determined by the dynamics of the main ion species only.

The electrostatic potential Φ can be derived from the E_r measurements using $E_r = -\nabla\Phi = -\frac{\partial\Phi}{\partial r}$ and is obtained by integrating E_r along the radial coordinate r . For this purpose two assumptions are used: one, it is assumed that the electrostatic potential is a flux function inside of the edge transport barrier, i.e. $\Phi_{ped,top}^{LFS} = \Phi_{ped,top}^{HFS} = \Phi_0$ is set as a starting condition at the pedestal top, where Φ_0 is chosen arbitrarily. Two, it is assumed that the potential at the HFS

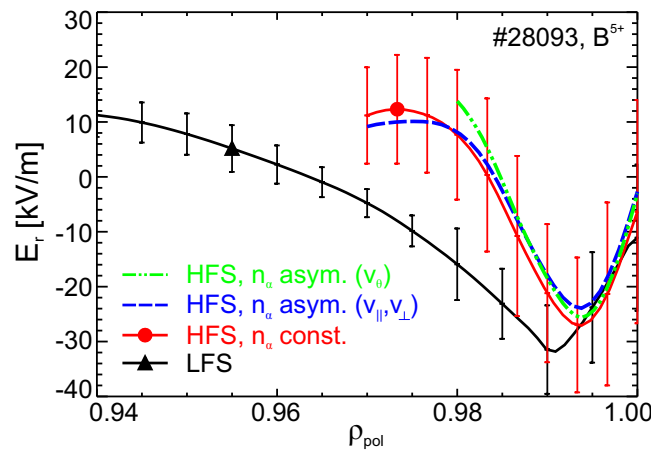


Figure 5.10: E_r profile at the LFS (black) and HFS using the assumption that the impurity density is a flux function (red) and assuming an asymmetric profile based on the poloidal rotation measurements (green) and based on the parallel and perpendicular flows (blue).

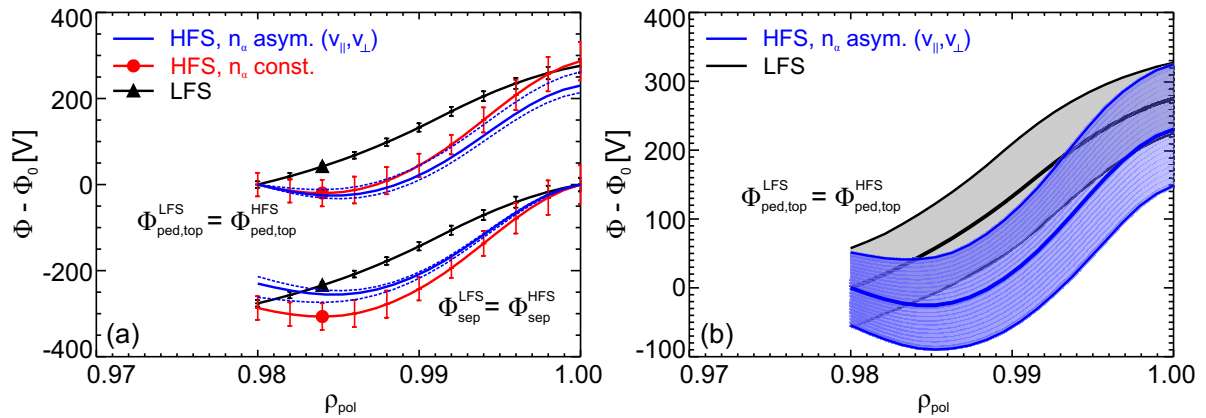


Figure 5.11: Electrostatic potential at the LFS in black and at the HFS in red (using a symmetric n_α profile) and in blue (n_α is asymmetric): (a) The upper profiles have been evaluated using the assumption $\Phi_{ped,top}^{LFS} = \Phi_{ped,top}^{HFS} = \Phi_0$, while for the lower profiles Φ_0 is set constant at the separatrix. The error bars reflect the uncertainties in the E_r measurements. The dashed lines of the blue profiles show the effect of the uncertainties in the asymmetric n_α profile. (b) Here, the error bands have been estimated assuming an additional uncertainty of 2 mm due to the magnetic equilibrium and taking into account that an uncertainty in Φ_0 propagates into all the other error bars.

and LFS are the same at the separatrix, i.e. $\Phi_{sep}^{LFS} = \Phi_{sep}^{HFS} = \Phi_0$, and then integrated along the path to obtain the profile in the ETB.

Figure 5.11(a) shows the electrostatic potential obtained using both assumptions on Φ_0 . The profile at the LFS is shown in black, at the HFS using a symmetric n_α profile in red and an asymmetric profile in blue. For better clarity only the evaluation using the n_α asymmetry factor as obtained from the parallel and perpendicular rotation measurements (equation (5.8)) is shown. In both cases ($\Phi_{ped,top}^{LFS} = \Phi_{ped,top}^{HFS}$ and $\Phi_{sep}^{LFS} = \Phi_{sep}^{HFS}$) the electrostatic potential at the HFS exhibits a stronger curvature in the ETB than at the LFS, while Φ reaches almost the same value at the separatrix and at the pedestal top, respectively. The error bars shown in figure 5.11(a) reflect the uncertainties of E_r only. However, additional uncertainties arise due to the magnetic equilibrium and due to the choice of where Φ_0 is set, since the error bar on the local radial electric field at this position will propagate into all the other error bars when the radial electric field is integrated along r . The uncertainties due to the magnetic equilibrium have been estimated assuming an error in r of 2 mm. Figure 5.11(b) shows the resulting error bands for the case $\Phi_{ped,top}^{LFS} = \Phi_{ped,top}^{HFS} = \Phi_0$. These have been calculated using Gaussian error propagation including the uncertainties in the local E_r , an error in the radial position, r , and taking into account that an uncertainty arising from the choice of the location of Φ_0 propagates into the other error bars. Within these uncertainties, the electrostatic potential is constant along the flux surface.

Chapter 6

Connections between the radial electric field and the edge transport barrier

It is widely acknowledged that the radial electric field E_r and its shear play a crucial role in the physics governing the L-H transition. The associated $\mathbf{E} \times \mathbf{B}$ velocity shear is thought to be important in the shear turbulence suppression feedback loop which is required to enter into the H-mode. As discussed in chapter 2 the radial electric field and the gradients in the main ion species are intimately interlinked. In this chapter the E_r profiles derived from the new edge charge exchange recombination spectroscopy (CXRS) diagnostics (see chapter 4) are compared to the main ion pressure gradient term. The structure of the E_r well is analyzed as a function of pedestal parameters and the possible connection between edge E_r profiles and global plasma energy confinement is examined. The evolution of the E_r profile during an edge localized mode cycle as well as the effect of externally applied magnetic perturbations on E_r is studied.

6.1 Comparison of the radial electric field to the main ion pressure gradient term

The radial electric field E_r is supposed to be driven by the main ions, typically deuterium at AUG, and not by the impurities. However, measurement of the main ion population using CXRS is difficult to interpret due to the large background emission and a weak localization of the active signal due to the thermal beam halo [5], which is produced by charge transfer from beam neutrals to deuterium ions. Usually, CXRS measurements are performed on impurity ions since the diagnostic method is easily applicable. Since E_r is the same for every species, the profile derived from the impurity ions allows information on the main ion species to be obtained indirectly. For this purpose, an estimate of the pressure gradient term of deuterium is calculated for the measured data presented in section 5.1 using the assumption of quasi-neutrality and two assumptions on the ion density profile: (i) constant dilution, $n_i \propto n_e$ (n_i being the main ion density and n_e the electron density), leading to

$$\frac{\nabla p_i}{n_i} = \frac{\nabla(n_i T_i)}{n_i} = \frac{C \nabla n_e T_i + \nabla T_i}{C n_e} = \frac{\nabla n_e T_i}{n_e} + \nabla T_i \quad (6.1)$$

and (ii) radially varying dilution with $n_i = n_e(1 - \sum_{\alpha} Z_{\alpha} c_{\alpha})$, c_{α} being the radially dependent concentration of the impurity species α . The main ion density profile has been evaluated from

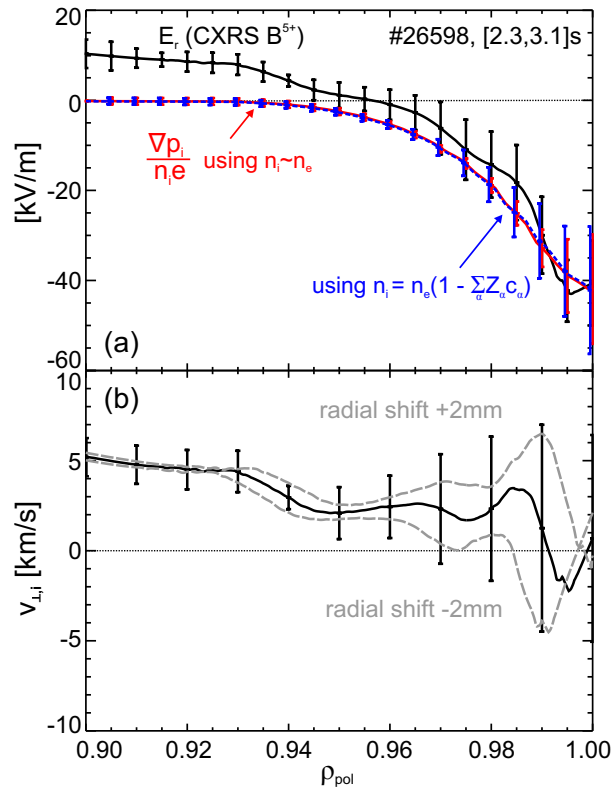


Figure 6.1: (a) Comparison of E_r (black curve) to an estimate of the main ion pressure gradient term assuming constant dilution (red curve) and correcting for the effect of impurities (blue curve), (b) derived perpendicular main ion velocity. The dashed lines in the lower panel show the effect of a relative shift between electron and ion profiles by ± 2 mm.

the measured n_e profile and using the boron and carbon concentrations measured in subsequent discharges. In this case the radial concentration of boron (carbon) changes from 0.2 % to 0.5 % (0.4 % to 0.6 %) over the pedestal region.

Figure 6.1(a) depicts the E_r profile in black obtained from CXRS on B^{5+} , while the pressure gradient term of deuterium is shown in red. Here, T_i is used from the CXRS measurement, while n_e is taken from measurements with Thomson scattering (TS), the Li beam diagnostic (LIB) and the interferometry system. The T_i and n_e profiles have been aligned relative to each other as described in section 3.3. The modification of the main ion pressure gradient term due to a non-constant dilution (see blue dashed line in figure 6.1(a)) is found to be small (the maximum difference is less than 1.5 kV/m).

The pressure gradient term of deuterium is very similar to E_r indicating that for the main ions the pressure gradient term is the main contribution in the radial force balance. From this comparison an estimate of the perpendicular flow velocity of the main ions, $v_{\perp,i}$, can be calculated via a rearrangement of the radial force balance (see equation (5.1)):

$$v_{\perp,i} = \frac{1}{B} \left(E_r - \frac{1}{e} \left(\frac{\nabla n_i}{n_i} T_i + \nabla T_i \right) \right) \quad (6.2)$$

In figure 6.1(b) the calculated main ion fluid velocity perpendicular to the magnetic field is shown. The perpendicular main ion flow is positive, i.e. in the ion diamagnetic drift direction. Note that $v_{\perp,i}$ is rather small in magnitude, approaching $v_{\perp,i} = 0$ inside the ETB, similar to results obtained at Alcator C-Mod [17]. The dashed lines in figure 6.1(b) show the effect of a

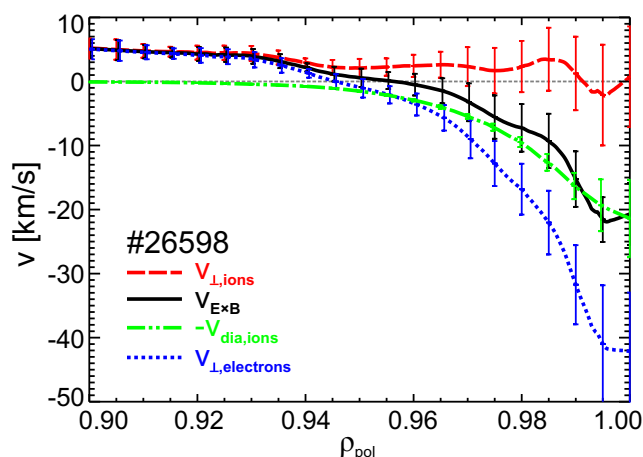


Figure 6.2: $\mathbf{E} \times \mathbf{B}$ velocity (black), main ion diamagnetic fluid velocity (multiplied by -1, green) and perpendicular velocities of main ions (red) and electrons (blue).

radial shift of ± 2 mm in alignment between the n_e and T_i measurements.

The fact that the perpendicular ion fluid velocity is approximately zero indicates that the $\mathbf{E} \times \mathbf{B}$ drift and the ion diamagnetic drift are almost in balance at the plasma edge. Figure 6.2 shows the perpendicular velocity of the main ions (red) and electrons (blue), the $\mathbf{E} \times \mathbf{B}$ velocity (black) and the ion diamagnetic drift velocity (multiplied by -1, green). The perpendicular velocity of the electrons is evaluated using equation (6.2), i.e. using the measured E_r profile and the measured electron density and temperature profiles. The perpendicular electron flow velocity is almost twice the electron diamagnetic drift velocity (which is almost the same as the ion diamagnetic drift but in the opposite direction, i.e. negative) since the $\mathbf{E} \times \mathbf{B}$ drift and the electron diamagnetic drift add up. This is also consistent with $\nabla p = \mathbf{j} \times \mathbf{B}$, i.e. a current \mathbf{j} perpendicular to the magnetic field balances with the pressure force. Since the main ion fluid is at rest, the electrons have to speed up to fulfill this condition.

Helium plasmas provide the opportunity to obtain direct information on the temperature, density and velocity of the main ion species by using CXRS on He^{2+} . These measurements have been performed in an H-mode discharge with $B_\phi = -2.5$ T, $I_p = 1.0$ MA, 0.5 MW ECRH, 9.2 MW deuterium NBI heating and a central line-averaged density of $1.1 \times 10^{20} \text{ m}^{-3}$. At the plasma edge E_r is found to be dominated by the pressure gradient term of He^{2+} , while the Lorentz force term is small and approaches zero close to the separatrix (see figure 6.3(a)). In the analysis the plume effect is not taken into account. The helium plume is caused by He^+ ions, excited via electron impact (or ion impact), which gyrate along the magnetic field lines and thus, would lead to a polluting emission in the spectrum. At the plasma edge the contribution of the helium plume is expected to be small [5]. This is also confirmed by independent density measurements using LIB, TS and the interferometry diagnostic: as expected, the helium density is found to be half the electron density and the gradients match, i.e. $\nabla n_{\text{He}} = \nabla n_e / 2$. Figure 6.3(b) shows the measured helium density profile, along with a fit (in red, solid line) and a fit to the electron density profile (blue dashed line). The fit to n_e has been scaled by a factor of 2.

These results are in agreement with neoclassical theory [27] which predicts that to zeroth order, and in case of small toroidal rotation velocities, the edge E_r is balanced by the ion pressure gradient normalized to the ion density. Quantitative comparisons between measurements and neoclassical codes are presented in chapter 7.

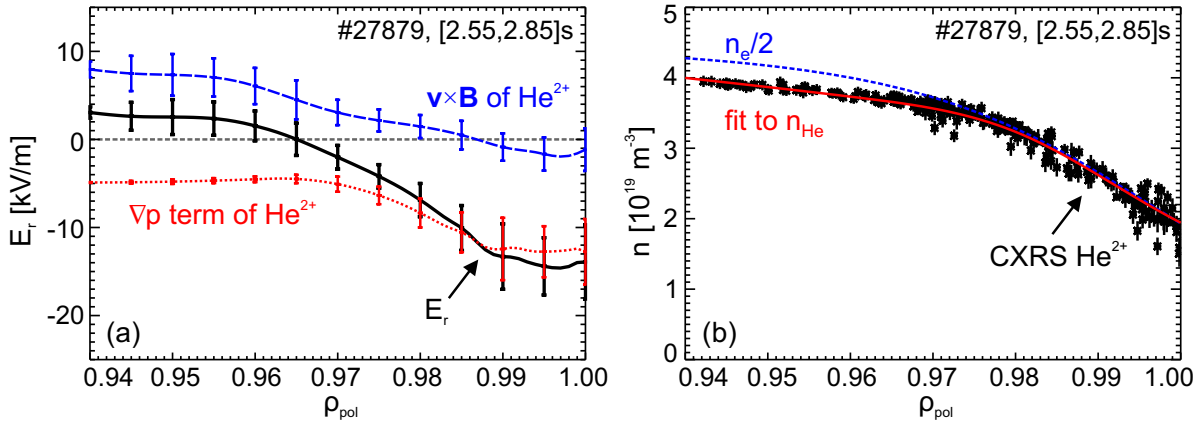


Figure 6.3: CXRS measurements in a helium plasma: (a) E_r profile in black, pressure gradient term of He^{2+} in red (dotted line) and $\mathbf{v} \times \mathbf{B}$ term of He^{2+} in blue (dashed line), (b) measured helium density profile in black, fit in red and fit to the electron density profile in blue (dashed line). The fit to n_e is scaled by a factor of 2.

6.2 Radial electric field profiles in different confinement regimes

Previous work on several devices has demonstrated a connection between edge E_r profiles and global plasma energy confinement [137, 12, 6, 24, 17, 67]. This connection has also been examined in AUG discharges using the data from the new edge CXRS systems. In order to explore this over the widest range of plasma parameters possible, E_r profiles have been collected from many different types of discharges including L-, I-, H- and improved H-mode plasmas. Figure 6.4(a) shows the E_r profile obtained in an L-mode plasma with B_ϕ on axis of -2.5 T, I_p of 1 MA and 1 MW NBI heating. The CX measurements were performed on He^{2+} . In L-mode the radial electric field is generally small in magnitude and consequently exhibits weak gradients. In this confinement regime all impurity components are important for the evaluation of the E_r well (cf. figure 6.4(a)). I-mode plasmas [138], originally referred to as ‘improved L-mode’ at ASDEX Upgrade [139], are characterized by similar energy confinement times as

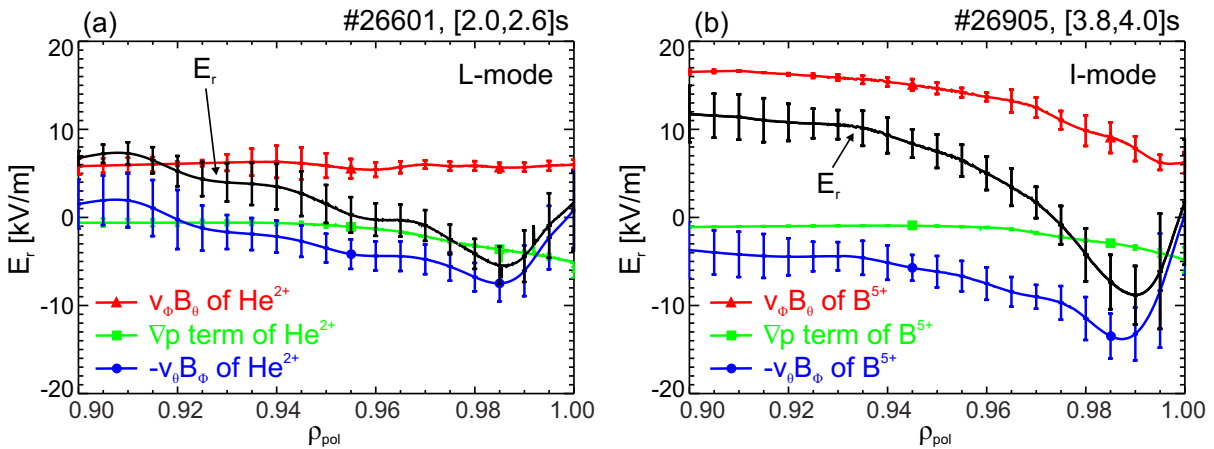


Figure 6.4: Radial electric field profile in (a) L-mode and (b) I-mode.

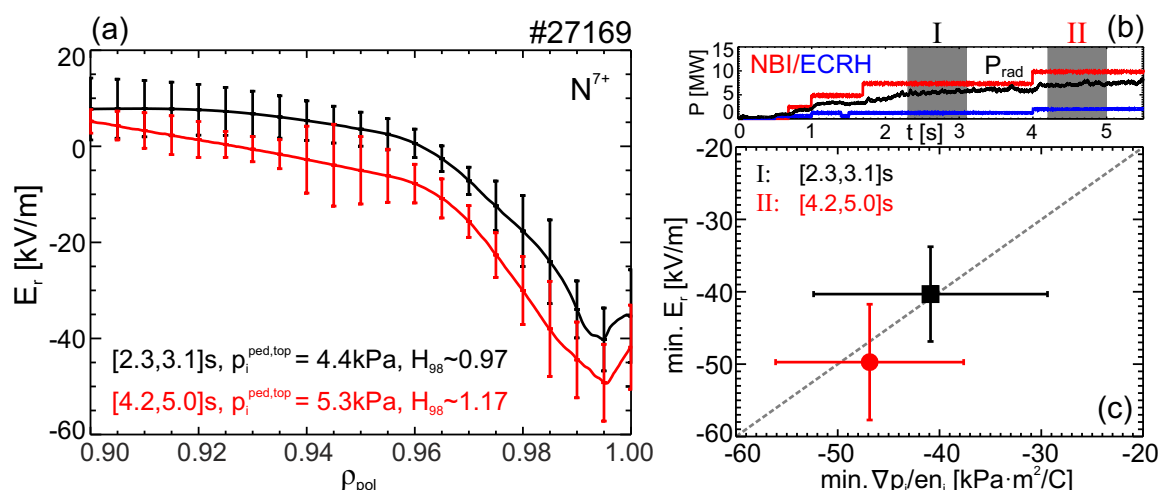


Figure 6.5: (a) Radial electric field profiles obtained in an improved H-mode discharge with different pedestal top ion pressures $p_i^{ped,top}$ (at $\rho_{pol} = 0.97$) and different H/L scaling factors $H_{98}(y,2)$ [96], (b) time traces of NBI, ECRH and radiated power (P_{rad}), (c) minimum of E_r versus minimum of main ion pressure gradient term.

the H-mode, however, the particle confinement is near L-mode levels. In the I-mode regime the depth of the E_r well is found to be intermediate between L- and H-mode and dominated by the poloidal impurity rotation contribution (see figure 6.4(b)).

The radial electric field has also been studied in improved H-mode discharges with nitrogen (N_2) seeding. At AUG improved confinement is observed when using nitrogen as a low-Z radiator to protect the divertor in high power discharges [140]. In these plasmas the CX measurements are performed on a nitrogen line, i.e. N^{7+} ($n = 9 \rightarrow 8$) at $\lambda = 566.937$ nm. Figure 6.5(a) shows the resulting E_r profiles obtained in two phases with different pedestal top pressures. N_2 seeding was applied throughout the whole discharge and the energy confinement increased from phase I to phase II. The E_r well is observed to deepen with higher pedestal top pressures.

The effect of increasing the NBI heating was studied in the improved H-mode discharge and two different phases with 7.5 and 10 MW NBI (see figure 6.5(b)) were analyzed. Increasing the momentum input and thus, changing the core rotation of the plasma, has no observable effect on the relation between the radial electric field and the main ion pressure gradient term at the plasma edge (cf. figure 6.5(c)). This result supports that in H-mode E_r assumes a value such that the E_r well is in balance with the gradients in the main ion species and the perpendicular flow of the main ions vanishes at the plasma edge.

6.3 Interdependences between the radial electric field, its shear and pedestal parameters

Combining the results obtained in the different plasma regimes introduced in section 6.1 and 6.2 shows that the minimum of E_r is correlated with the ion pressure at the pedestal top. Figure 6.6 shows the minimum of E_r as a function of the (a) ion temperature $T_i^{ped,top}$, (b) ion density $n_i^{ped,top}$ and (c) ion pressure $p_i^{ped,top}$ near the pedestal top ($\rho_{pol} = 0.97$). For the evaluation of $n_i^{ped,top}$ the dilution due to the impurity concentration as measured by CXRS has

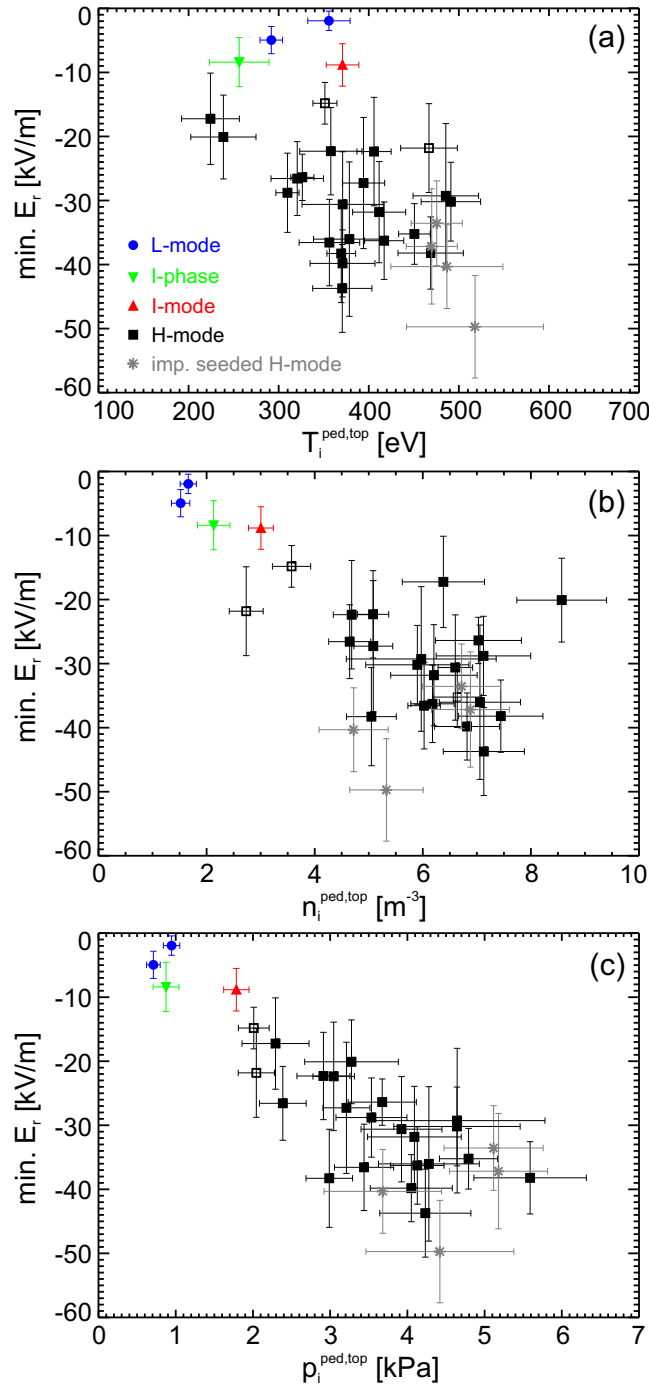


Figure 6.6: Depth of the E_r well as a function of the (a) pedestal top ion temperature $T_i^{ped,top}$, (b) pedestal top ion density $n_i^{ped,top}$ and (c) pedestal top ion pressure $p_i^{ped,top}$ (at $\rho_{pol} = 0.97$).

been taken into account. Data obtained in impurity seeded H-modes (including the improved H-mode discharge) are marked in grey, while the I-phase data point (as presented in section 5.2.2) is highlighted in green. The data points measured in He plasmas are marked with black open squares. No direct correlation is found between the minimum of the E_r well and the ion temperature at the top of the pedestal. A weak trend between deeper E_r wells and higher ion densities at the pedestal top is observed, however, within the H-mode data, the scatter is rather large and no clear correlation is found. The best correlation is found between the minimum

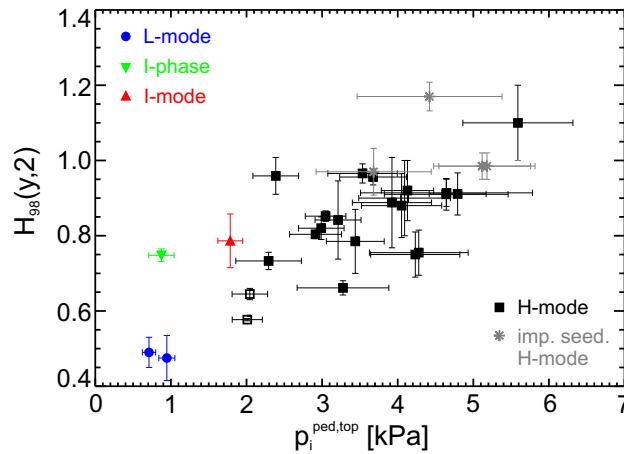


Figure 6.7: Energy confinement factor $H_{98}(y,2)$ as a function of $p_i^{ped,top}$.

of the E_r well and $p_i^{ped,top}$ (see figure 6.6(c)). Using a linear least-squares approximation, the smallest χ^2 , which is a measure for the goodness of a fit, is obtained for the fit of the E_r minimum as a function of $p_i^{ped,top}$ (χ^2 is a factor of 2 and 4 lower with respect to fitting the E_r minimum versus $n_i^{ped,top}$ and $T_i^{ped,top}$).

In general, it is observed that for higher pedestal top pressures the E_r well is deeper, further confirming that E_r corresponds to the main ion pressure gradient term.

Figure 6.7 shows the interdependence of the energy confinement factor $H_{98}(y,2)$ with respect to the ITER confinement scaling [96] and $p_i^{ped,top}$. The energy confinement increases for higher pedestal top ion pressures as a result of stiff T_i gradient scale lengths. In figure 6.8 the minimum of E_r is plotted against the global energy confinement factor $H_{98}(y,2)$. Moving from L- to H-mode the E_r well deepens and the energy confinement of the plasma increases. However, within the H-mode the scatter is substantial and only a weak correlation between the depth of the E_r well and $H_{98}(y,2)$ is found. Due to the density dependence of the $H_{98}(y,2)$ -scaling ($\propto \bar{n}_e^{0.41}$, \bar{n}_e being the line-averaged electron density) the same $p_i^{ped,top}$ value can result in different $H_{98}(y,2)$ -factors. This may explain the observation of deep E_r wells, or higher pedestal top pressures, at lower energy confinement factors (~ 0.75 , cf. figure 6.8). These data points were measured in high density H-mode plasmas ($n_i^{ped,top} \sim 7 \times 10^{19} \text{ m}^{-3}$), where the $H_{98}(y,2)$ -scaling, which depends on the density, may not be valid [141].

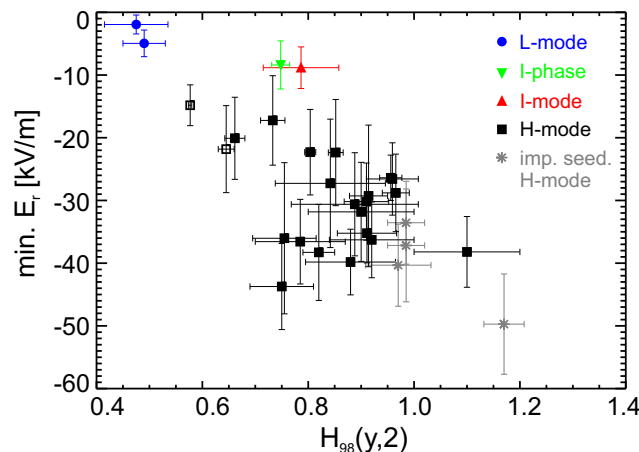


Figure 6.8: Depth of E_r well versus energy confinement factor $H_{98}(y,2)$.

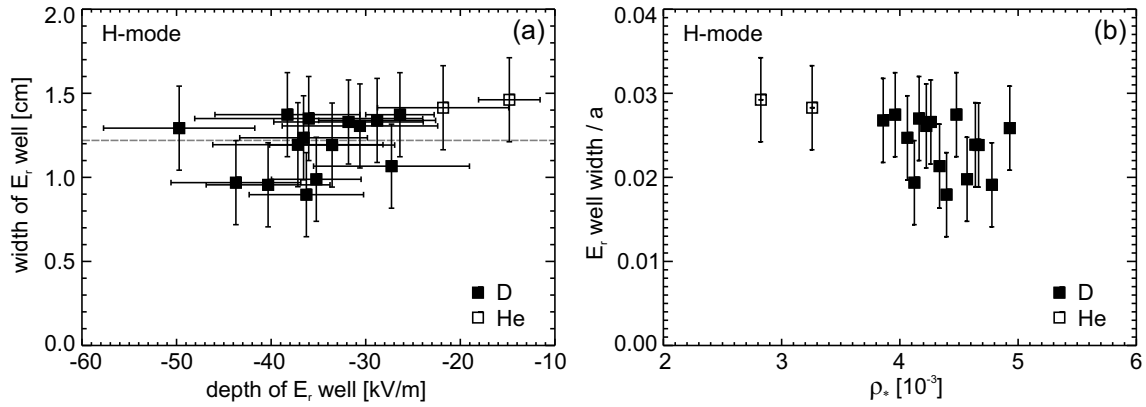


Figure 6.9: (a) Width versus depth of E_r well in H-mode plasmas, (b) E_r well width, normalized to the minor radius a , plotted as a function of the normalized toroidal Larmor radius ρ_* . Data measured in D plasmas are marked by black squares, while data obtained in He plasmas are highlighted by open squares.

Recent results at Alcator C-Mod [17] showed that in H-mode the width of the E_r well scales with the size of the machine. This relationship has also been examined at AUG using the E_r data from the new edge CXRS diagnostics. Only data from fully developed H-mode discharges performed in deuterium and helium plasmas were included in the study. Here, the width of the E_r well is defined as the full width at half maximum (FWHM), whereas the half width at half maximum of the E_r well is determined from the measured profile and then multiplied by 2 to obtain the FWHM. Figure 6.9(a) shows the width of the E_r well plotted against the depth of E_r . The uncertainty of the width determination is given by the radial resolution of the diagnostics (5 mm for the poloidal system). Only small variations in the E_r well width are found consistent with data from C-Mod [17]. On average the width is 1.2 cm with a standard deviation of 0.2 cm.

Figure 6.9(b) shows the E_r well width, normalized to the minor radius a , plotted as a function of the normalized toroidal Larmor radius ρ_* , which is defined as $\rho_* = \frac{r_{L,i}}{a} = \frac{\sqrt{2m_i k_B T_i}}{q_i B_\phi a}$ where m_i and q_i are the mass and charge of the ion species i . The variations in the normalized E_r well width are found to be small despite changing the ion temperature, magnetic field and the plasma particle species (D and He).

Combining the E_r well width from AUG with data from other machines supports the scaling of the E_r well width with the size of the machine [17]. Figure 6.10(a) shows the average width of the E_r well at AUG in comparison with E_r well widths measured at Alcator C-Mod [17], DIII-D [14, 13], JET [15] and JFT-2M [142] (adapted from [17]). The data points from AUG, Alcator C-Mod, DIII-D and JET support the machine size scaling while the data from JFT-2M differs by a factor of 2, which might be explained by the uncertainty of the diagnostic technique as a combination of passive and active views in different toroidal sectors were employed.

At DIII-D [14] and Alcator C-Mod [17] the width of the E_r well did not vary significantly despite changing the plasma parameters, such as plasma current, magnetic field, temperature and density. The normalized toroidal Larmor radius ρ_* varied from 3.2–5.3 at Alcator C-Mod [17], 4.9–9.9 at DIII-D [14, 13], 1.4 at JET [15] and 7.3 at JFT-2M [142]. The values for ρ_* were evaluated using the published data from these machines.

Figure 6.10(b) shows the width of the E_r well normalized to the minor radius a of the plasma plotted against a . The data from AUG, Alcator C-Mod, DIII-D and JET suggest that indepen-

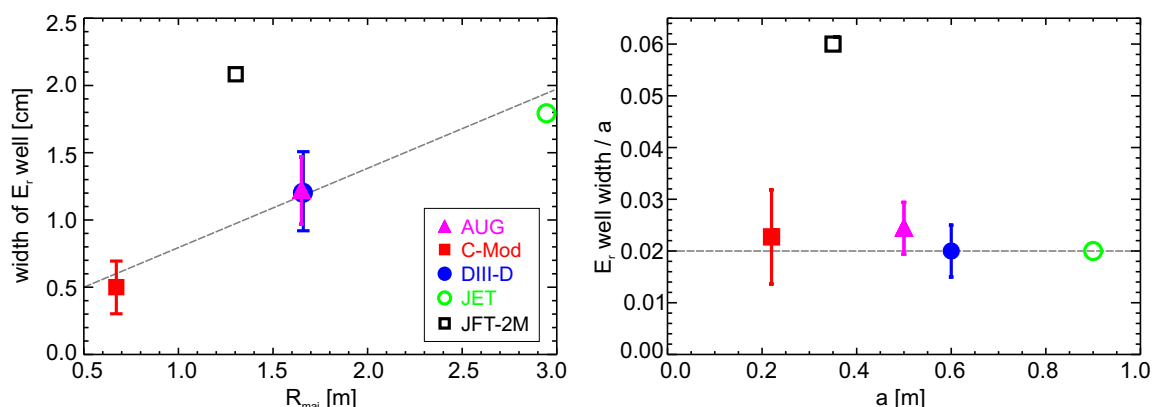


Figure 6.10: (a) E_r well width plotted against the major radius R_{maj} of the machine (data from C-Mod, DIII-D, JET and JFT-2M reprinted from [17]), (b) width of the E_r well, normalized to the minor radius a of each machine, plotted as a function of the minor radius.

dently of the size of the machine, the width of the E_r well corresponds to $\sim 2\%$ of the minor radius. Using this scaling, the width of the E_r well in ITER (with a minor radius of 2 m [143]) is estimated to 4 cm.

Studying the position of the minimum of the E_r well in H-mode shows that for deeper E_r wells the minimum appears to move towards the separatrix. This finding also suggests that the steepest gradients in the kinetic profiles should shift towards the separatrix. Note that this movement is observed in fully developed H-mode discharges and may be different when moving from L- to H-mode as reported in [84]. Figure 6.11 shows the distance of the minimum of E_r from the separatrix plotted against the depth of the E_r well. The uncertainty of determining the position of the E_r minimum is given by the uncertainty of the radial profile alignment, i.e. 2–3 mm (see section 3.3). For two cases the radial distance of the minimum in the main ion pressure gradient term $\nabla p_i/n_i e$ was analyzed (marked by blue stars in figure 6.11), which shows the same systematic trend. This supports that the radial alignment of the edge kinetic profiles is very accurate for the present work and is well suited to study effects on

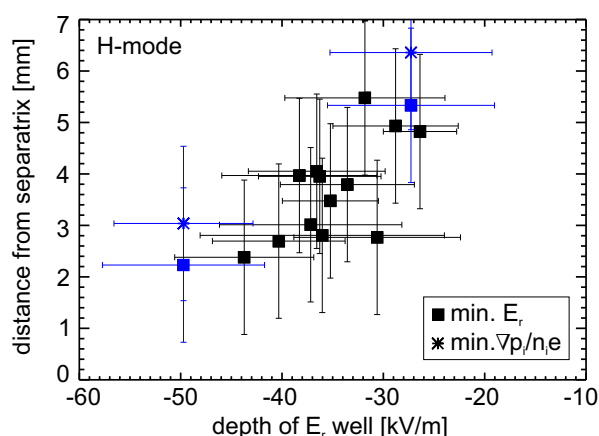


Figure 6.11: Distance of the E_r minimum from the separatrix versus depth of the E_r well. The deepest and one of the more shallower E_r wells are highlighted in blue. The corresponding data points for the main ion pressure gradient term (i.e. the distance of the minimum in the main ion pressure gradient term from the separatrix) are marked by stars for the two cases shown in blue.

the mm range. The physical mechanism behind the radial movement remains, as yet, unclear as the relative positioning of both the density and temperature profiles and their gradients is crucial. However, for the two cases highlighted in blue in figure 6.11 the radial distance of $\nabla p_i/n_i e = (T_i \nabla n_i/n_i + \nabla T_i)/e$ from the separatrix was disentangled into the distance of $T_i \nabla n_i/n_i$ and ∇T_i . For these two data points the $T_i \nabla n_i/n_i$ term seems to move towards the separatrix, while the ∇T_i term stays close to the separatrix and does not move significantly. This indicates that for deeper E_r wells the radial distance between the steepest ∇n_i and ∇T_i decreases. This result is not unexpected since the pedestal widths for the electron temperature and density are observed to be different [144]. A statistical analysis including detailed edge profiles is needed to identify the mechanism responsible for this movement.

Within the framework of turbulence reduction theory through $\mathbf{E} \times \mathbf{B}$ shear [4], the following picture emerges from the measurements obtained with the new edge CXRS diagnostics: for

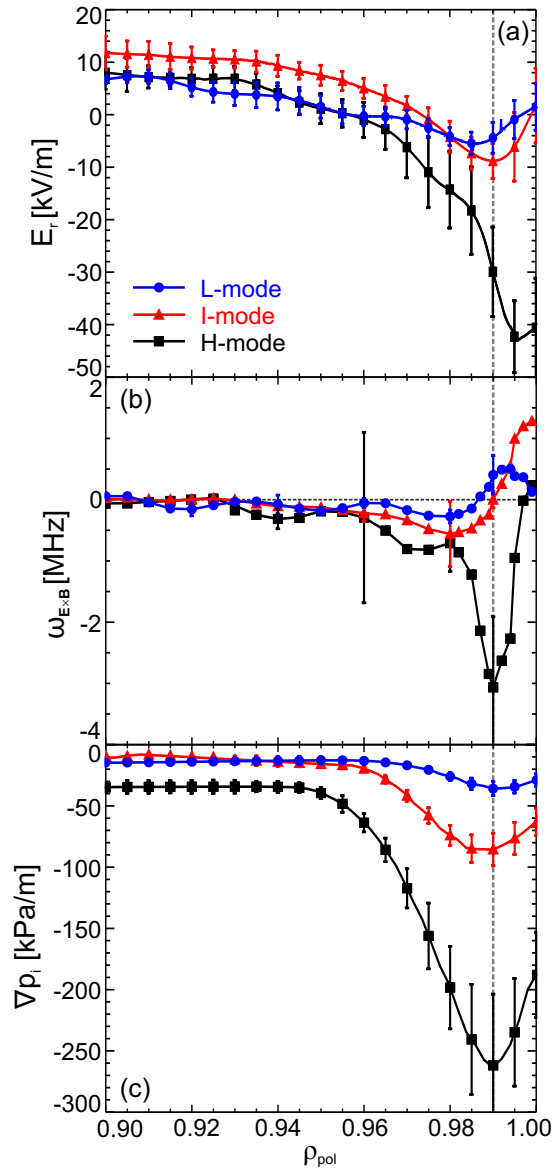


Figure 6.12: L-, I- and H-mode: (a) E_r profile and (b) resulting E_r shear. For better clarity the uncertainties are only shown for distinct radial positions. (c) Radial profile of the main ion pressure gradient, ∇p_i .

constant E_r well widths and if the zero-crossing point of E_r stays approximately constant, deeper E_r wells have higher E_r shearing rates which increase the efficiency of turbulence reduction when moving from L- to H-mode. This leads to higher pedestal top pressures, which are correlated with the global plasma confinement due to stiff T_i gradient scale lengths in the core. Hence, also the magnitude of the E_r shear (defined as $\omega_{E \times B} = \frac{r}{q} \frac{\partial}{\partial r} \left(\frac{q}{r} \frac{E_r}{B} \right)$ [145]) correlates with the energy confinement and increases from L- to H-mode. Figure 6.12 shows (a) the E_r profiles and (b) the calculated E_r shear obtained in the different confinement regimes. In the low confinement regimes, i.e. L- and I-mode, the shear is weak (smaller than in H-mode) and comparable to the width of the turbulence spectrum (~ 100 – 200 kHz at the plasma edge [146]), while in the ETB of the H-mode the E_r shearing rate reaches values of up to 3 MHz. It is worth noticing that in H-mode the maximum shear coincides with the maximum ion pressure gradient, ∇p_i (see figure 6.12(c)), calculated using the n_e profile, giving confidence that the radial alignment of the gradients and E_r is very accurate. Note also that the maximum in the E_r shearing rate, or alternatively the steepest ∇p_i , lies in the inner part of the E_r well, indicating that the negative shear region is the important region for turbulence suppression consistent with previous results [147, 148, 24].

6.4 Temporal evolution of the radial electric field during an edge-localized mode cycle

Due to the occurrence of edge-localized modes (ELMs, see section 2.3.2) the steep edge gradients of H-modes flatten transiently during each event. The temporal resolution of the newly installed edge CXRS diagnostics (2.2 ms) enables a synchronization of the data with respect to the onset of an ELM. Thus, the behaviour of the radial electric field during the ELM crash can be analyzed in detail. To this end, the data from a set of reproducible type-I ELM cycles measured in a time window of 700 ms was sorted and mapped onto a time grid relative to the time of the closest ELM. In this phase the plasma was radially moved through the LOS of the CXRS diagnostics to obtain complete edge profiles.

The discharge used in the following analysis is identical to the one discussed in section 5.1. The ELM frequency was constant at ~ 80 Hz. Figure 6.13 shows the profiles measured on C^{6+} of (a) T_i , (b) spectral radiance of the CX line, (c) toroidal and (d) poloidal rotation velocity during the ELM cycle averaged over ~ 60 ELMs. The labels ‘-2.2 ms’, ‘0.0 ms’ and ‘+2.2 ms’ of figure 6.13 denote the relative time to the closest ELM at which the measurements were taken. Before the ELM T_i and the spectral radiance of the CX line exhibit a strong gradient at the edge, while the toroidal rotation has a minimum localized near the pedestal top. The poloidal rotation on the other hand exhibits a local minimum close to the separatrix. During the ELM (labeled with ‘0.0 ms’ in figure 6.13) the steep gradients flatten and the dips in both the toroidal and poloidal rotation vanish. Note that the integration time of the edge CXRS systems might be too long to quantitatively judge the behaviour of the impurity profiles, but the qualitative behaviour can be described. During the inter-ELM phase the signal in the scrape-off layer is not sufficient to analyze the CXRS spectral line, but when the ELM occurs the signal increases, indicating that the impurities are expelled, and the fits are trustworthy. The profiles start to recover and a pedestal forms already 2.2 ms after the ELM, however, the pre-ELM values are not yet reached in this early phase of recovery. This result is in agreement with experimental studies performed at DIII-D [149] and consistent with time scales of the

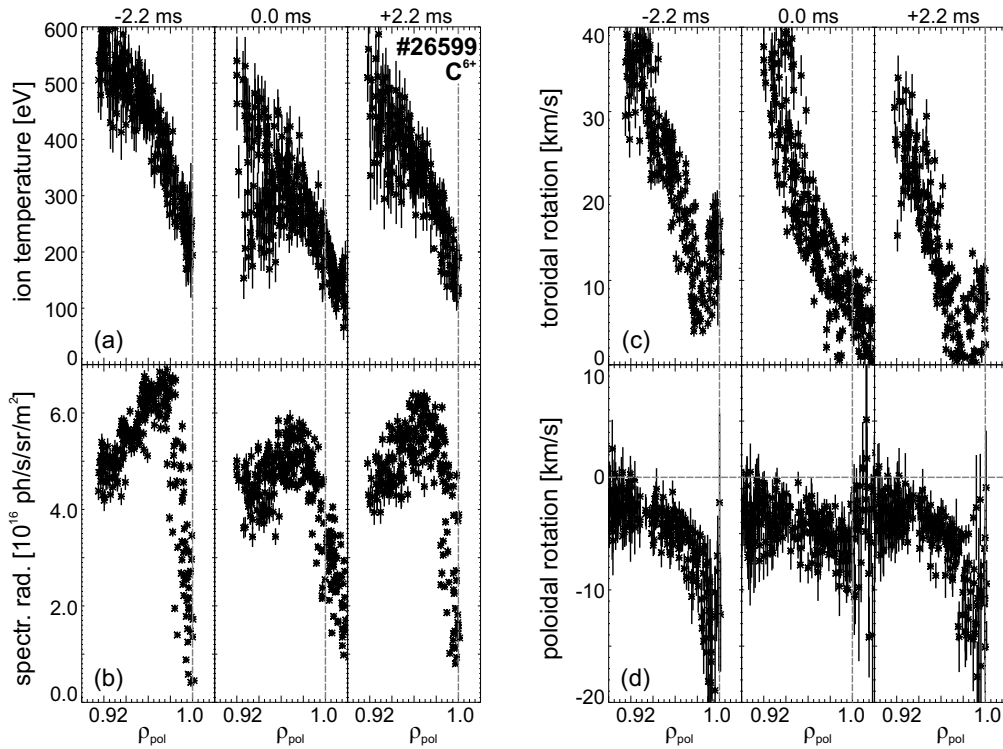


Figure 6.13: Evolution of CXRS measurements at different time points during an ELM cycle averaged over ~ 60 ELMs: (a) T_i , (b) spectral radiance of the CX line, (c) toroidal rotation and (d) poloidal rotation. The labels ‘-2.2 ms’, ‘0.0 ms’ and ‘+2.2 ms’ denote the relative time to the closest ELM. The profiles originate from a time window of 700 ms in which the plasma was radially moved through the LOS of the edge CXRS diagnostics. The vertical dashed line in each subfigure indicates the separatrix position.

electron profiles observed at AUG [60].

Figure 6.14(a) shows the resulting E_r profiles. The radial electric field is the deepest shortly before the ELM (black profile), while during the ELM crash the profile decreases in the ETB by up to a factor of 3 (red dotted profile), consistent with DR measurements [79]. The collapse of E_r results in a reduction of the E_r shear across the whole ETB. The destruction of the E_r

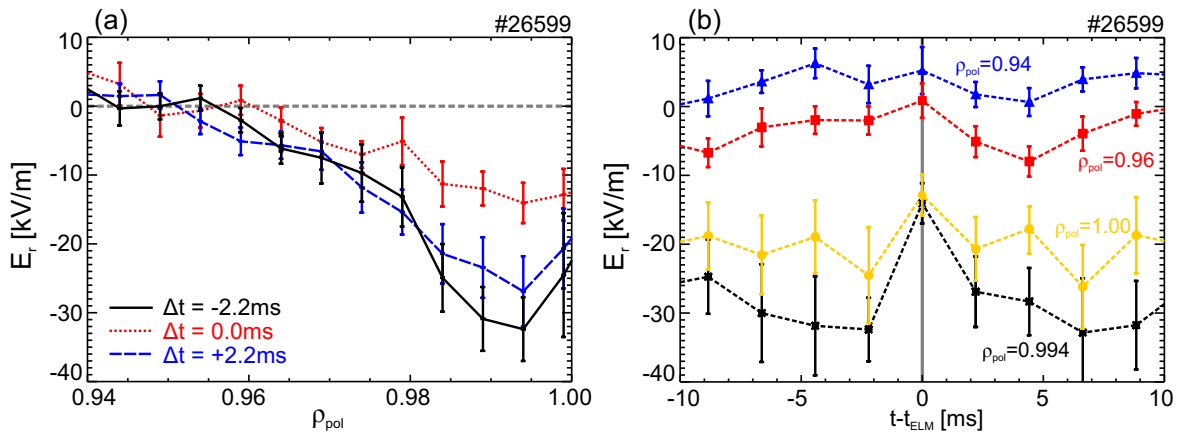


Figure 6.14: (a) Radial electric field profiles before (black), during (red) and after (blue) an ELM, (b) E_r at distinct radial positions during an ELM cycle.

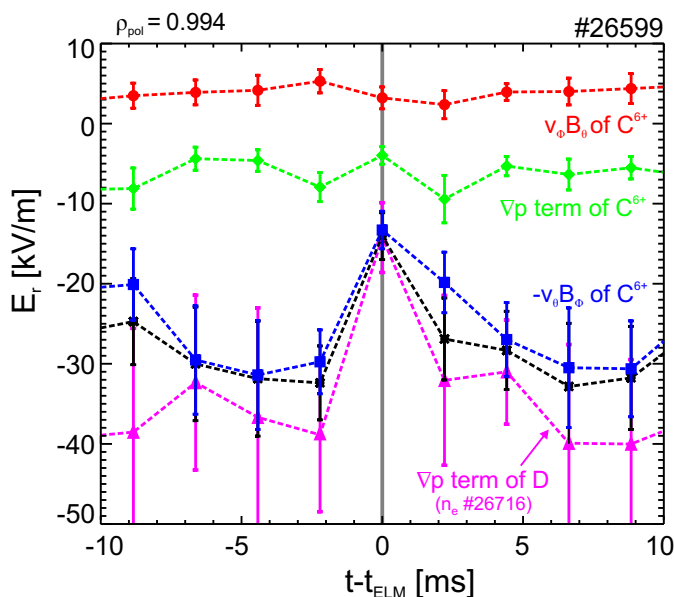


Figure 6.15: Individual impurity terms for the evaluation of E_r (red circles, green diamonds and blue squares) and main ion pressure gradient term (magenta triangles) at $\rho_{pol} = 0.994$ during an ELM cycle.

shear layer at the ELM crash has also been observed in MAST using fast CXRS measurements with a time resolution of $200 \mu s$ [150]. Shortly after the ELM (+2.2 ms, blue dashed profile in figure 6.14(a)) the profile recovers and the E_r well reforms, reaching its initial depth 4–6 ms after the ELM event (cf. figure 6.14(b)), consistent with time scales observed at DIII-D [149]. Figure 6.14(b) shows the temporal evolution of E_r at different radial locations. Further inside the plasma ($\rho_{pol} < 0.95$) E_r is almost not affected with only slight modifications during the ELM crash, while in the ETB the E_r well is strongly reduced. Note that the E_r well might even vanish for a brief time period that is too short to be detected by the diagnostics.

Figure 6.15 shows the contributions of the individual terms of the radial force balance equation to the E_r well during the ELM cycle. Throughout the entire ELM cycle the poloidal impurity rotation term is the dominant contribution for the evaluation of the E_r well. The temporal evolution of the main ion pressure gradient term is shown in magenta (triangles) in figure 6.15. The agreement in both the magnitude and evolution is remarkably good and shows that already ~ 2 ms after the ELM crash both the p_i gradient and the E_r well are recovering. It should be mentioned that the main ion pressure gradient term has been calculated using the n_e profile from an identical experiment (#26716), as the edge n_e measurements were not available for the considered discharge.

6.5 Effect of magnetic perturbations on the edge radial electric field

For the 2011 experimental campaign, the AUG tokamak was equipped with a set of in-vessel saddle coils which consisted of two rows of coils above and below the midplane [151]. Each row had four coils at different toroidal positions (see figure 6.16(a)). The coils marked in grey were installed additionally for the 2012 experimental campaign.

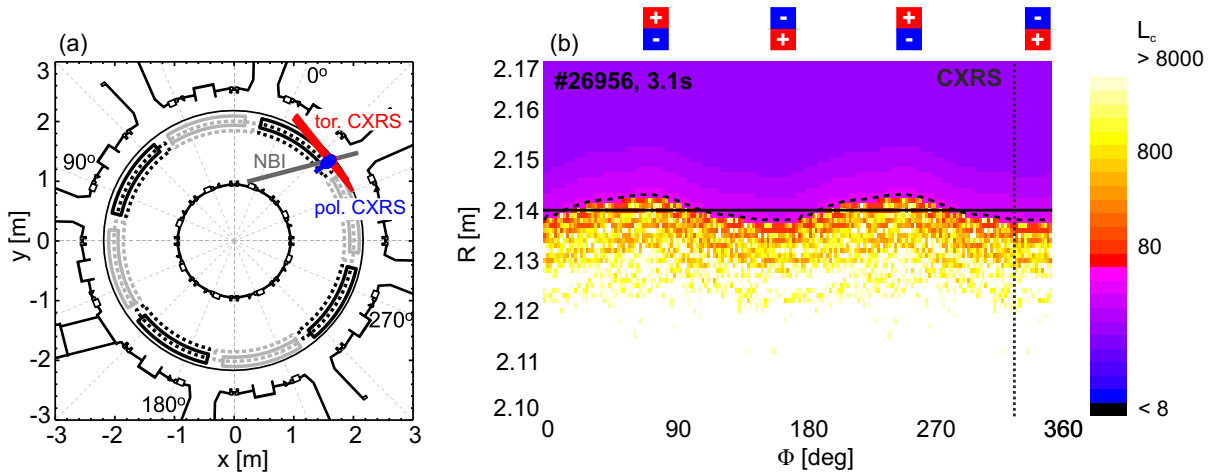


Figure 6.16: Magnetic perturbation coils at AUG: (a) toroidal cross-section of AUG indicating the position of the MP coils and the LOS of the edge CXRS diagnostics (since the 2012 experimental campaign the full set of MP coils is in operation, i.e. two rows with 8 MP coils each), (b) Poincaré plot in R - ϕ plane showing the connection length L_c to the low-field side target of field lines starting at $z = 0.03$ m, assuming that the total magnetic field corresponds to the sum of the magnetic field from the unperturbed equilibrium and the vacuum field of the MP coils. The vertical dashed line marks the position of the edge CXRS measurements. The horizontal solid line indicates the unperturbed separatrix position, while the dashed curve marks the perturbed separatrix position.

The coils were used to apply non-axisymmetric magnetic perturbations (MPs) to the plasma in order to suppress type-I ELMs. In H-mode plasmas with externally applied MPs (toroidal mode number $n = 2$) ELM mitigation was observed above a critical edge density [101], corresponding typically to a fractional Greenwald density of $n_{e,ped}/n_{GW} \sim 0.65$. Here, $n_{e,ped}$ is the pedestal electron density and n_{GW} the Greenwald density [152] defined as $n_{GW} = I_p/\pi a^2$. So far, ELM mitigation has been observed in plasmas with different shape, different heating mixes, different levels of heating power [153] and with MPs that are both resonant and non-resonant at the q_{95} surface [101] (q_{95} being the safety factor at the surface that encloses 95% of the poloidal magnetic flux). Resonance means that the MP is aligned with the local magnetic field lines.

The experiment presented here was carried out specifically to test if there is an observable effect on the E_r profile due to the MPs. The discharge was designed with four phases (see figure 6.17), the first one without MPs, followed by a phase with MPs but without ELM mitigation. In the third phase (MPs on) the density was increased and ELM mitigation was achieved and in the last phase, the MPs were switched off. The discharge was performed in H-mode with $B_\phi = -2.4$ T, $I_p = 1$ MA, NBI heating of 7.6 MW and ECRH ranging between 1.5 and 2.2 MW. The edge safety factor q_{95} ranged between 4.05 and 4.35 throughout the different phases of the discharge. The $n = 2$, odd configuration (odd corresponding to the opposite parity of upper and lower MP coils) was used.

Figure 6.16(b) shows the connection length L_c to the low-field side target of field lines which start on a horizontal plane at $z = 0.03$ m (corresponding to the z position of the edge CXRS measurements) and wind around the torus. These calculations are based on a 3D field line tracing code [154] which assumes that the total magnetic field is given by the sum of the mag-

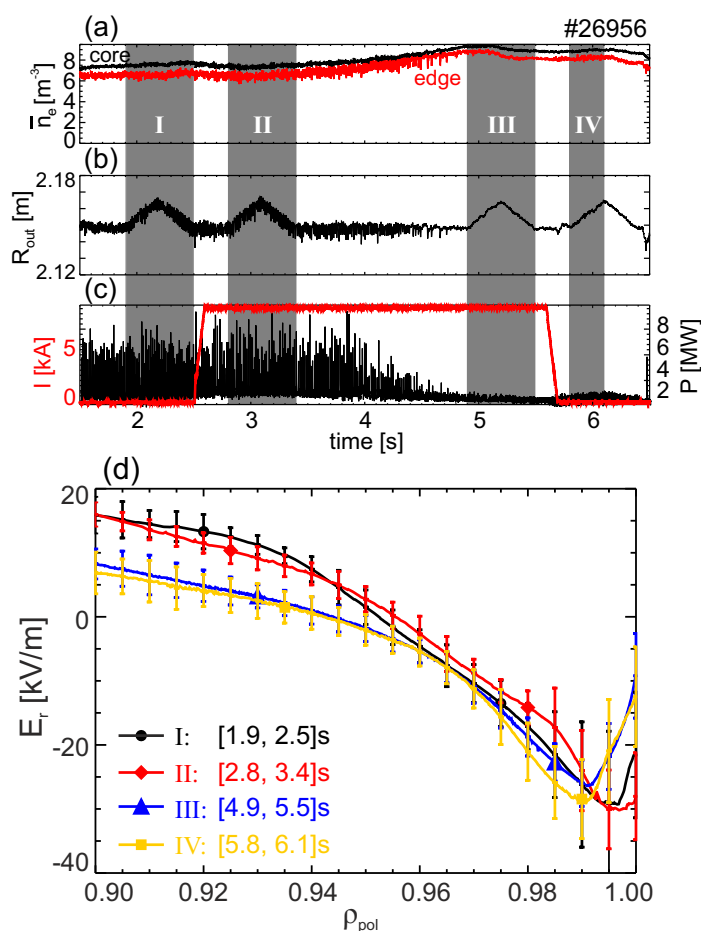


Figure 6.17: Time traces of MP scenario ($n = 2$): (a) Line-averaged density in the plasma core (black) and edge (red), (b) radial plasma position at outer midplane R_{out} , (c) ELM monitoring signal in the divertor (black) and current of MP coils (red), (d) radial electric field profiles corresponding to different phases during the discharge (marked in gray in (a)-(c)). No obvious effect on E_r is observed due to the MP coils.

netic field from the unperturbed equilibrium and the vacuum field of the MP coils [155]. The vertical dotted line represents the position of the edge CXRS measurements at $\phi = 333^\circ$. The horizontal line corresponds to the unperturbed separatrix position $R = 2.141$ m, while the dashed curve marks the position of the perturbed separatrix (i.e. when the magnetic perturbation coils are switched on) as calculated via field line tracing. The perturbed separatrix winds sinusoidally around the torus. At the z -position of the edge CXRS diagnostics the perturbed separatrix is radially shifted inwards by about 3 mm.

Figure 6.17(a) shows the time trace of the line-averaged electron density from a central LOS and an edge LOS of the interferometry system. The radial plasma position at the outer mid-plane (see figure 6.17(b)) was scanned several times to obtain detailed edge profiles in each phase. In figure 6.17(c) the current of the MP coils and an ELM-monitoring signal in the divertor are plotted. At a line-averaged edge density of $6.5 \times 10^{19} \text{ m}^{-3}$ the application of the MP coils has no effect on the ELMs. However, as soon as a critical edge density is achieved (cf. phase III) the type-I ELMs disappear. From the CXRS measurements in each radial sweep E_r profiles were obtained by measuring the B^{5+} CX line (see figure 6.17(d)). In general, the E_r profile does not exhibit any significant change due to the MPs. Moving from phase I to II and

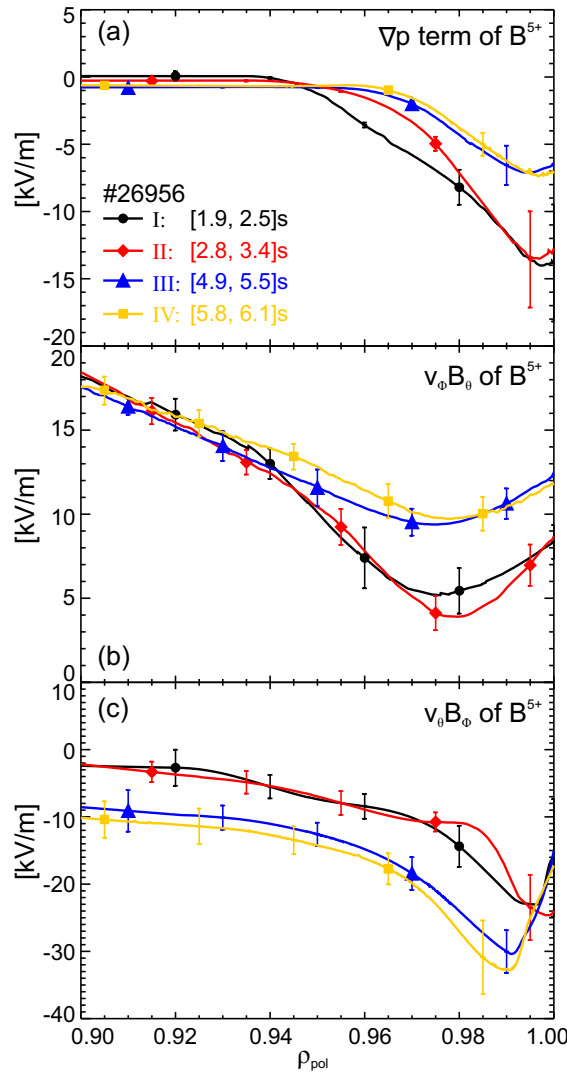


Figure 6.18: Individual impurity ion terms in the radial force balance of B^{5+} : (a) pressure gradient term, (b) toroidal rotation term and (c) poloidal rotation term. Note the different scales of panels (a)–(c).

switching on the MP coils has no effect on the ELMs and no change in E_r is observed. As the plasma density increases (moving from phase II to III) the type-I ELMs disappear. However, the E_r well (see blue curve of figure 6.17(d)) is not affected and stays constant also when the coils are switched off. Comparing the E_r profile of phases II and III, the minimum of the E_r well appears to be slightly shifted inwards. This shift corresponds to about 2 mm in real space and is just within the error bars. The radial shift might arise due to the 3D equilibrium induced by the MPs (as discussed in chapter 3.3). Towards the plasma core the radial electric field decreases by ~ 8 kV/m (at $\rho_{pol} = 0.9$). Note that this reduction is mainly attributed to the increase in the gas puff level and hence, plasma density as the changes are only observed when moving from phase II to phase III. In the last phase the density stays at the same level and the MP coils are switched off. Here, the type-I ELMs do not return, however, small high-frequency ELMs (~ 200 Hz) appear. Note that the radial electric field shows again no response. Figure 6.18 shows the individual impurity terms in the radial force balance of B^{5+} for the four different phases: (a) pressure gradient term, (b) toroidal rotation term and (c) poloidal rotation

term. Note the difference in scale when comparing the individual terms. The different impurity contributions for the evaluation of E_r show a similar behaviour, i.e. the MPs do not have a significant impact on the edge kinetic impurity profiles (compare phase I and II, or, phase III and IV), consistent with the observation of no changes in the kinetic electron pressure profiles in H-mode discharges with $n = 2$ MPs [102]. The biggest change on the kinetic impurity profiles is visible when moving from phase II to phase III and is attributed to the increased gas puff. At the same time the edge transport is changing since the type-I ELMs are suppressed (see figure 6.17(c)). The fact that in the ETB E_r is almost unchanged when moving from phase II to phase III suggests that the main ions set the radial electric field, while the impurities follow E_r and the impurity terms in the radial force balance redistribute according to the edge transport. These results suggest that in H-mode plasmas at high density the edge radial electric field is not affected by externally applied MPs in the $n = 2$ configuration. The fact that E_r remains unaffected may be explained by the shielding of the plasma, i.e. the MP is not fully penetrating into the pedestal. A similar indication was reported from DIII-D in H-mode plasmas with resonant MPs in the $n = 3$ configuration with odd parity and $q_{95} = 3.8$ [156]. Here, the E_r minimum remained unchanged while in the scrape-off layer E_r increased. The edge kinetic profiles, however, showed a response on the MPs and a reduction of the pressure gradient in the edge pedestal was observed. At TEXTOR an effect of resonant MPs on E_r was measured [157] resulting in a maximum increase of E_r by 9 kV/m with respect to a reference discharge without MPs. This was attributed to the ergodization of the plasma edge. At AUG a control experiment was conducted to test whether magnetic perturbations with a different toroidal mode number have an effect on E_r . Here, the full set of MP coils were em-

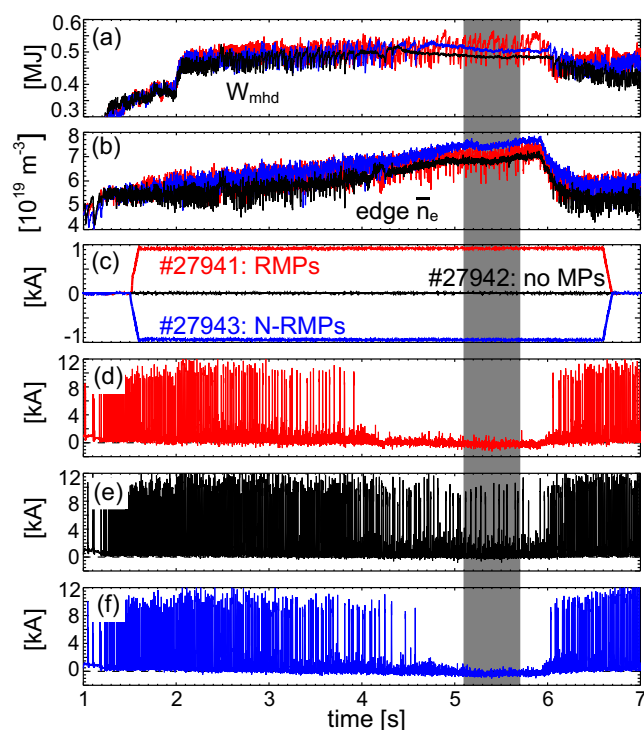


Figure 6.19: Time traces of scenario with $n = 1$ MPs: (a) Stored energy W_{mhd} , (b) line-averaged electron density, (c) current of the MP coils, (d)-(f) ELM monitor (thermo-currents in the outer divertor) for the three discharges: #27941 resonant case (RMPs), #27942 reference discharge without MPs and #27943 non-resonant case (N-RMPs).

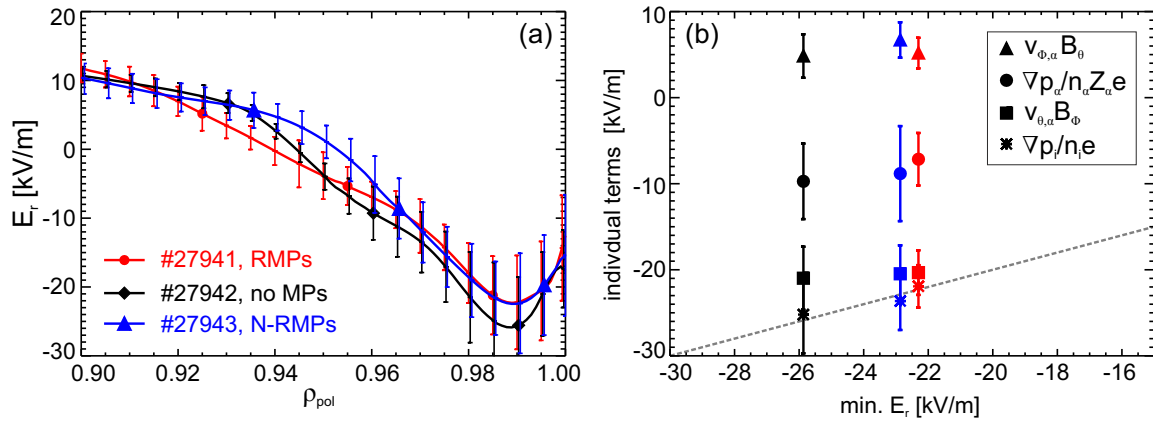


Figure 6.20: (a) E_r profiles in plasmas with $n = 1$ MPs, (b) individual impurity terms in the radial force balance of B^{5+} and main ion pressure gradient term (stars) versus minimum of E_r well. The values of the individual terms are taken at the minimum of E_r . For better clarity the uncertainties of the E_r well minimum are not plotted in subfigure (b).

ployed, i.e. all eight coils above and below the midplane (see figure 6.16(a)). Three discharges were carried out, one with $n = 1$ resonant MPs (RMP), one with non-resonant $n = 1$ MPs (N-RMP) and one reference discharge without MPs. The density was slowly ramped to identify the ELM mitigation threshold with MPs [158].

Figure 6.19 shows time traces of the (a) stored energy, (b) line-averaged electron density, (c) current of the MP coils and (d)–(f) an ELM-monitoring signal, i.e. thermo-currents in the outer divertor, for the three discharges. In the phase marked in grey in figure 6.19 a radial plasma sweep was included to provide detailed edge profiles. The E_r profiles are evaluated from measurements on the B^{5+} spectral line. Figure 6.20(a) shows the E_r profiles obtained in the three different discharges. The E_r well shows a slight reduction of ~ 4 kV/m when the MPs are switched on independent of their resonance. It may be noted that the difference is within the uncertainties, however, it is intriguing that the E_r well decreases in both cases compared to the reference discharge without MPs. Figure 6.20(b) shows the individual impurity terms in the radial force balance of B^{5+} at the radial position of the E_r minimum plotted against the minimum of the E_r well. The differences in the evaluation of E_r result mainly due to a change in the toroidal rotation term and in the pressure gradient term of B^{5+} , however, both changes are not really significant and are within the uncertainties. A comparison to the main ion pressure gradient term shows that E_r and $\nabla p_i / n_i e$ are coupled independent of the application of the MPs (cf. figure 6.20(b)). As the edge density is different for the resonant and non-resonant cases (see figure 6.19(b)), the ion pressure gradient ∇p_i should react differently as well. In the resonant case ∇p_i is lowered by about 15%, while in the non-resonant case ∇p_i is almost unchanged compared to the reference discharge without MPs. This is consistent with observations of the electron pressure gradient [159] which reacts similar to ∇p_i .

The results obtained in discharges with $n = 1$ MPs suggest that the MP may penetrate into the pedestal causing a reduction of the E_r well of ~ 4 kV/m. However, the uncertainties do not allow to unambiguously determine this effect. A reduction of the E_r well has also been observed in low density L-mode plasmas at AUG [160]. The fact that in H-mode the radial electric field and the main ion pressure gradient term match even in the presence of MPs underlines that E_r and the gradients in the main ion species are closely coupled.

Chapter 7

Comparison to neoclassical theory

In chapter 2 the theoretical background important to this thesis was presented and the simplest approximation of the radial electric field was derived. Neoclassical theory provides experimentally testable predictions for the poloidal rotation velocity and for the radial electric field E_r . In this chapter the validity of the neoclassical formulation of poloidal rotation velocities is studied for the conditions in the pedestal using the measurements from the new poloidal edge charge exchange recombination spectroscopy (CXRS) diagnostic.

7.1 Previous results from other tokamaks

To perform experimental tests against neoclassical theory [27] very accurate poloidal rotation measurements are required. The picture is quite puzzling as measurements on various devices have revealed different results: In internal transport barriers formed in enhanced reversed shear discharges at TFTR [123], in internal transport barriers at JET [161, 162] as well as in the core of H-mode and quiescent H-mode discharges at DIII-D [163] the neoclassical simulations deviated by an order of magnitude.

On all tokamaks the poloidal rotation was measured using active CXRS. At TFTR the poloidal rotation velocity was obtained using an inversion technique and up-down symmetric views to cancel the effect arising due to the energy dependent charge exchange (CX) cross-section [164, 123]. At JET [115] and DIII-D [163] corrections due to the CX cross-section and gyromotion effects (as described in chapter 4) were taken into account as their contribution was a significant fraction of the poloidal rotation velocity in the plasma core. Despite including these corrections the measurements were found to be almost an order of magnitude larger than the neoclassical prediction. At DIII-D the measurement was even found to be in the opposite direction to the neoclassical prediction across the whole profile.

Earlier DIII-D results [9] at the plasma edge showed that the poloidal rotation velocities of main ions and impurities are in qualitative agreement with neoclassical expectations as the directions were found to be consistent with the predictions. However, the magnitude of the simulated main ion poloidal rotation did not agree with the measured profile. The main ion poloidal flow was measured using CXRS on He^{2+} in helium plasmas and yielded poloidal rotation velocities of up to +40 km/s at the plasma edge (with the positive sign being in the ion diamagnetic drift direction). The conventional neoclassical calculations [35] predicted velocities in the range of +0–2 km/s. Comparison of the measured DIII-D data with neoclassical predictions including the orbit-squeezing effect [165], i.e. the ion banana widths are reduced

due to the gradient in the radial electric field [166], showed a fair agreement at the very edge of the plasma.

In JT-60U plasmas with internal transport barriers [167, 168], in improved H-modes at ASDEX Upgrade [22], in H-mode plasmas on Alcator C-Mod [133, 169], in L- and H-mode plasmas in the spherical tokamak MAST [170] as well as in experiments performed at NSTX [113] the poloidal rotation measurements agreed with neoclassical theory within the experimental uncertainties. So far, these measurements have been performed on impurities and in the core of the plasma (except for the work of Marr *et al.* [133] which was focussed at the plasma edge).

To shed more light on this puzzling picture and on the physics determining the poloidal flow in a tokamak plasma, the edge poloidal rotation measurements obtained during this thesis are compared to neoclassical calculations. The results discussed in chapter 6 show that the radial electric field E_r is well described by the main ion pressure gradient term $\nabla p_i/en_i$. As the toroidal rotation is observed to be small at the plasma edge, the matching between E_r and $\nabla p_i/en_i$ indicates that the poloidal rotation velocity of the main ions should be neoclassical. As discussed in chapter 2 neoclassical theory provides experimentally testable predictions of the poloidal flows. The main ion poloidal rotation is strongly dependent on the ion temperature gradient scale length, while the poloidal impurity rotation depends on both the main ion temperature and pressure gradient scale lengths. The experimental tests against neoclassical theory of both main ions and impurities are presented in the following.

7.2 Experimental tests of poloidal flows against neoclassical theory

The measurements from the new poloidal edge CXRS diagnostic at AUG enable a detailed comparison of neoclassical predictions and experimental data in the edge pedestal. As presented in chapter 4 the measurements are purely poloidal and the atomic physics effects in the measured CX spectra are negligible. To compare the measurements with neoclassical simulations the numerical code NEOART [38] is used. NEOART is based on the calculation of collisional transport coefficients for a given number of impurities and includes collisions between all species. The transport coefficients represent the sum of a classical, a Pfirsch-Schlüter and a banana plateau term [38, 171]. The code solves a set of linear coupled equations for the parallel velocities in an arbitrary toroidally symmetric geometry and calculates neoclassical transport parameters for all collisionality regimes [172]. A reduced charge state method [38] is applied for all contributing parts in order to reduce computational time required for these calculations. For the simulations the measured kinetic profiles are used as input and it is assumed that all ions have the same temperature T_i , i.e. $T_D = T_\alpha = T_i$ (D being deuterium and α the impurity species).

A complementary approach of comparing the experimental data to neoclassical predictions is provided by the neoclassical numerical codes NEO [45] and HAGIS [46]. Both NEO and HAGIS employ the δf method in which the distribution function is split into $f = f_0 + \delta f$ where f_0 is the equilibrium distribution function and δf the perturbed part.

The numerical code NEO [45] is based on an Eulerian numerical discretization scheme and solves the first-order drift kinetic equation. It uses a δf expansion of the fundamental drift-kinetic Poisson equations [173] and a first-principles approach to calculate the neoclassical

transport coefficients directly from the solution of the distribution function. NEO includes self-consistent coupling of electrons and multiple ion species, fast toroidal rotation and the calculation of the electrostatic potential through coupling with the Poisson equation.

The drift-kinetic, perturbative code HAGIS [46] was developed to study the interaction between Alfvén eigenmodes and fast particles. An extension of the original HAGIS code with a Monte-Carlo pitch angle collision model [174] enables the calculation of neoclassical transport where the unperturbed distribution function f_0 is a Maxwellian with constant density and temperature on a flux surface. The perturbed part of the distribution function, δf , is represented by marker particles which are followed along their orbits and the collisions are modelled by a Monte-Carlo procedure. The extended version of HAGIS models a three-species plasma (electrons, main ions and one trace impurity species) and includes the effects due to finite orbit sizes.

7.2.1 Poloidal main ion rotation velocity

Helium plasmas provide the opportunity to obtain information on the main ion species and a direct measurement of the main ion poloidal rotation velocity $v_{\theta,i}$. In these plasmas, the main ion poloidal flow was obtained from CXRS on He^{2+} ($n = 4 \rightarrow 3$). The data were measured in the same H-mode discharge as presented in section 6.1. Figure 7.1(a) shows the measured $v_{\theta,i}$ profile in black along with a spline fit in blue. The measured values are negative, i.e. in the electron diamagnetic direction. The corrections due to the atomic physics effects [109, 112] are found to be small: the maximum apparent velocity is 0.2 km/s which is well within the experimental uncertainties. The corrections have been calculated using a vacuum radiative lifetime of 2 ns for the $\text{He}^{2+} + \text{D}^0 \rightarrow \text{He}^{1+} + \text{D}^+$ transition. This value has been determined from the Einstein coefficients calculated using the Cowan code [116], as provided by the Atomic Data Analysis Structure [117]. The main ion poloidal rotation is found to be small and is in agreement with the neoclassical prediction calculated with the code NEOART [38] shown in red. The main ion poloidal flow is predominantly driven by the ion temperature gradient scale length. The dashed lines in red in figure 7.1 show the effect of a radial shift of ± 2 mm between electron and ion profiles which are used as input for the simulations.

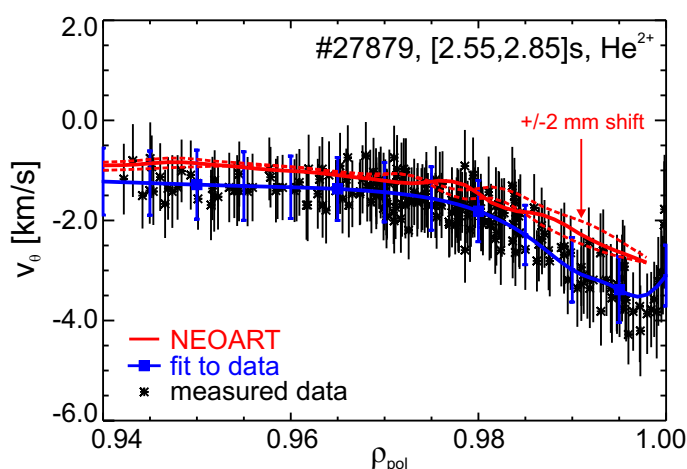


Figure 7.1: Main ion poloidal rotation velocity measured in a helium plasma, the fit to the measured data is shown in blue, while the neoclassical prediction calculated with NEOART is shown in red.

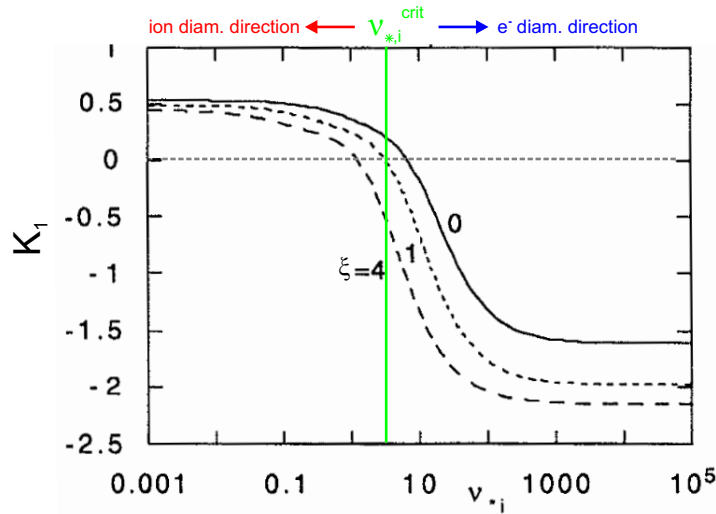


Figure 7.2: Neoclassical coefficient K_1 , which enters the neoclassical prediction of the poloidal main ion flow (see equation 2.33), plotted as a function of the ion collisionality for different impurity strength parameters ξ (adapted from [35]). At a critical value of $\nu_{*,i}$, K_1 changes sign and thus, the poloidal rotation flips from the ion diamagnetic to the electron diamagnetic drift direction.

In this discharge the ion collisionality $\nu_{*,i}$, as defined in section 2.1.2, at the pedestal top ($\rho_{pol} = 0.97$) is ~ 12 (see also black curve in figure 7.8(a)), which is two orders of magnitude higher compared to the helium plasmas performed at DIII-D [9]. In the DIII-D experiments the ion collisionality varied from 0.1 to 0.3 [9]. This explains the opposite direction of the main ion poloidal rotation velocity measured at AUG and DIII-D. At DIII-D $v_{\theta,i}$ was positive, i.e. in the ion diamagnetic drift direction, and reached values of up to 40 km/s in the plasma edge. The conventional neoclassical approach [35] predicts that $v_{\theta,i}$ is strongly dependent on the neoclassical coefficient K_1 (see equation (2.33)) which itself depends on the edge ion parameters. Depending on the ion collisionality the main ion poloidal rotation can be in the electron or in the ion diamagnetic drift direction. The poloidal flow can also be close to zero at a certain critical value of the collisionality or, expressed with the parameter K_1 [35], where $K_1(\nu_{*,i}) = 0$ (for details on the derivation of K_1 see ref. [35]).

Figure 7.2 shows the neoclassical coefficient K_1 as a function of the ion collisionality for an inverse aspect ratio $\epsilon = 0.3$ and different impurity strength parameters ξ , defined as $\xi = n_\alpha Z_\alpha^2 / n_i Z_i^2$ where n and Z denote the density and the charge state of the impurity α and the main ion i , respectively. Both AUG and DIII-D have an inverse aspect ratio of 0.3. At AUG, the impurity strength parameter ξ is typically below or around 1. It should be noted that K_1 varies depending on the discharge parameters and the zero-crossing, i.e. the critical value of $\nu_{*,i}$, might change depending on the experiment. Figure 7.2 shows that depending on the collisionality regime, K_1 may change sign and thus, the main ion poloidal flow can be either in the ion or in the electron diamagnetic drift direction. Due to the different collisionalities obtained in the helium plasmas performed at AUG and DIII-D, it is not surprising that $v_{\theta,i}$ is in the opposite direction. However, the measured profile at DIII-D exhibited peak velocities of up to 40 km/s at the plasma edge and they were far off from the neoclassical prediction ($v_{\theta,i} \approx 0-2$ km/s). Extending the neoclassical model with the orbit-squeezing effect [165] increased the neoclassical prediction to the same order of magnitude as the measurement, at least at the very edge of the plasma. The orbit-squeezing effect can become important only in the

deep banana regime as here the particles complete several banana orbits before colliding. At AUG the operation of low density He discharges, which facilitate access to the low collisionality regime, is limited due to the pumping system and the inventory in the all W wall. In addition, helium plasmas are not a standard operation at AUG and thus, the experimental time to perform main ion flow measurements is limited. However, the low collisionality regime was simulated using test input profiles to quantify the effect of the collisionality on the poloidal rotation profile (see section 7.3).

7.2.2 Measured poloidal impurity flows in comparison with neoclassical simulations

The comparative analysis has been extended to several different impurity species and to different neoclassical codes including NEO [45] and HAGIS [46].

In an H-mode discharge performed in deuterium the poloidal impurity rotation velocity $v_{\theta,\alpha}$ was measured on the N^{7+} ($n = 9 \rightarrow 8$) spectral line and compared to conventional neoclassical predictions based on [35] (see also section 2.2.2). Figure 7.3 shows the spline fit to the measured poloidal rotation data in black and the neoclassical prediction using the analytic model [35] in blue (dashed line). In addition, the simulated profiles obtained with the neoclassical codes NEOART, NEO and HAGIS are shown in red (solid line), magenta (crosses) and green (dashed dotted line), respectively. All models agree quite well within the uncertainties and are consistent with the measured profile. It should be noted that at the very plasma edge the gradient scale length approaches that of the poloidal ion gyroradius, thus breaking the order assumed in the theory and the neoclassical approximation is less valid in this region.

Since the toroidal flow is small at the plasma edge, the agreement between the measurement and the neoclassical simulations also indicates that the edge radial electric field E_r behaves as expected from neoclassical theory. Figure 7.3(b) shows the E_r profile derived from the CXRS measurements in black and an estimate of the main ion pressure gradient term $\nabla p_i / en_i$ in grey (dotted line). The profile shown in blue has been calculated using the Hinton-Hazeltine

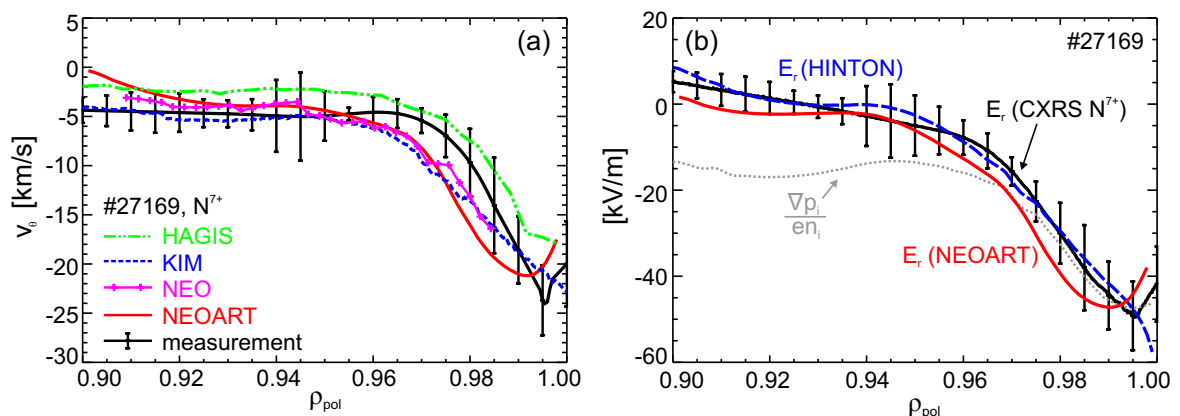


Figure 7.3: (a) Impurity poloidal rotation velocity measured on N^{7+} in a D plasma, along with the conventional neoclassical prediction [35] in blue (dotted line) and the simulated profile using NEOART (red, solid line), NEO (magenta, crosses) and HAGIS (green, dashed dotted line). (b) E_r profile as measured with CXRS in black, estimate of main ion pressure gradient term in grey (dotted line), E_r calculated using the Hinton-Hazeltine formulation [27] in blue (dashed line) and from NEOART in red (solid line).

formulation [27], while the profile in red shows the simulated profile using NEOART. At the plasma edge the poloidal rotation velocity is at neoclassical levels and, in combination with the observed small toroidal rotation velocities, E_r is well described by the neoclassical prediction. The mechanism responsible for damping the toroidal rotation velocity to small values at the plasma edge is not clear [42] and requires a more detailed understanding of the toroidal momentum transport in the edge pedestal region.

A basic understanding of the relation between E_r and $\nabla p_i/en_i$ may be demonstrated by the following qualitative picture: In the pedestal the radial electric field acts like a potential barrier which confines the thermal ions, thus, preventing the ions to get lost through the separatrix. The thermal energy of the ions corresponds to the potential energy associated with the potential drop to the separatrix. Figure 7.4 shows the potential energy $\Delta\Phi$ related to the electrostatic potential in black and in red the thermal energy of the ions, $U_{th} = k_B T_i$, where k_B is the Boltzmann constant and T_i the ion temperature as measured with CXRS. For the calculation of $\Delta\Phi = \Phi - \Phi_0$ the radial electric field is integrated from the separatrix to $\rho_{pol} = 0.9$ and Φ_0 is arbitrarily chosen at the separatrix. The matching of the two curves near the pedestal top (at $\rho_{pol} \approx 0.97$) indicates that, using this simplified picture, the thermal ions are confined by the electric field.

A possible explanation for the build-up of the potential barrier might be the hot tail of the distribution function of the ions. The ions originating from the hotter part of the distribution function can get lost while completing their banana orbit, which leads locally to a lower net charge and, therefore, to a potential difference. This is substantiated by calculations made with HAGIS [175] (see blue dashed curve in figure 7.4), in which full orbit effects and the magnetic field configuration of AUG were taken into account. Only ions were followed, starting with initially given profiles and the electric field which is computed via Poisson's law using the charge deficit arising from the radial loss flow of ions. This is equivalent to assuming that the electrons are much better confined. The ion losses are practically stopped, once the potential has grown to a sufficiently high value. In reality, the losses will be continuous, at a rate compatible with the electron losses, but as this loss rate will determine only the (small) fraction of ions capable to overcome the potential barrier, the latter (for an approximately Maxwellian distribution) will depend only logarithmically on the amount of these losses. The scale length

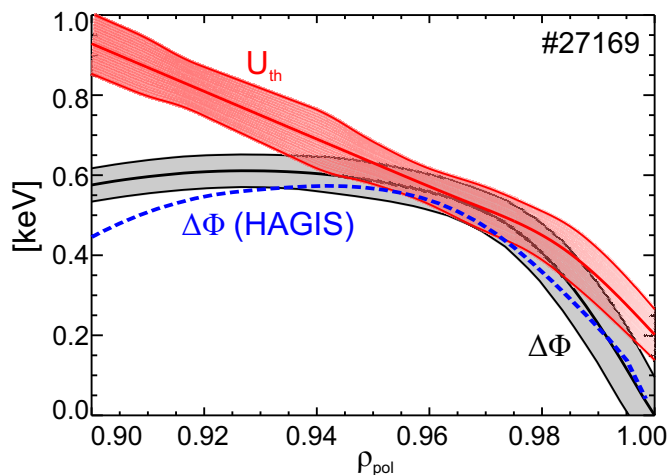


Figure 7.4: Potential energy associated with the potential difference between the separatrix and the pedestal in black and thermal ion energy in red, simulated potential drop using HAGIS [175] in blue (dashed line).

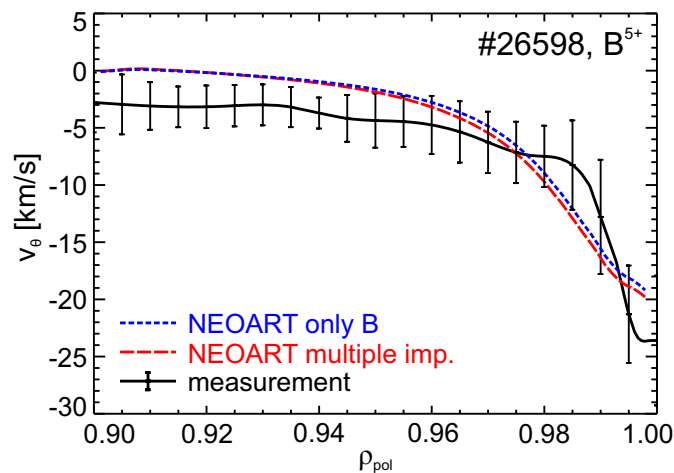


Figure 7.5: Effect of including multiple impurity species in the neoclassical simulation: fit to measured $v_{\theta,\alpha}$ profile of B^{5+} in black, neoclassical predictions using only boron as impurity species in blue and using boron, carbon, oxygen and tungsten in red.

of the potential drop corresponds approximately to the ion banana width. For a thermal ion, the banana width is ~ 7 mm at the pedestal top.

For a further validation of the experimental tests against neoclassical theory different impurity species, including He^{2+} , B^{5+} and C^{6+} measured in D plasmas, have been analyzed. Figure 7.5 shows the measured poloidal rotation velocity of B^{5+} in comparison with the neoclassical prediction calculated with NEOART. Here, the effect of including multiple impurity species is shown. For the simulated profile shown in blue a three-species plasma was assumed, i.e. electrons, deuterium and boron. The boron concentration (0.5 % at the pedestal top), which is used as input, is taken from the CXRS measurement. The neoclassical prediction shown in red includes boron, carbon, oxygen and tungsten as impurity species. Here, the carbon concentration was measured in a subsequent discharge using CXRS (0.6 % at the pedestal top), the tungsten concentration is measured by passive VUV (vacuum ultraviolet) spectroscopy and is usually of the order 0.01 ‰, while the oxygen concentration, measured by means of X-ray spectroscopy, is of the order 0.1–0.3 % in H-mode discharges. The inclusion of multiple impurity species, which is usually the case in the experiment, has only small effects on the poloidal rotation profile of boron and leads to an increase of 1 km/s in the edge transport barrier.

Figure 7.6 shows the minimum of the measured poloidal rotation velocity plotted against the minimum of the simulated profile of both impurity ions (black squares) and main ions (red circles) as measured in helium plasmas. In the H-mode edge pedestal both the sign and the magnitude of the neoclassical poloidal rotation are consistent with the measurement. Hence, $v_{\theta,\alpha}$ is mainly given by the main ion temperature and pressure gradient scale lengths, while the contribution from the impurity pressure gradient scale length is small as it is multiplied by Z_i/Z_α (see section 2.2.2).

Since the neoclassical poloidal rotation velocity is proportional to the toroidal magnetic field B_ϕ , the direction of the poloidal flow should change sign when B_ϕ is reversed. If the poloidal magnetic field B_θ is flipped the direction should not be affected [35]. The poloidal impurity ion rotation has been measured in the reversed I_p/B_ϕ configuration of AUG to verify whether or not the measurement is consistent with the neoclassical prediction. The data has been obtained in an H-mode discharge with B_ϕ on-axis of +2.4 T, $I_p = -900$ kA, 1.3 MW ECRH, 5 MW NBI heating and a central line-averaged density of $6 \times 10^{19} \text{ m}^{-3}$. The CXRS measurements

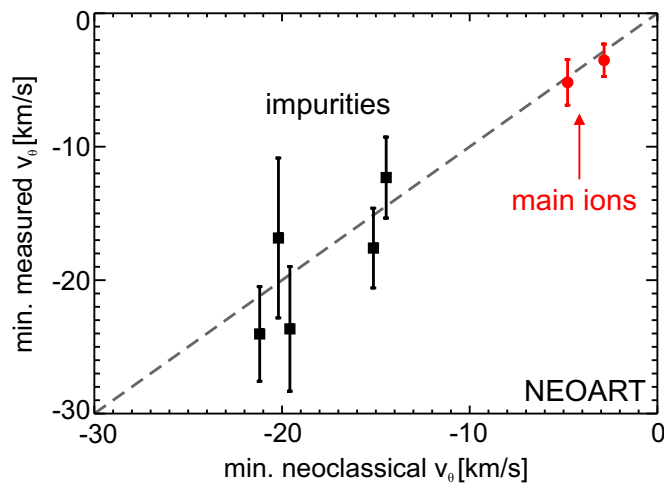


Figure 7.6: Minimum of measured poloidal rotation velocity versus minimum of neoclassical prediction.

were obtained on B^{5+} . In the reversed I_p/B_ϕ configuration positive values of $v_{\theta,\alpha}$ are in the electron diamagnetic drift direction. Figure 7.7 shows the measured data in black along with a spline fit in blue and the neoclassical prediction calculated with NEOART in red. The effect of a radial shift of ± 2 mm between electron and ion measurements are marked by dashed lines. Here the effect is slightly larger than it was for the main ion measurements (see figure 7.1) since the neoclassical poloidal impurity rotation depends on the local gradients of both the ion pressure and the ion temperature profiles.

The measurements show a hill-like structure at the plasma edge reaching values of up to ~ 20 km/s (cf. figure 7.7). In the ETB the poloidal rotation velocity behaves as expected from neoclassical theory and the sign and the magnitude are in remarkably good agreement with the experimental data. Further inwards ($\rho_{pol} < 0.94$) the measurements exhibit negative values for $v_{\theta,\alpha}$ (i.e. in the ion diamagnetic direction) while the simulation predicts positive values, though very close to zero. Note, however, that the measured value is ~ 1 km/s and including the uncertainty due to the wavelength calibration the measurement is consistent with the neoclassical prediction. The simulated profile exhibits a wider hill and in the region $0.95 < \rho_{pol} < 0.97$ the

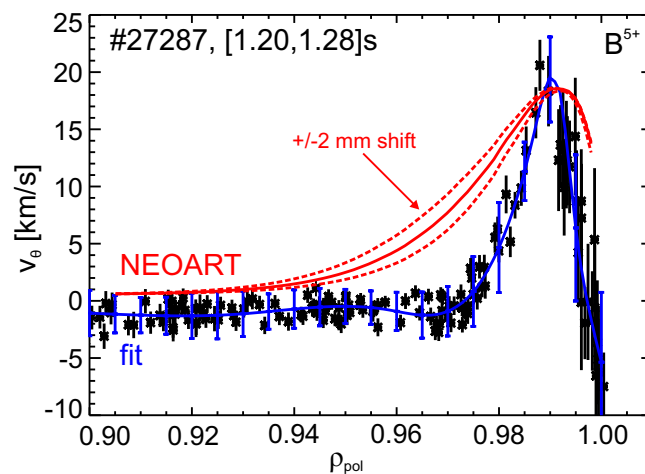


Figure 7.7: Poloidal rotation velocity of B^{5+} measured in the reversed I_p/B_ϕ configuration and comparison to neoclassical prediction.

measurements show a damping of $v_{\theta,\alpha}$ of the order ~ 5 km/s. Here, other mechanisms could affect the poloidal rotation velocity. If the parallel flow is reduced compared to the neoclassical value then the poloidal rotation may be affected by the ion diamagnetic velocity [165], which might be the case in the region $0.95 < \rho_{pol} < 0.97$. A mechanism which can reduce the parallel flow is for example radial diffusion of parallel momentum due to viscosity [165]. In addition, a toroidal torque (due to the NBI) could play a role and diminish the poloidal rotation velocity (i.e. the contribution is in the ion diamagnetic drift direction) as this term in the momentum balance equation does not change sign when reversing I_p and B_ϕ . However, it is not clear which mechanism is responsible for the damping of $v_{\theta,\alpha}$ in this region.

7.3 Simulation of low collisionality plasmas

Different test cases have been performed using the code NEOART to study the effect of collisionality on the poloidal rotation. The low collisionality regime has been approached by scaling the electron density and the ion and electron temperature, which are used as input profiles.

Figure 7.8(a) shows the radial profile of the main ion collisionality (here He). The Pfirsch-Schlüter limit (PS limit) is at $\nu_* \approx 7$, while the banana limit is at $\nu_* = 1$. In the real experiment, as presented in section 7.2.1, the main ions were deep in the Pfirsch-Schlüter regime (black curve in figure 7.8(a)). The density and temperatures are scaled such that the pressure remains constant. Using a scaling factor of 2 results in the ion collisionality being in the intermediate plateau regime (see red curve in figure 7.8(a)). The ion collisionality crosses the banana limit when dividing the electron density by a factor of 3 and scaling the temperatures correspondingly (cf. blue curve). The ions are deep in the banana regime when using a scaling factor of 4 (cf. green curve). Figure 7.8(b) shows the effect of reducing the ion collisionality on the main ion poloidal rotation. For lower collisionalities the main ion poloidal flow approaches zero and at a critical value of the collisionality v_θ changes sign and is in the opposite direction, i.e. in the ion diamagnetic drift direction (see green curve in figure 7.8(b)).

This analysis has been extended to study the effect on impurity ions. In general, the impurities are in the high collisionality regime at the plasma edge. Figure 7.9(a) shows the collisionality

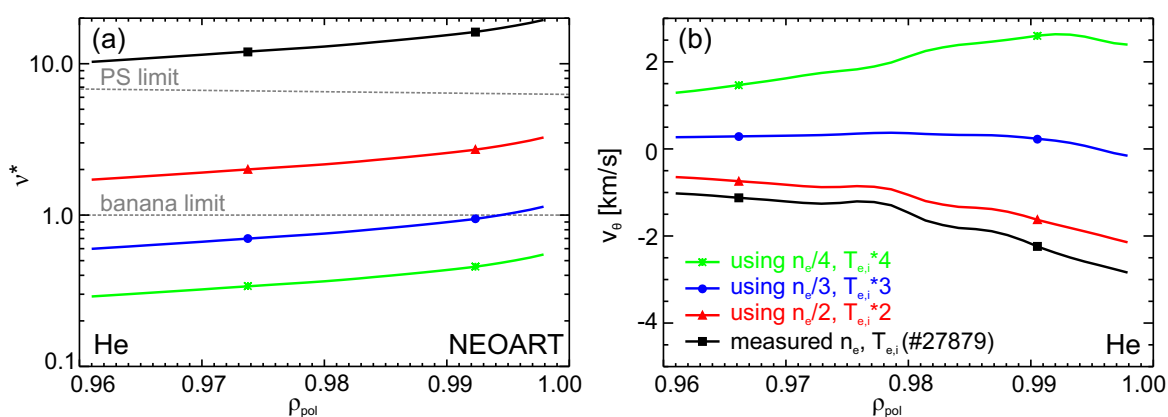


Figure 7.8: Simulation of main ions in the low-collisionality regime: (a) collisionality profile ν_* and (b) main ion poloidal rotation velocity v_θ . At a certain ν_* the poloidal rotation flips sign and is in the ion diamagnetic direction (positive v_θ).

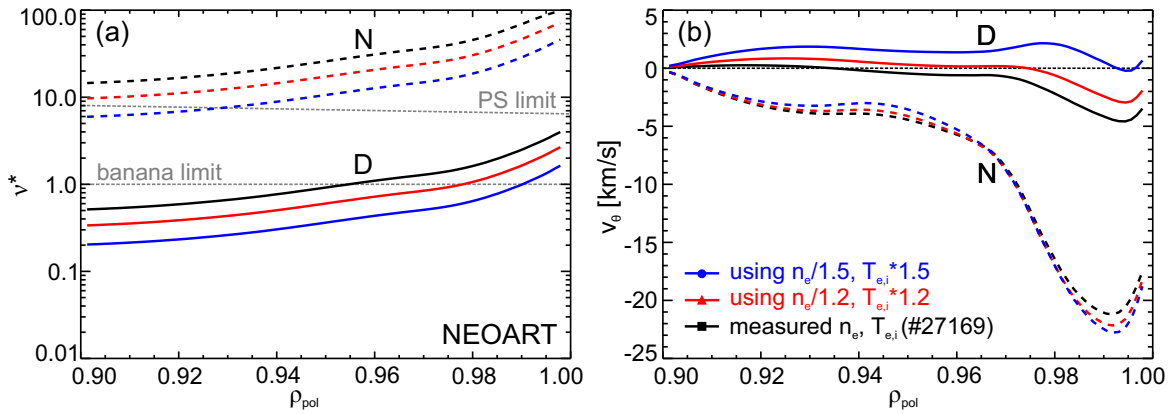


Figure 7.9: Simulation of nitrogen and deuterium poloidal rotation velocity in the low-collisionality regime: (a) collisionality and (b) poloidal rotation velocity.

for the main ions (here D, solid lines) and for the impurity species N (dashed lines). Due to the N_2 seeding, in the real experiment the main ions were in the banana regime further inwards and in the plateau regime at the plasma edge (cf. black solid line in figure 7.9(a)). Reducing the electron density and increasing the temperatures by a factor of 1.2 and 1.5, thus lowering the collisionality, leads to a decrease of the poloidal main ion flow (see figure 7.9(b)). The impurity concentrations remained unchanged and, therefore, the friction between impurities and main ions is increased. At a certain threshold of the main ion collisionality the poloidal main ion flow flips sign, while the impurities stay in the Pfirsch-Schlüter regime and the poloidal impurity rotation remains in the electron diamagnetic drift direction. Note that the poloidal impurity rotation is almost unchanged. Since the neoclassical poloidal impurity rotation depends mainly on the ion pressure and ion temperature gradients (see equation (2.34)), $v_{\theta,\alpha}$ is expected to show only little variations as the pressure is kept constant when scanning the collisionality in the calculations.

These simulations show that in the banana regime the poloidal rotation velocity of the main ions should change sign and, therefore, pointing into the ion diamagnetic drift direction. Measurements in the low collisionality regime would enable the experimental test of the poloidal main ion rotation against neoclassical theory. In particular, a variation of the collisionality could help to identify the critical value of ν_* at which the poloidal rotation flips sign.

Chapter 8

Summary and Discussion

This thesis contributes to the study and characterization of the radial electric field at the edge of tokamak plasmas. The understanding of the physics relevant to the edge of an H-mode fusion plasma is of crucial importance as steep gradients drive ion and impurity flows and the height of the pressure pedestal determines the boundary conditions for the performance in the plasma core. The underlying reason for the formation of the edge transport barrier (ETB) is believed to be the existence of a sheared plasma flow perpendicular to the magnetic field caused by a local radial electric field E_r .

The new edge charge exchange recombination spectroscopy (CXRS) diagnostics installed at ASDEX Upgrade (AUG) enabled the determination of E_r from the radial force balance equation. Using these measurements the connections between E_r and the ETB have been analyzed. In this final chapter the work performed in this thesis is summarized and the main findings are discussed. Possible directions for future work are outlined.

8.1 Summary and conclusions

The research performed in this thesis is based on active charge exchange recombination spectroscopy (CXRS), which provides temporally and radially resolved measurements of the ion temperature, density and velocity from the analysis of spectroscopic emission in the visible range. During this work the pre-existing toroidal edge CXRS diagnostic was upgraded with a new spectrometer and extended with a poloidal system, which was designed, installed and operated at the AUG tokamak. The new diagnostic enables high temporally (2 ms) and radially resolved (5 mm) measurements of the poloidal impurity rotation velocity and thus, provides the missing measurements for deriving the radial electric field E_r from the radial force balance equation. In addition, the combination of poloidal and toroidal views allows the determination of full plasma rotation profiles both perpendicular and parallel to the magnetic field.

In H-mode the poloidal impurity rotation velocity is very low towards the plasma core, while inside the ETB a strongly sheared rotation in the electron diamagnetic drift direction is observed. The toroidal rotation is co-current and exhibits a dip located near the pedestal top. The ion temperature T_i and impurity density n_α profile form a clear H-mode pedestal. Both T_i and n_α measured with both edge CXRS diagnostics are in excellent agreement and are consistent with the core toroidal CXRS measurements.

The E_r profile has been derived from charge exchange (CX) spectra measured on different impurity species including He^{2+} , B^{5+} , C^{6+} and Ne^{10+} . The resulting E_r profiles are found to

be identical within the uncertainties regardless of the impurity species used for the analysis. This demonstrates the validity of the diagnostic technique and provides a consistency check of the evaluation of E_r . In the present work, the localization of the E_r dip is of unprecedentedly high quality and has small uncertainties (2–3 mm) due to two aspects: First, the measurements are fixed in real space and have a resolution between 3 and 5 mm. Secondly, the T_i profile is part of the CXRS measurements and is therefore rigidly aligned to the E_r profile. The relative alignment of E_r to the electron profiles and the separatrix position is following an established scheme that makes use of the unique edge diagnostic capabilities available at the AUG tokamak. As a result, all E_r profiles are reproducibly aligned.

Using the measurements obtained during this thesis the questions raised in chapter 1 can now be answered:

- **What is the structure of E_r in the H-mode edge transport barrier? How is E_r characterized with respect to the edge kinetic profiles?**

In the ETB the radial electric field exhibits a deep, negative E_r well with the minimum localized close to the separatrix ($\rho_{pol} > 0.99$). The width of the E_r well shows little variation and is on average 1.2 cm.

In the radial force balance of impurity ions the poloidal rotation contribution yields the dominant term in the evaluation of E_r at the plasma edge. For the main ions, the E_r minimum coincides with the maximum pressure gradient term $\nabla p_i / en_i$ supporting that the E_r well is created by the main ion species. An estimate of the perpendicular deuterium velocity has been evaluated by comparing the main ion pressure gradient term and the E_r profile derived from CXRS. For $\rho_{pol} > 0.95$, i.e. the edge pedestal, the results suggest that the perpendicular main ion flow is close to zero with uncertainties less than 5 km/s. This is confirmed by direct measurements of the main ion temperature, density and rotation velocities in helium plasmas, which show that at the plasma edge E_r is mainly determined by the pressure gradient term of the main ions. This relationship requires in particular that the toroidal ion rotation velocity, which is determined by the toroidal momentum transport, is balanced by the poloidal rotation velocity. The poloidal main ion rotation is observed to be neoclassical and is, therefore, a small contribution to E_r . However, it is unclear which mechanism in the plasma edge is responsible for damping the toroidal rotation to small values. The possible drive (or damping) of the toroidal flow in the edge pedestal is still under investigation.

The fact that the perpendicular ion fluid velocity is almost zero at the plasma edge demonstrates that the $\mathbf{E} \times \mathbf{B}$ velocity and the ion diamagnetic fluid drift are in balance. The perpendicular electron flow velocity is evaluated from the measured E_r profile and the measured electron density and temperature profiles. Combining all measurements of the edge kinetic profiles provides experimental evidence that perpendicular to the magnetic field the ions are at rest in the lab frame while the electrons move with a speed that is approximately twice the electron diamagnetic drift velocity. This is also consistent with $\nabla p = \mathbf{j} \times \mathbf{B}$, i.e. to zeroth order a current \mathbf{j} perpendicular to the magnetic field balances with the pressure force. Since the main ion fluid velocity is almost zero, the electrons have to speed up to fulfill this condition.

The maximum in the E_r shearing rate coincides with the steepest ion pressure gradient ∇p_i and lies inside the position of the minimum of the E_r well. This suggests that the negative shear region is the important region for turbulence reduction within the $\mathbf{E} \times \mathbf{B}$ shear model.

- **What is the behaviour of E_r in different confinement regimes?**

To answer this question, the E_r profile has been investigated in L-, I- and H-mode plasmas. In L-mode, E_r is small in magnitude and exhibits little shear in contrast to the H-mode regime in which a strongly sheared negative E_r is observed in the ETB. Towards the plasma core, the absolute magnitude of E_r decreases and E_r changes sign. In the I-mode regime the minimum of E_r is intermediate between L- and H-mode.

The E_r minimum has been studied as a function of ion temperature, density and pressure at the pedestal top by combining the data measured in all confinement regimes. The depth of the E_r well, or the magnitude of the E_r shear respectively, shows a clear correlation with the ion pressure at the pedestal top, in keeping with the main ion pressure gradient term being the dominant contribution to E_r .

- **Are the impurity density, temperature and flows forming an equilibrium within a flux surface? Is the electrostatic potential constant along the flux surface?**

The installation of novel flow measurements at the inboard midplane of AUG, which are based on CXRS at a deuterium gas puff, enabled the study of possible asymmetries on a flux surface. The comparison of the high-field (HFS) and low-field side (LFS) profiles requires the alignment of the CXRS measurements and is based on the assumption of a constant ion temperature on the flux surface. Using this assumption the new edge CXRS measurements reveal the existence of an asymmetric flow structure at the H-mode edge. In the ETB the poloidal impurity flow exhibits a strongly sheared flow in the electron diamagnetic direction both at the LFS and HFS. The HFS poloidal rotation velocity is about a factor of 1.5–2 lower than at the LFS thus, breaking the dependence of the poloidal flow on the poloidal magnetic field. The toroidal rotation velocity is co-current at both the LFS and HFS, however, the profile exhibits an asymmetric structure.

Both the toroidal flow asymmetry and the difference in magnitude of the poloidal flow might arise due to the existence of a poloidal impurity density asymmetry, with the impurity density being larger at the HFS. The evaluation of E_r from the measured HFS and LFS profiles enables the determination of the electrostatic potential at both poloidal positions. The measurements show that within the uncertainties the electrostatic potential is a flux function and forms a consistent equilibrium with the measured flow structure.

- **Is neoclassical theory sufficient to describe the observed poloidal rotation velocities at the plasma edge?**

Experimental tests against neoclassical theory have been performed which show that at the plasma edge the poloidal rotation of both main ions and impurities is at neoclassical levels. Both the sign and the magnitude of the neoclassical predictions are in very good agreement with the measurement. Hence, the poloidal main ion flow is driven by the ion temperature gradient, while the poloidal impurity flow is determined by both the ion temperature and pressure gradient. The fact that at the plasma edge the E_r well is mainly determined by the main ion pressure gradient term $\nabla p_i / en_i$ is consistent with the main ion poloidal flow behaving as expected from neoclassical theory.

The time resolution of the edge CXRS diagnostics (2.2 ms) allows the study of the temporal evolution of E_r during an ELM cycle. At the ELM crash the E_r minimum decreases leading to a reduction of the $\mathbf{E} \times \mathbf{B}$ shear layer. Shortly after the ELM, the profile recovers and the E_r well reforms reaching its initial value 4–6 ms after the ELM. A comparison to the main ion pressure gradient term shows remarkably good agreement in both the magnitude and the

temporal evolution. This suggests that ∇p_i and the E_r well recover on similar time scales. In high density type-I ELM-mitigated H-mode plasmas, obtained via externally applied magnetic perturbations (MPs) with toroidal mode number $n = 2$, no obvious effect on the E_r profile is visible. In H-mode plasmas with MPs in the $n = 1$ configuration a slight reduction ($\sim 15\%$) of the E_r well is observed, however, the difference is within the uncertainties of the measurements. Although the reduction is within the error bars, it is observed for both resonant and non-resonant MPs compared to the reference discharge without MPs. This indicates that in high density, magnetically perturbed ($n = 1$) H-mode plasmas the MP may penetrate into the pedestal causing a small reduction of the E_r well. The radial electric field and the main ion pressure gradient term at the plasma edge are found to match even in the presence of MPs. This underlines that E_r and the gradients in the main ion species are closely coupled. The results presented in this thesis show that the particle and energy transport across the pedestal and the radial electric field build a closed, self-consistent system. This work provides experimental evidence that the E_r well is created by the gradients in the main ion species. The main points discussed in this thesis support that the ion channel plays a key role in the interplay between $\mathbf{E} \times \mathbf{B}$ velocity shearing, turbulence and transport reduction.

8.2 Directions for future work

As presented in this thesis the evaluation of the radial electric field E_r via CXRS enables an unprecedented high-accuracy localization of the E_r dip and is well suited to study the relationship between the ETB and E_r . The installation of additional optical heads, which provide more lines of sight and fill the gaps in-between the existing channels, would provide more detailed edge CXRS profiles without the need of performing a radial plasma sweep. Hence, very detailed profiles could be measured during the L-H transition. At the same time more accurate measurements of the gradients in ion temperature, impurity density, rotation velocities and E_r could be obtained for a single time point. Faster CXRS measurements, on a timescale of several hundreds of μs , coupled with detailed comparison to the edge kinetic profiles will allow a deeper understanding of the mechanism causing the L-H transition.

The question why the main ion flow velocity perpendicular to the magnetic field is almost zero remains an open issue. The measurements performed during this thesis demonstrate that the poloidal rotation of both main ions and impurities is neoclassical, however, the actual mechanism responsible for the small toroidal rotation velocities observed at the plasma edge remains unclear. The identification of the dominant processes that are relevant at the plasma edge is essential for understanding the edge toroidal rotation and toroidal momentum transport.

Developing an alternative discharge scenario to obtain low collisionality plasmas at AUG would enable the test of poloidal flow measurements against neoclassical theory in the low collisionality regime, i.e. in the banana regime. A scan in collisionality could help identifying at which critical value of the collisionality the orbit-squeezing effect may become important.

The novel CXRS measurements at the inboard midplane have revealed the existence of an asymmetric flow structure on a flux surface, which is thought to arise due to a poloidal impurity density asymmetry. A direct evaluation of the impurity density profile at the high-field side is pending. Measurements of the gas puff cloud combined with modelling of the neutral gas puff penetration is required to obtain a quantitative measurement of the poloidal impurity density asymmetry.

Acknowledgements

During the last three years I have profited immensely from the expertise, intellect and encouragement of several people. At this stage I want to thank everybody who has contributed to this thesis, both professionally and personally.

First and foremost, I would like to express my deep gratitude to my advisor, Dr. Thomas Pütterich, who encouraged me throughout the whole thesis. I was fortunate to be his first PhD student and I have benefited a huge amount from his enthusiasm for science and research. Thank you for your dedication, your patience, your constant support and your friendship. *Ich danke Dir für alles, einen besseren Betreuer hätte ich mir nicht wünschen können!*

I am grateful to my academic advisor, Prof. Dr. Harmut Zohm, for guiding me through this process. Thank you for giving me the opportunity to perform this thesis under your supervision and thank you for the fruitful discussions, especially towards the end of the thesis.

I would like to extend my appreciation to my group leader, Dr. Ralph Dux, who was a constant source of support and motivation. Thank you for answering all my questions and for the many hours we spend in front of the spectrometer. Thank you for your time and dedication.

I want to thank Dr. Rachael McDermott for being my ‘not-a-supervisor’, I have profited immensely from our discussions and your knowledge. I will never forget our calibration nights.

I am deeply indebted to Dr. Emiliano Fable who has taught me so much about neoclassical theory (and theory in general) and who always supported me and showed interest in my work. *Grazie mille per tutte le discussioni e per il tuo sostegno.*

I am grateful to Prof. Dr. Arne Kallenbach for his supporting optimism, for his enthusiasm and the fruitful discussions over the last years. Furthermore, I want to express my appreciation to Prof. Dr. Uli Stroth, thank you for your insight, interest and input to this work.

My deepest appreciation to Prof. Dr. Karl Lackner for the fruitful discussions and vivid pictures. Thank you for your generosity in time in the very last minutes.

I would like to thank Dr. Garrard Conway and Dr. Tim Happel for their enthusiasm and for their tireless efforts to explain the nuances of turbulence and Doppler reflectometry. Thank you for your patience in answering all my questions and thank you for the many lessons you gave me in the last three years. I would also like to extend my appreciation to Dr. Clemente Angioni, Dr. Andreas Bergmann, Dr. Francis Casson, Dr. François Ryter, Dr. Wolfgang Suttrop, Dr. Elisabeth Wolfrum and Dr. Qingquan Yu for their contributions and input to this work. Thank you for your availability and time.

Special thanks deserves the whole spectroscopy group, especially Benedikt Geiger, Dr. Steffen Potzel, Athina Kappatou, Matthias Bernert, Felix Reimold, Dr. Marco Sertoli, Arthur Janzer and our technicians Anton Mayer and Andreas Bolland. Thank you for your help and all the fun and laughs in the lab, in the vessel and in the control room.

The installation of the new diagnostics would not have been possible without the constant support and help of Wolfgang Zeidner. *Danke für die unzähligen Stunden im und am Gefäß,*

im Labor, am Spektrometer, mit den Optikköpfen und Lichtleitern. Ohne Deine Unterstützung wäre diese Arbeit nicht möglich gewesen. Special thanks to Dr. Albrecht Hermann for his constant support and to Michael Ebner for all his help and for always lending me a hand or a tool. I am grateful to Peter Bischoff for his patience in refurbishing all the optical fibers needed for this work. I would like to extend my gratitude to Karl Eismann, who coordinated the construction of every single piece of the spectrometer and the optical heads, and to Günther Eicher for his endurance when sharpening the entrance slit of the spectrometer. *Ein herzliches Dankeschön an die gesamten Gefäßmannschaft und die EI-Werkstatt für die Unterstützung beim Aufbau der neuen Diagnostiken.* I am thankful to Dr. Karl Behler and Dr. Roland Merkel for their support in setting up the diagnostic computers. Special thanks to Helmut Blank for helping me set up the shotfile headers and to Georg Zimmermann for providing the power switches, an essential piece for the shot-to-shot wavelength calibration.

I would like to acknowledge the whole ASDEX Upgrade Team for their support, friendship and all the help. Special thanks to all the experiment leaders for their assistance in designing the discharges. I am grateful to Dr. Christian Hopf and the whole NBI group, without you this work would not have been possible. Special thanks deserve Anja Bauer, Gabriele Dörsch, Petra Jordan and Margot Jung for their support in administrative and bureaucratic questions.

I would like to express my gratitude to Sina Fietz, Matthias Bernert, Andreas Burckhart, Benedikt Geiger, Sylvia Rathgeber, Fabian Sommer, João Bernardo, Marco Veranda, Alessandro Scaggion and Emanuele Sartori for the great time we had in Munich, Lisboa and Padova. *Vielen Dank, obrigada e grazie mille per le avventure!*

Many thanks to all my fellow PhD students and postdocs at IPP who have worked alongside me and helped me in so many ways: Dr. Leena Aho-Mantila, Dr. Laura Barrera-Orte, Dr. Gregor Birkenmeier, Dr. Jurrian Boom, Livia Casali, Dr. Ivo Classen, Diarmuid Curran, Dr. Hauke Doerk, Mike Dunne, Dr. Tilmann Lunt, Pierre Sauter, Dr. Philip Schneider, Christian Vorpahl, Dr. Bernd Wieland, Matthias Willensdorfer ... Thank you for the good time we had during lunch, at the various conferences and thank you for all the discussions and laughs.

Special thanks deserves Sina Fietz, who was a constant source of support in the last years. Thank you for always being there and backing me up when I needed you.

I am thankful to Samy, Jose H., Jorge, Manuel, Elisa, Jose M., Franziska, Marta, Eric, Naty and Rafa for cheering me up, for showing me that there is life outside work (though in the last months there wasn't) and for the great time we always spend together. *Muchas gracias!*

I want to thank my family in Italy, my grandmother, aunts and uncles and all my cousins. Special thanks deserves Rosy Viezzer who has supported me so much in the last years. *Ti ringrazio di cuore per tutto quello che hai fatto per noi.* I want to extend my appreciation to my family on the Philippines, so far away, but you are always in my thoughts.

I do not have words to express my gratitude to my closest friend Katharina who was always there when I most needed her. Thank you for all your emails and our Skype-sessions, for your support and belief in me and what I can achieve. *Merci beaucoup pour tout et je viendrai te rendre visite bientôt, promis!*

I am incredibly fortunate to have met Manuel, the one who went through all the ups and downs I encountered during this thesis. Thank you for your endurance and your encouragement. Hearing your voice at the end of the day made my day!

I am even more fortunate to have such a loving and supportive family. I want to thank my mother Victorina and my brother Denis who were always there when I most needed them. Thank you for your understanding, your unconditional love and for keeping my spirits up. I dedicate this thesis to you, *salamat para sa lahat!*

Bibliography

- [1] J. Wesson. *Tokamaks*. 3rd edition, ISBN 0 19 8509227, Oxford University Press, Oxford, 2004.
- [2] J. Jacquinot and the JET team. *Plasma Phys. Control. Fusion*, 41:A13, 1999.
- [3] F. Wagner *et al.*. *Phys. Rev. Lett.*, 49(19):1408, 1982.
- [4] H. Biglari *et al.* *Phys. Fluids B*, 2:1, 1990.
- [5] R.J. Fonck *et al.* *Phys. Rev. A*, 29(6), 1984.
- [6] K. Ida. *Plasma Phys. Control. Fusion*, 40:1429, 1998.
- [7] S.-I. Itoh and K. Itoh. *Phys. Rev. Lett.*, 60:2276, 1988.
- [8] K. C. Shaing. *Phys. Fluids*, 31(8):2249, 1988.
- [9] J. Kim *et al.* *Phys. Rev. Lett.*, 72(14):2199, 1994.
- [10] K. H. Burrell *et al.* *Phys. Plasmas*, 1(5):1536, 1994.
- [11] R. J. Groebner *et al.* *Phys. Rev. Lett.*, 64(25):3015, 1990.
- [12] K. H. Burrell *et al.* *Phys. Plasmas*, 4:1499, 1997.
- [13] K. H. Burrell *et al.* *Plasma Phys. Control. Fusion*, 46:A165, 2004.
- [14] P. Gohil *et al.* *Nucl. Fusion*, 38(1):93, 1998.
- [15] N. Hawkes *et al.* *Plasma Phys. Control. Fusion*, 38:1261, 1996.
- [16] Y. Andrew *et al.* *Eur. Phys. Lett.*, 83:15003, 2008.
- [17] R. M. McDermott *et al.* *Phys. Plasmas*, 16:056103, 2009.
- [18] K. Kamiya *et al.* *Nucl. Fusion*, 51:053009, 2011.
- [19] M. Hirsch *et al.* *Plasma Phys. Control. Fusion*, 43:1641, 2001.
- [20] T. Ido *et al.* *Rev. Sci. Instrum.*, 70:955, 1999.
- [21] L. I. Krupnik *et al.* *Fus. Eng. Design*, 56-57:935, 2001.
- [22] H. Meister *et al.* *Nucl. Fusion*, 41(11):1633, 2001.

- [23] G. D. Conway *et al.* *Plasma Phys. Control. Fusion*, 46:951, 2004.
- [24] J. Schirmer *et al.* *Nucl. Fusion*, 46:S780–S791, 2006.
- [25] B. Wieland. *Investigations on radial electric fields in the edge transport barrier of H-mode discharges*. PhD thesis, Technische Universität München, 2011.
- [26] R. Fischer *et al.* *Fus. Sci. Technol.*, 58:675, 2010.
- [27] F. L. Hinton and R. D. Hazeltine. *Rev. Mod. Physics*, 48(2):239, 1976.
- [28] R. Dux. *Plasmaphysik und Fusionsforschung. Lecture script, Universität Augsburg*, 2002.
- [29] P. Helander and D. J. Sigmar. *Collisional Transport in Magnetized Plasmas*. 1st edition, ISBN 0-521-80798 -0, Cambridge University Press, Cambridge, 2002.
- [30] S. P. Hirshman and D. J. Sigmar. *Nucl. Fusion*, 21(9):1079, 1981.
- [31] R. B. White. *Theory of Tokamak Plasmas*. North Holland Physics, Elsevier Science Publisher B.V., Amsterdam, 1989.
- [32] E. J. Doyle *et al.* *Nucl. Fusion*, 47:S18, 2007.
- [33] T. Pütterich *et al.* *J. Nucl. Mater.*, 415(1):S334–S339, 2011.
- [34] H. Zohm. *Plasmaphysik. Lecture script, Ludwig-Maximilians-Universität München*, 2001.
- [35] Y. B. Kim *et al.* *Phys. Fluids B*, 3(8), 1991.
- [36] J. D. Callen *et al.* *Nucl. Fusion*, 49:085021, 2009.
- [37] U. Stroth *et al.* *Plasma Phys. Control. Fusion*, 53:024006, 2011.
- [38] A. G. Peeters. *Phys. Plasmas*, 7(1):268, 2000.
- [39] K. C. Shaing. *Phys. Plasmas*, 10(5):1443, 2003.
- [40] K. C. Shaing *et al.* *Nucl. Fusion*, 50:025022, 2010.
- [41] P. H. Diamond and Y.-B. Kim. *Phys. Fluids B*, 3:1626, 1991.
- [42] A. G. Peeters *et al.* *Nucl. Fusion*, 51:094027, 2011.
- [43] K. C. Shaing *et al.* *Phys. Fluids B*, 2(6):1492, 1990.
- [44] F. L. Hinton *et al.* *Phys. Lett. A*, 259:267, 1999.
- [45] E. A. Belli and J. Candy. *Plasma Phys. Control. Fusion*, 50:095010, 2008.
- [46] S. D. Pinches *et al.* *Comp. Phys. Comm.*, 111:133, 1998.
- [47] P. A. Schneider. *Characterization and scaling of the tokamak edge transport barrier*. PhD thesis, Ludwig-Maximilians-Universität München, 2012.

- [48] W. Suttrop *et al.* *Plasma Phys. Control. Fusion*, 39:2051, 1997.
- [49] F. Ryter *et al.* *Plasma Phys. Control. Fusion*, 43(A323), 2001.
- [50] A. M. Dimits *et al.* *Phys. Plasmas*, 7:969, 2000.
- [51] Y. R. Martin *et al.* *J. Phys.: Conf. Ser.*, 123:012033, 2008.
- [52] F. Ryter *et al.* *Nucl. Fusion*, 36:1217, 1996.
- [53] T. N. Carlstrom and R. J. Groebner. *Phys. Plasmas*, 3:1867, 1996.
- [54] A. E. Hubbard *et al.* *Plasma Phys. Control. Fusion*, 40:689, 1998.
- [55] F. Ryter *et al.* *Nucl. Fusion*, 49(062003), 2009.
- [56] P. Sauter *et al.* *Nucl. Fusion*, 52:012001, 2012.
- [57] H. Zohm. *Plasma Phys. Control. Fusion*, 38(2):105, 1996.
- [58] J. W. Connor *et al.* *Phys. Plasmas*, 5(7):2687, 1998.
- [59] P. B. Snyder *et al.* *Phys. Plasmas*, 9:2037, 2002.
- [60] A. Burckhart *et al.* *Plasma Phys. Control. Fusion*, 52:105010, 2010.
- [61] M. Shimada *et al.* *Nucl. Fusion*, 47:S1, 2007.
- [62] P. W. Terry *et al.* *Rev. Mod. Phys.*, 72(1):109, 2000.
- [63] P. Manz *et al.* *Phys. Rev. Lett.*, 103:165004, 2009.
- [64] P. H. Diamond *et al.* *Plasma Phys. Control. Fusion*, 47:R35, 2005.
- [65] K. Itoh *et al.* *Phys. Plasmas*, 13:055502, 2006.
- [66] A. Fujisawa. *Nucl. Fusion*, 49:013001, 2009.
- [67] G. D. Conway *et al.* *Conf. Proceedings of the 23rd IAEA Fusion Energy Conference, IAEA-CN-180/EXC/7-1, Daejeon*, 2010.
- [68] G. D. Conway *et al.* *Phys. Rev. Lett.*, 106:065001, 2011.
- [69] K. C. Shaing and E. C. Crume, Jr. *Phys. Rev. Lett.*, 63(21):2369, 1989.
- [70] A. B. Hassam *et al.* *Phys. Rev. Lett.*, 66:309, 1991.
- [71] T. E. Stringer *et al.* *Phys. Rev. Lett.*, 22:1770, 1969.
- [72] R.C. Isler. *Physica Scripta*, 35:650, 1987.
- [73] M. G. von Hellermann *et al.* *Physica Scripta*, T120:19, 2005.
- [74] B. Geiger. *Fast-ion transport studies using FIDA spectroscopy at the ASDEX Upgrade tokamak*. PhD thesis, Ludwig-Maximilians-Universität München, 2012.

- [75] R. Dux *et al.* Conf. Proceedings of the 39th EPS Conference on Plasma Physics, ECA Vol. 36F, P2.049, Stockholm, 2012.
- [76] F. F. Chen. *Introduction to Plasma Physics and Controlled Fusion*. 2nd edition, ISBN 0-306-41332-9, Plenum Press, New York, 1983.
- [77] R. B. White and F. F. Chen. *Plasma Phys.*, 16:565, 1974.
- [78] T. Happel. *Doppler Reflectometry in the TJ-II Stellarator: Design of an Optimized Doppler Reflectometer and its Application to Turbulence and Radial Electric Field Studies*. PhD thesis, Universidad Carlos III de Madrid, 2010.
- [79] G. D. Conway *et al.* *Plasma Fus. Research*, 5(S2005), 2010.
- [80] I. Hutchinson. *Principles of plasma diagnostics*. 2nd edition, ISBN 978-0521803892, Cambridge University Press, Cambridge, 2002.
- [81] M. Hirsch *et al.* *Plasma Phys. Control. Fusion*, 48:S155, 2006.
- [82] T. Estrada *et al.* *Plasma Phys. Control. Fusion*, 51:124015, 2009.
- [83] G. R. McKee *et al.* *Phys. Plasmas*, 7:1870, 2000.
- [84] S. Klenge. *Dynamik magnetisch eingeschlossener Plasmen am L-H Übergang*. PhD thesis, Universität Stuttgart, 2005.
- [85] J. Schirmer. *Plasma Turbulence Studies Using Correlation Doppler Reflectometry on the ASDEX Upgrade Tokamak*. PhD thesis, Ludwig-Maximilians-Universität München, 2005.
- [86] C. Tröster. *Development of a flexible Doppler reflectometry system and its application to turbulence characterization in the ASDEX Upgrade tokamak*. PhD thesis, Ludwig-Maximilians-Universität München, 2008.
- [87] T. Happel *et al.* 10th International Reflectometry Workshop. Padova, Italy, 2011.
- [88] S. K. Rathgeber *et al.* *Plasma Phys. Control. Fusion (accepted for publication)*, 2012.
- [89] W. Suttrop. *Practical Limitations to Plasma Edge Electron Temperature Measurements by Radiometry of Electron Cyclotron Emission*. IPP Report 1/306, Max-Planck-Institute for Plasma Physics, Garching, Germany, 1997.
- [90] B. Kurzan *et al.* *Rev. Sci. Instrum.*, 82:103501, 2011.
- [91] J. Schweinzer *et al.* *Plasma Phys. Control. Fusion*, 34(7):1173, 1992.
- [92] R. Fischer *et al.* *Plasma Phys. Control. Fusion*, 50:085009, 2008.
- [93] M. Willensdorfer *et al.* *Rev. Sci. Instrum.*, 83:023501, 2012.
- [94] O. Gehre. *International Journal of Infrared and Millimeter Waves*, 5(3), 1984.
- [95] A. Mlynek *et al.* *Rev. Sci. Instrum.*, 81:033507, 2010.

- [96] ITER Physics Expert Group on Confinement and Transport *et al.* *Nucl. Fusion*, 39:2175, 1999.
- [97] E. Wolfrum *et al.* Conf. Proceedings of the 22nd IAEA Fusion Energy Conference, EX/P3-7, Geneva, 2008.
- [98] J. Neuhauser *et al.* *Plasma Phys. Control. Fusion*, 44:855, 2002.
- [99] A. Kallenbach *et al.* *J. Nucl. Mater.*, 337-339:381, 2005.
- [100] T. Pütterich *et al.* *Phys. Rev. Lett.*, 102(025001), 2009.
- [101] W. Suttrop *et al.* *Phys. Rev. Lett.*, 106(225004), 2011.
- [102] R. Fischer *et al.* *Plasma Phys. Control. Fusion*, 54:115008, 2012.
- [103] E. Viezzer *et al.* *Rev. Sci. Instrum.*, 83:103501, 2012.
- [104] T. Pütterich *et al.* Conf. Proceedings of the 35th EPS Conference on Plasma Physics, ECA Vol. 32D, P-2.083. Crete, 2008.
- [105] Princeton Instruments. <http://www.princetoninstruments.com>.
- [106] NIST Atomic Spectra Database. http://physics.nist.gov/PhysRefData/ASD/lines_form.html.
- [107] E. Viezzer *et al.* *Plasma Phys. Control. Fusion*, 53:035002, 2011.
- [108] T. Pütterich *et al.* *Nucl. Fusion*, 52:083013, 2012.
- [109] M. von Hellermann *et al.* *Plasma Phys. Control. Fusion*, 37:71, 1995.
- [110] FARO Technologies, Inc. <http://www.faro.com>.
- [111] R. E. Bell. *Rev. Sci. Instrum.*, 75(10), 2004.
- [112] R. E. Bell and E. J. Synakowski. *AIP Conf. Proc.*, 547:39, 2000.
- [113] R. E. Bell *et al.*. *Phys. Plasmas*, 17:082507, 2010.
- [114] W. M. Solomon *et al.* *Rev. Sci. Instrum.*, 75(10):3481, 2004.
- [115] K. Crombé. *Spectroscopic studies of Impurity Ion Dynamics on the JET and TEXTOR Tokamaks*, ISBN 90-8578-033-0, available at <http://hdl.handle.net/1854/5551>. PhD thesis, Ghent University, 2006.
- [116] R. D. Cowan. *The Theory of Atomic Structure and Spectra*. University of California Press, ISBN 9780520038219, 1981.
- [117] H. P. Summers. *ADAS User Manual 2.6*. <http://www.adas.ac.uk/manual.php>, 2004.
- [118] W. L. Wiese *et al.* *Atomic Transition Probabilities, Volume I Hydrogen Through Neon, A Critical Data Compilation, NSRDS-NBS 4*. National Standard Reference Data Series, National Bureau of Standards 4, U. S. Government Printing Office, Washington, D. C., 1966.

- [119] A. Blom and C. Jupén. *Plasma Phys. Control. Fusion*, 44:1229, 2002.
- [120] J. D. Hey *et al.* Conf. Proceedings of the 20th EPS Conference on Contr. Fusion and Plasma Physics, ECA VOL. 17C/III, p. 1111, Lisbon, 1993.
- [121] D. H. Sampson. *J. Phys. B: At. Mol. Phys.*, 10(4):749, 1977.
- [122] K. H. Burrell *et al.* *Plasma Phys. Control. Fusion*, 31:10, 1989.
- [123] R. E. Bell *et al.* *Phys. Rev. Lett.*, 81(7):1429, 1998.
- [124] J. W. Coenen *et al.* *J. Phys. B: At. Mol. Opt. Phys.*, 43:144015, 2010.
- [125] H. Meyer *et al.* *Jour. of Phys.: Conference Series*, 123:012005, 2008.
- [126] K. Ida *et al.* *Rev. Sci. Instrum.*, 71(6):2360, 2000.
- [127] R. Brakel *et al.* *Plasma Phys. Control. Fusion*, 39:B273–B286, 1997.
- [128] T. Happel *et al.* *Phys. Plasmas*, 18:102302, 2011.
- [129] V. Antoni *et al.* *Phys. Rev. Lett.*, 79:24, 1997.
- [130] W. Schneider *et al.* *Fusion Engineering and Design*, 48:127, 2000.
- [131] F. Ryter *et al.* Conf. Proceedings of the 24th IAEA Fusion Energy Conference, EX/P4-03, San Diego, 2012.
- [132] T. Fülöp and P. Helander. *Phys. Plasmas*, 8:3305, 2001.
- [133] K. D. Marr *et al.* *Plasma Phys. Control. Fusion*, 52(055010), 2010.
- [134] R. M. Churchill *et al.* 53rd APS conference, UP9.009, Salt Lake City, 2011.
- [135] E. Fable and A. Bergmann. *Private Communications*, 2012.
- [136] E. Fable *et al.* *Nucl. Fusion (to be submitted)*, 2012.
- [137] K. Itoh and S.-I. Itoh. *Plasma Phys. Control. Fusion*, 38:1, 1996.
- [138] D. G. Whyte *et al.* *Nucl. Fusion*, 50(105005), 2010.
- [139] F. Ryter *et al.* *Plasma Phys. Control. Fusion*, 40:725, 1998.
- [140] O. Gruber *et al.* *Nucl. Fusion*, 49(115014), 2009.
- [141] P. Lang *et al.* Conf. Proc. of the 24th IAEA Fusion Energy Conf., EX/P4-01, San Diego, 2012.
- [142] K. Ida *et al.* *Phys. Rev. Lett.*, 65(11):1364, 1990.
- [143] ITER. <http://www.iter.org>.
- [144] P. A. Schneider *et al.* *Plasma Phys. Control. Fusion*, 54:105009, 2012.

- [145] T. S. Hahm and K. H. Burrell. *Phys. Plasmas*, 2(5):1648, 1995.
- [146] G. D. Conway *et al.* *Plasma Phys. Control. Fusion*, 44:451, 2002.
- [147] R. A. Moyer *et al.* *Phys. Plasmas*, 2(6):2397, 1995.
- [148] K. H. Burrell *et al.* *Phys. Plasmas*, 6(12):4418, 1999.
- [149] M. R. Wade *et al.* *Phys. Plasmas*, 12:056120, 2005.
- [150] H. Meyer *et al.* *Nucl. Fusion*, 51(113011), 2011.
- [151] W. Suttrop *et al.* *Fusion Eng. Design*, 84(290), 2009.
- [152] M. Greenwald *et al.* *Nucl. Fusion*, 28:2199, 1988.
- [153] W. Suttrop *et al.* *Plasma Phys. Control. Fusion*, 53:124014, 2011.
- [154] J. C. Fuchs *et al.* *Conf. Proceedings of the 38th EPS Conference on Plasma Physics, P-1.090*. Strasbourg, 2011.
- [155] E. Strumberger and E. Schwarz. *Vacfield Code: Computation of the Vacuum Magnetic Field and Its First Derivatives for Various Coil Types*. IPP Report 5/112, Max-Planck-Institute for Plasma Physics, Garching, Germany, 2005.
- [156] R. A. Moyer *et al.* *Phys. Plasmas*, 12:056119, 2005.
- [157] J. W. Coenen *et al.* *Nucl. Fusion*, 51(063030), 2011.
- [158] W. Suttrop *et al.* *Conf. Proc. of the 24th IAEA Fusion Energy Conf., EX/3-4, San Diego*, 2012.
- [159] S. K. Rathgeber. *Electron temperature and pressure profiles at the edge of ASDEX Upgrade – Estimation via electron cyclotron radiation forward modelling and investigation of the gradients in the presence of magnetic perturbations (to be submitted)*. PhD thesis, Ludwig-Maximilians-Universität München, 2013.
- [160] M. Kočan *et al.* *Conf. Proc. of the 24th IAEA Fusion Energy Conf., EX/P7-23, San Diego*, 2012.
- [161] K. Crombé *et al.* *Phys. Rev. Lett.*, 95(155003), 2005.
- [162] T. Tala *et al.* *Nucl. Fusion*, 47:1012, 2007.
- [163] W. M. Solomon *et al.* *Phys. Plasmas*, 13(056116), 2006.
- [164] R. E. Bell. *Rev. Sci. Instrum.*, 68(2):1273, 1997.
- [165] F. L. Hinton *et al.* *Phys. Rev. Lett.*, 72(8):1216, 1994.
- [166] R. D. Hazeltine. *Phys. Fluids B*, 1(10):2031, 1989.
- [167] B. J. Ding *et al.* *Plasma Phys. Control. Fusion*, 47(789), 2005.

-
- [168] B. J. Ding *et al.* *Chin. Phys.*, 16(3434), 2007.
- [169] G. Kagan *et al.* *Plasma Phys. Control. Fusion*, 53(025008), 2011.
- [170] A. R. Field *et al.* *Plasma Phys. Control. Fusion*, 51(105002), 2009.
- [171] R. Dux and A. G. Peeters. *Nucl. Fusion*, 40(10):1721, 2000.
- [172] R. Dux. *Impurity Transport in Tokamak Plasmas*. IPP Report 10/27, Professorial dissertation, University Augsburg, 2004.
- [173] E. A. Belli and J. Candy. *Plasma Phys. Control. Fusion*, 51:075018, 2009.
- [174] A. Bergmann *et al.* *Phys. Plasmas*, 8:5192, 2001.
- [175] A. Bergmann. *Private Communications*, 2012.

List of Publications

1. **E. Viezzer**, T. Pütterich, E. Fable, C. Angioni, A. Bergmann, R. Dux, R. M. McDermott and the ASDEX Upgrade Team
Experimental evidence of neoclassical poloidal rotation velocities at the plasma edge of ASDEX Upgrade (in preparation)
2. **E. Viezzer**, T. Pütterich, G. D. Conway, R. Dux, T. Happel, J.C. Fuchs, R. M. McDermott, F. Ryter, B. Sieglin, W. Suttrop, M. Willensdorfer, E. Wolfrum and the ASDEX Upgrade Team
High-accuracy characterization of the edge radial electric field at ASDEX Upgrade
Nucl. Fusion (submitted October 2012)
3. **E. Viezzer**, T. Pütterich, R. Dux, R. M. McDermott and the ASDEX Upgrade Team
High-resolution charge-exchange measurements at ASDEX Upgrade
Rev. Sci. Instrum. **83** 103501 (2012)
4. **E. Viezzer**, T. Pütterich, R. Dux, A. Kallenbach and the ASDEX Upgrade Team
Investigation of passive edge emission in charge exchange spectra at the ASDEX Upgrade tokamak
Plasma Phys. Control. Fusion **53** 035002 (2011)
5. E. Wolfrum, P. Sauter, M. Willensdorfer, F. Ryter, F. Aumayr, L. Barrera-Orte, A. Burckhart, E. Fable, R. Fischer, B. Kurzan, T. Pütterich, S. Rathgeber, W. Suttrop, **E. Viezzer** and the ASDEX Upgrade Team
Recent progress in understanding the L-H transition physics from ASDEX Upgrade
Plasma Phys. Control. Fusion **54** 124002 (2012)
6. T. Makkonen, M. Groth, M. Airila, A. Janzer, R. Dux, T. Kurki-Suonio, T. Lunt, H. W. Müller, T. Pütterich, **E. Viezzer** and the ASDEX Upgrade Team
Measurements and ERO simulations of carbon flows in the high-field size main SOL in ASDEX Upgrade
Accepted for publication in Journ. Nucl. Materials (2012)
7. F. Ryter, S. K. Rathgeber, **E. Viezzer**, W. Suttrop, A. Burckhart, R. Fischer, B. Kurzan, S. Potzel, T. Pütterich and the ASDEX Upgrade Team
L-H transition in the presence of magnetic perturbations in ASDEX Upgrade
Nucl. Fusion **52** 114014 (2012)
8. F. Sommer, J. Stober, C. Angioni, M. Bernert, A. Burckhart, V. Bobkov, R. Fischer, C. Fuchs, R. M. McDermott, W. Suttrop, **E. Viezzer** and the ASDEX Upgrade Team
H-mode characterization for dominant ECRH and comparison to dominant NBI and

- ICRF heating at ASDEX Upgrade*
Nucl. Fusion **52** 114018 (2012)
9. R. P. Wenninger, H. Zohm, J. E. Boom, A. Burckhart, M. G. Dunne, R. Dux, T. Eich, R. Fischer, J. C. Fuchs, M. Garcia-Munoz, V. Igochine, M. Hölzl, N. C. Luhmann Jr., T. Lunt, M. Maraschek, H. W. Müller, H. K. Park, P. A. Schneider, F. Sommer, W. Suttrop, **E. Viezzer** and the ASDEX Upgrade Team
Solitary magnetic perturbations at the ELM onset
Nucl. Fusion **52** 114025 (2012)
10. M. Willensdorfer, E. Wolfrum, A. Scarabosio, F. Aumayr, R. Fischer, B. Kurzan, R. M. McDermott, A. Mlynek, B. Nold, S.K. Rathgeber, V. Rohde, F. Ryter, P. Sauter, **E. Viezzer** and the ASDEX Upgrade Team
Electron density evolution after L-H transitions and the L-H/H-L cycle in ASDEX Upgrade
Nucl. Fusion **52** 114026 (2012)
11. T. Pütterich, **E. Viezzer**, R. Dux, R. M. McDermott and the ASDEX Upgrade Team
Poloidal asymmetry of parallel rotation measured in ASDEX Upgrade Nucl. Fusion **52** 083013 (2012)
12. E. Fable, C. Angioni, R. Fischer, B. Geiger, R.M. McDermott, G.V. Pereverzev, T. Pütterich, F. Ryter, B. Scott, G. Tardini, **E. Viezzer** and the ASDEX Upgrade Team
Progress in characterization and modelling of the current ramp-up phase of ASDEX Upgrade discharges
Nucl. Fusion **52** 063017 (2012)
13. P. Sauter, T. Pütterich, F. Ryter, **E. Viezzer**, E. Wolfrum, G. D. Conway, R. Fischer, B. Kurzan, R. M. McDermott, S. K. Rathgeber and the ASDEX Upgrade Team
L- to H-mode transitions at low density in ASDEX Upgrade
Nucl. Fusion **52** 012001 (2012)
14. R. M. McDermott, C. Angioni, R. Dux, E. Fable, T. Pütterich, F. Ryter, A. Salmi, T. Tala, G. Tardini, **E. Viezzer** and the ASDEX Upgrade Team
Core momentum and particle transport studies in the ASDEX Upgrade tokamak
Plasma Phys. Control. Fusion **53** 124013 (2011)
15. W. Suttrop, L. Barrera, A. Herrmann, R. M. McDermott, T. Eich, R. Fischer, B. Kurzan, P. T. Lang, A. Mlynek, T. Pütterich, S. K. Rathgeber, M. Rott, T. Vierle, **E. Viezzer**, M. Willensdorfer, E. Wolfrum, I. Zammuto and the ASDEX Upgrade Team
Studies of edge localized mode mitigation with new active in-vessel saddle coils in ASDEX Upgrade
Plasma Phys. Control. Fusion **53** 124014 (2011)
16. C. Angioni, R. M. McDermott, F. J. Casson, E. Fable, A. Bottino, R. Dux, R. Fischer, Y. Podoba, T. Pütterich, F. Ryter, **E. Viezzer**, ASDEX Upgrade Team
Intrinsic Toroidal Rotation, Density Peaking, and Turbulence Regimes in the Core of Tokamak Plasmas
Phys. Rev. Lett. **107** 215003 (2011)

17. A. Kallenbach *et al.*
Overview of ASDEX Upgrade results Nucl. Fusion **51** 094012 (2011)
18. T. Lunt, Y. Feng, M. Bernert, A. Herrmann, P. de Marné, R. McDermott, H. W.Müller, S. Potzel, T. Pütterich, S. Rathgeber, W. Suttrop, **E. Viezzer**, E. Wolfrum, M. Willensdorfer and the ASDEX Upgrade team
First EMC3-Eirene simulations of the edge magnetic perturbations at ASDEX Upgrade compared to the experiment Nuclear Fusion **52** 054013 (2011)